DEMONSTRATION OF CODE-DIVISION MULTIPLE-ACCESS ENCODING AND DECODING OF FEMTOSECOND OPTICAL PULSES OVER A 2.5-KM DISPERSION-COMPENSATED FIBER LINK

A Thesis

Submitted to the Faculty

of

Purdue University

by

Cheng-Chun Chang

In Partial Fulfillment of the

Requirements for the Degree

of

Doctor of Philosophy

December 1997

TABLE OF CONTENTS

Page

LIST OF FIGURES

Figure Page

ABSTRACT

Chang, Cheng-Chun Ph.D., Purdue University, December 1997. Demonstration of Code-Division Multiple-Access Encoding and Decoding of Femtosecond Optical Pulses over a 2.5-km Dispersion-Compensated Fiber Link. Major Professor: Andrew. M. Weiner.

Ultrashort pulse code-division multiple-access (CDMA) based on spectral phase encoding and subsequent decoding of coherent femtosecond pulses offers an interesting approach for local area network applications. In this thesis, we report for the first time proof-of-concept transmission experiments for femtosecond pulse Code Division Multiple Access (CDMA) operating over kilometer lengths of optical fiber in the 1550 nm communication band. Our CDMA system integrates several novel components and sub-systems, including a femosecond modelocked Er-fiber laser and two chirped pulse fiber amplifiers, a pair of low-loss fiber-pigtailed pulse-shapers with programmable phase modulators for encoding/decoding and dispersion fine tuning , a 2.5-km dispersion-compensated transmission fiber, and an ultrafast nonlinear optical receiver. Femtosecond pulses generated by the Er-fiber laser are spectrally encoded by the first encoder pulse shaper. Coded pulses (which look like pseudorandom noise-bursts) are then transmitted over a 2.5-km transmission fiber link which is dispersion compensated using a special dispersion-compensating fiber (DCF). The output encoded pulses from the fiber link are sent to the second pulse shaper to decode the transmitted signals. With proper decoding phase codes, the encoded signals can be restored to almost its original pulsewidth. With wrong phase codes, the encoded signals remain as low-intensity noisebursts. A nonlinear fiber-optic thresholder is then used to distinguish properly decoded pulses from improperly decoded signals. This thesis

concentrates on the developement and study of a few individual component technologies, namely femtosecond pulse laser, dispersion compensation, and a femtosecond pulse encoder/phase compensator, and their integration into a single-user CDMA testbed. Almost distortionless transmission of sub-500-fs pulses over a few kilometers of fibers will be presented using a combination of DCF and a programmable pulse shaper. Because of the great successes of fiber dispersion compensation and spectral phase encoding/decoding, high-fidelity transmission of encoded femtosecond pulses over 2.5-km transmission fiber link is achieved, which leads to high contrast results in the nonlinear thresholder.

1. INTRODUCTION

As ever-increasing amount of information are created by human activities, communication systems of higher and higher capacity and speed are always in constant need. Fiber-optic lightwave systems widely employed in the 1980s have revolutionized the field of communication and replaced in many areas the coaxial cable and microwave communication systems. Optical fiber communication systems can offer, in principle, a tremendous amount signal bandwidth (>1 THz) because of the very large transmission bandwidth of optical fibers (~4 THz for system employing erbium-doped fiber amplifiers) and the large carrier frequency associated with optical carriers. However, in practice the bit rate is limited to several tens of GHz or less due to electronics-speed limitations for conventional point-to-point single-channel (or single-wavelength) systems, which only utilize a small slice of the huge signal bandwidth. To increase the bit rate and more efficiently use the bandwidth, multiple optical channels over the same fiber have to be employed. Most efforts have been devoted to time-division multiplexing (TDM) and wavelength-division multiplexing (WDM) systems. In TDM systems, data from multiple users are combined together through a series of narrow time slots. Higher bit rates are achieved by using shorter optical pulses and still limited by electronics. A high-speed TDM with data rate of 400 Gbit/s has been demonstrated using 0.98 ps optical pulses [1]. In WDM scheme, the optical bandwidth is carved into different wavelength channels. Signals of different carrier frequencies corresponding to different users propagate over the same fiber at moderate rates of ~20 Gbit/s. A WDM system with 55 such channels to give an aggregate rate of 1.1 Tbit/s has been demonstrated [2].

Optical code-division multiple-access (CDMA) systems offer another approach to take advantage of the large bandwidth of optical fibers and find important applications especially in the local- and metropolitan-area networks [3]. In a CDMA network, each transmitted signal is encoded with address information and broadcast to all receivers. The intended receiver applies a matched filter to incoming signals to distinguish the desired signal from high levels of background noise (unwanted signals). Multiple access is achieved by assigning different, minimally interfering code sequences to different subscriber pairs. Several different encoding schemes have been proposed to demonstrate CDMA operation. The earliest optical CDMA experiments use fiber-optic delay lines to "encode" a single input pulse into a series of delayed pulses [4, 5, 6]. The encoding of such scheme is performed in the time domain. In the decoding matched filter operation reconstructs the input pulse while unmatched decoding further subdivide the encoded pulse train. Such decoding techniques are based on intensity optical processing and can not sum to zero. Later CDMA works based on frequency-domain encoding of either coherent ultrashort pulses [7]-[10] or broadband incoherent light [11]-[13] have the ability to utilize bipolar codes, which increase the processing gain compared to earlier optical CDMA schemes limited to unipolar codes. Unlike TDM and WDM where signals are shared in time and in wavelength respectively, in CDMA signals are overlapped in both time and frequency. TDM and WDM can be classified as *scheduled multiple-access* techniques, as different users access the medium according to fixed assignment. CDMA, on the other hand, is a *random multiple-access* technique, which allows users to access any channel at any arbitrary time. The main advantage of optical CDMA compared to other multiple-access schemes is the relaxed requirements for wavelength stabilization (as in WDM) and freedom from network synchronization (as in TDM). Furthermore, in the optical CDMA encoding and decoding are inherently implemented by the use of optical processing, which allows implementation of some network operations, such as addressing, routing, and security, directly in the optical domain.

The radio frequency CDMA employed in cellular communication is a spread-spectrum technique where each signal bit is encoded into many bipolar "chips" of value 1 or -1 in time domain. Consequently, the bandwidth is spread. In analogy to RF spread spectrum, ultrashort pulse CDMA system based on frequency-domain encoding and decoding (spreading and despreading in time domain) of femtosecond coherent optical pulses [7]-[10] is a *spread-time* technique. The spectrum of femtosecond pulses is divided into many small units (according to the code length) and each frequency unit is assigned with phase 0 or π according to code sequence applied. As a result, the femtosecond pulses is spread to lower intensity, picosecond pseudonoise bursts. Only the receiver decoders with the right codes can convert (despread) the noise bursts back to femtosecond pulses.

An ultrashort pulse CDMA system of N users can be operated in the following way [7]-[10]: N user stations are connected via an N×N star coupler and a common fiber channel. Each user station is equipped with a CDMA transmitter including a femtosecond pulse source and an encoder which converts femtosecond pulses into lower intensity, picosecond pseudonoise bursts. Encoded signals are broadcast to the receivers of all other stations. Only the intended receiver with a matching code can decode the encoded signals back into short pulses. Incorrectly decoded signals corresponding to the wrong code remain low intensity noise-like bursts which are eventually rejected by the optical thresholder.

Ultrashort pulse CDMA system was first proposed in 1988 [6]. Although such spectral encoding/encoding has been demonstrated at visible wavelengths using a pair of conjugate phase masks adjacent to each other [7]-[8] and theoretical modeling and numerical analysis have been performed [9], no experiments testing ultrashort pulse CDMA at the infrared wavelengths compatible to fiber-optic technology have yet been reported to date. In this research we aim at assembling a simple femtosecond pulse fiber-optic CDMA testbed operated in the 1.5 μm wavelength band to test the physical feasibility of this technique.

Figure 1.1 the schematic for our envisioned femtosecond pulse CDMA system. It consists basically of one transmitter-receiver pair connected with a common transmission fiber link. In the transmitter, a laser pulse source generates femtosecond pulses in the 1.55 μm band. A spectral filter following the laser source is used to tailor the signal bandwidth (or pulse width). The filtered pulses are then amplified by an Er-doped fiber amplifier (EDFA) to compensate the loss occurring in the coder and fiber transmission. The amplified pulses are then passed through an encoder for phase coding. The coded pulses propagate over a transmission fiber link which requires dispersion compensation to allow for broadband pulse transmission before entering the receiver whose first element is a decoder. If the decoder is programmed with a phase code which is the conjugate of that applied to the encoder, the encoded signals is restored to femtosecond pulses; if the pulse is improperly decoded (by a non-conjugate phase code), the pulse remains as a pseudonoise burst. The decoder is immediately followed by a second EDFA to boost the decoded signals for nonlinear thresholding.

To assemble such a single-user CDMA testbed, several component technologies have to be developed: 1) femtosecond optical pulse sources, 2) femtoseond optical amplifiers, 3) phase coding devices, 4) fiber dispersion compensation, and 5) nonlinear thresholders. The success of a CDMA system depends greatly on the performances of these individual component technologies as well as the integratablity and compatibility of these components. Three sub-systems, namely the femtosecond pulse encodind/decoding, the dispersion-compensated transmission fiber link, and the nonlinear thresholder, need to be characterized for their own performances and then integrated together one by one to form a CDMA testbed. This thesis research is devoted to the study of a few key building blocks of a femtosecond pulse CDMA, namely the femtosecond pulse source, the dispersion-compensated transmission fiber link, and the femtosecond encoding device, and their integration to the CDMA system.

A brief discussion these key component technologies is given below.

1. Femtosecond laser sources:

The very first task of the whole project is to construct a compact and stable femtosecond laser source. Mode-locked Er-doped fiber lasers are the ideal choice as the femtosecond pulse sources because Er fiber can produce pulses at 1.5 - 1.6 μm wavelength range (the lowest-loss transmission window in silica fibers) and they can be easily integrated with other fiber-optic devices due to their all-fiber nature. Here an all-fiber mode-locked Er-fiber ring laser was built. The ring cavity configuration makes possible unidirectional operation and thus increase the stability of mode-locking operation. The pulses generated from this laser source are subsequently used to study the dispersion compensation and coding technologies.

As a CDMA pulse source, the mode-locked fiber laser has to be designed to have a suitable bandwidth and average power for CDMA operations. Although larger bandwidth can accommodate more user channels, it also produces more severe fiber dispersion. Balancing the trade-off, bandwidths of 10 to 15 nm are the choice of our CDMA working bandwidth. Instead of engineering a mode-locked laser with a desired bandwidth, here we built a laser with a much wider bandwidth ($\sim$60 nm) and spectrally tailored the bandwidth to suit our needs. The original shorter pulses can be used as reference pulses for cross-correlation measurements. As for the laser power, we want it as low as possible in the transmission fiber so that the nonlinear effects can be negligible but in the meantime we also want it sufficient for measurements and for the nonlinear thresholding operation. As a result, an power attenuator and two optical amplifiers have to be installed in the proper locations of the system.

2. Fiber dispersion compensation techniques:

Group velocity dispersion in fiber is probably the most important problem to solve in femtosecond CDMA. Without dispersion compensation, femtosecond pulses cannot propagate very far before they are very much broadened. For example, a 100-fs

pulse will double its width after propagating only 0.18 meters over standard single-mode fiber (SMF). For pulses in the femtosecond regime, simultaneous compensation of second- and third-order dispersion is necessary. Here we use a dispersion-compensating fiber (DCF) technique, which is very simple in concept and in implementation, to compensate the dispersion acquired from propagation over SMF. The DCF with favorable dispersion characteristics can not only compensate second-order dispersion completely but also greatly reduce the third-order dispersion of the SMF. This SMF-DCF technique is first tested over a short length of fiber (42 m) using very short pulses (62 fsec) from the mode-locked fiber laser. Longer fiber transmission of 2.5 km is subsequently demonstrated using longer pulses (250-fsec pulses from spectral slicing of original 62-fsec pulses). Stretch/recompression ratio of 800 is demonstrated over this 2.5-km fiber tranmission. This is the first time DCF technique being applied to pulses on the femtosecond scale. The dispersion compensation using DCF as we will demonstrate in a later chapter is not only applicable to CDMA networks but also very useful to other communication systems involved with broadband signals, such as high-speed TDM [1] and chirped-pulse WDM [14].

The 2.5-km dispersion-compensated SMF-DCF link served as the transmission fiber of our CDMA system. Although this fiber link is tested and optimized using femtoseond pulses, in CDMA operation it's the encoded pulses (low-intensity noise-bursts) which propagate over the link. However, as long as the nonlinear effects are negligible in the femtosecond pulse transmission, the link is also optimized for coded pulses and the encoded pulses after fiber transmission can be restored to oringinal femtosecond pulses with proper decoding.

3. Femtosecond encoding devices:

The coding devices we use here are programmable pulse shapers which are capable of high-complexity pulse shaping through spectral phase filtering. They consist of the conventional grating-and-lens pulse shaping apparatus and an electronically programmable 128-element liquid crystal phase modulator (LCM) in the Fourier plane. The encoder and decoder pulse shapers have to be made identical to ensure successful

restoration of encoded pulses to original pulses. In addition to being as a phase coding device the pulse shaper with a LCM can also be programmed to compensate the small residual dispersion of the SMF-DCF link. As we will demonstrate in Chapter 4, the residual dispersion of the fiber link is almost removed and a distortionless 2.5-km fiber transmission for sub-500-fsec pulses is achieved.

After all above three components and other CDMA components, such as EDFAs and nonlinear thresholder, are successfully developed and tested, they will be assembled as a single-user CDMA testbed for proof-of-concept experimental studies at the system level. The contrast ratio (between properly and improperly decoded pulses) obtained from this single transmitter/receiver pair provides a baseline estimate for the signal-to-noise ratio performance of multiple-access systems. This thesis is organized in this way:

In Chapter 2, we will first review a few techniques for generating ultrashort pulses in fiber lasers and then describe in detail the operational principles and characteristics of our laser pulse source- a stretched-pulse mode-locked Er-doped fiber ring laser.

In Chapter 3, the effect of group velocity dispersion in fiber is first reviewed. Dispersion compensation technique using a special dispersion compensating fiber (DCF) was first tested and characterized over a short length of fiber. Longer fiber transmission (2.5 km) was subsequently demonstrated for sub-500-fec pulses using the same SMF-DCF scheme.

In Chapter 4, Femtosecond encoder and decoder made of a conventional grating-and-lens pulse shaper and a liquid crystal modulator array are built. Spectral phase encoding and decoding are successfully demonstrated. Such coding device is also used to further compensate the residual dispersion of 2.5-km SMF-DCF link.

In Chapter 5, we describe the integration of the above three components with other CDMA component to form a single CDMA transmitter/receiver pair for system study.

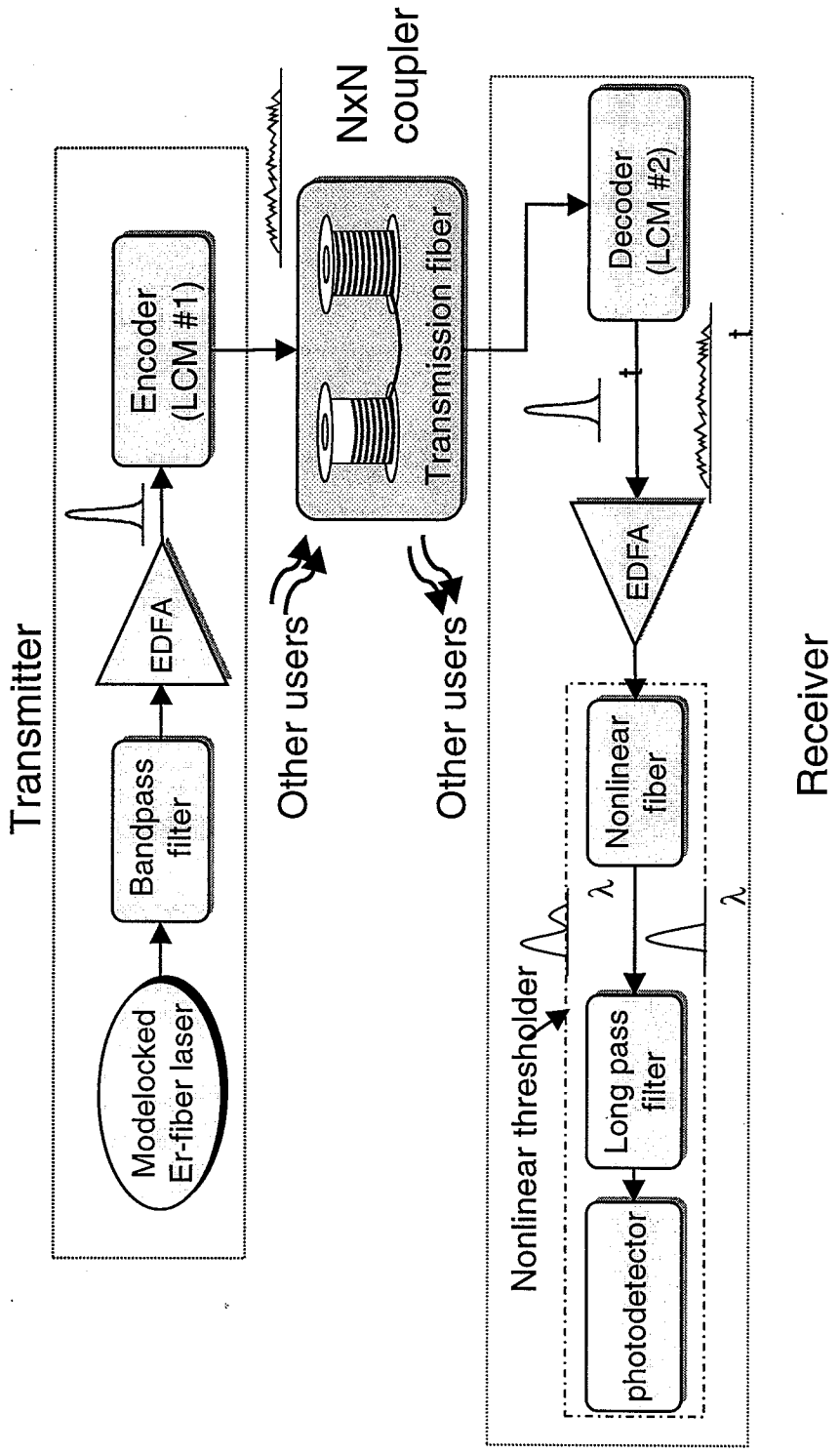

Fig. 1.1. Schematic block diagram of an femtosecond pulse CDMA

2. FEMTOSECOND FIBER LASER

Ultrashort optical pulses have found many applications in a variety of fields, such as time-resolved spectroscopy, high-energy physics, and optical signal processing, because of their short time duration and high peak intensity. Interest in utilizing ultrashort pulses in optical fiber communication increases over recent years due to the advance in short-pulses fiber lasers and fiber amplifier technologies. Ultrashort lightwave pulses are potentially ideal signal sources for high speed optical communication because more information can be packed into a given time interval and the large bandwidth associated with the ultrashort pulses. Femtosecond pulses generated from Er-doped fiber lasers are of most interest because they offer compatible all-fiber systems and, most of all, they operate near 1550 nm, the wavelength region in which silica fibers suffer least loss.

2.1 Passive Mode Locking in Fiber Lasers

The fundamental technique used for generating ultrashort pulses is mode locking [15]. Mode locking occurs when the various longitudinal modes in a laser cavity are "locked" together with a phase coherence among them. The more modes are synchronized in phase the shorter the pulses become. In active mode locking, an externally driven modulating element has to be placed within the cavity to induce phase coherence. Passive mode locking, on the other hand, is an all-optical nonlinear technique without requiring an active component. For fiber lasers, the passive mode locking techniques, especially those utilizing optical Kerr effect, are preferred ones for the generation of shortest possible pulses because it can take advantage of the full bandwidth of fiber lasers.

The pulse shortening mechanism of passive mode locking can be easily understood by considering the operation of a nonlinear optical element generally regarded as a saturable absorber. When an optical pulse travels through a fast saturable absorber the wings of the pulse suffer more loss than the central part where the intensity is high enough to saturate the absorber. As a result, pulses get shortened passing through the absorber. A variety of methods have been studied to employ the fast saturable-absorber-like mechanism to mode lock Er-doped fiber lasers. While real saturable absorbers made of semiconductor multiple-quantum-well devices have been used to achieve mode locking in solid-state laser [16] and fiber laser [17], the majority of mode locking techniques in fiber lasers can be categorized as interferometric or additive-pulse mode locking (APM) [18]. The fast saturable-absorber-like action is achieved by means of intracavity intensity-dependent refractive index [or self-phase modulation (SPM) effect] resulted from the Kerr nonlinearity. In its simplest form, APM action is a nonlinear amplitude modulation produced by the interference of two self-phase modulated pulses. The pulse shaping is achieved when the nonlinear phase shift leads to constructive interference near the peak of the pulse while the wings experience destructive interference. APM action is usually achieved in fiber lasers through two mechanisms. The first is using a nonlinear amplifying loop mirror (NALM) [19, 20]. By placing a gain medium, usually an Er-doped fiber, asymmetrically within it, the fiber loop acts like mirror which provides intensity-dependent transmission (or reflectance) characteristics. The figure-8 laser is one of this type [20]. The second is to use nonlinear polarization rotation to carry out APM action [21, 22]. Here the intensity-induced birefringence in optical fiber is the cause for nonlinear polarization evolution which eventually leads to passive amplitude modulation. Two cavity configurations, namely linear Fabry-Perot cavity and ring cavity, have been used. The ring configuration has the advantage of low scattering and reflecting loss because the unidirectional operation it can provide. As for the femtosecond pulse source for our CDMA experiments, source in our experiments, we adopt the nonlinear polarization rotation APM mechanism in a all-fiber ring cavity configuration.

2.2 Stretched-pulse Mode-locked Erbium Fiber Ring Laser

Figure 2.1 shows the schematic configuration of our all-fiber APM ring laser, adapted from the system developed by Tamura [22]. An erbium(Er)-doped fiber was used in the laser cavity as a gain medium to provide lasing in the 1.5 μm band. Erbium ions (Er^{3+}) were pumped by 980-nm Ti:sappire laser launched through a wavelength-division-multiplexed (WDM) coupler to the excited states, creating a population inversion which can produce stimulate emission for signals between 1525 nm to 1565 nm. The 80/20 output coupler was used to extract output pulses through the 20% port. A fiber-optic polarization-sensitive isolator following the output coupler ensures an unidirectional propagation and in the mean time functions as a polarizer. A polarization controller inside the cavity can be adjusted to change the polarization state of the light and is the key element to initiate mode locking. It is constructed by looping a piece of fiber around three disks of 2 inches in diameter. The stress-induced birefringence through the polarization controller can change the linearly polarized light into some arbitrary elliptical polarization. The mode locking mechanism of such laser configuration can be explained as follows. The light leaving the isolator/polarizer was linearly polarized and then changed to elliptical polarization after the polarization controller. This elliptically polarized light can be regarded as the sum of two circularly-polarized components (clockwise and counterclockwise) of different magnitude. The two components will travel at different velocity because of the intensity-dependent nonlinear refractive index of fibers. As a result, the orientation of the polarization ellipse is not fixed but evolving along fiber propagation. In short, the SPM in the fiber rotates the polarization ellipse. The isolator/polarizer transforms the rotation of ellipse in to amplitude modulation. Pulse shortening mechanism is realized by adjusting the polarization controller such that the polarizing isolator lets pass the central intense part and blocks the low-intensity wings. This technique is a varied form of APM in which the two circularly-polarized components play the roles of two interferometer arms.

The theoretical modeling of the pulse-formation process in the passive mode locking is in fact quite complex. A master equation was formulated using an analytical model in which nonuniformities and localized perturbation were distributed over the cavity length [23]. The effects of various parameters to the pulse formation were investigated in the solution to the master equation, which is a chirped secant hyperbolic function. Of all the parameters, the SPM and group velocity dispersion (GVD) are the most important factors in deciding the pulse characteristics such as pulse width, pulse energy, and mode locking stability. For example, it's well known that the balance between SPM and GVD can give rise to soliton pulses.

In constructing our all-fiber ring laser, the lengths of fibers were tailored to adjust the overall GVD of the cavity and the amount of SPM. A conventional single-mode fiber (SMF) has anomalous dispersion ($\beta_2 = 20\,ps^2/km$) at 1550 nm while the Er-doped fiber used here was estimated to have normal dispersion ($\beta_2 = 35\,ps^2/km$). The laser can be mode locked over a wide range of fiber length configuration but not all of the configurations result in mode-locked pulses with operating characteristics needed for our CDMA pulse source, such as self-starting, self-sustaining, stable mode locking , and sufficiently wide range of single-pulse operation. It was at first believed that negative-dispersion (or anomalous-dispersion) cavity was necessary for mode locking because of soliton formation [19]-[22]. However, later experiments in which 77-fs pulses were produced from a stretched-pulse mode-locked APM fiber laser with an positive (normal) overall dispersion proved that negative dispersion is not required and not necessarily beneficial because it limits the width and energy of mode-locked pulses [24, 25]. The Er-doped fiber in this case was not only the element providing gain but also the one contributing large positive overall dispersion. We adopted this stretched-pulse concept by adding a piece of special dispersion compensating fiber (DCF) with a large positive dispersion ($\beta_2 = 94\,ps^2/km$) to our cavity. From soliton area theorem, the pulse width is determined once the peak power is clamped due to saturation of APM mechanism. Therefore, the pulse energy is fixed to a certain value called fundamental soliton energy. With the addition of a positive-dispersion fiber

where soliton can't be sustained, this energy restraint is released and pulses with larger energy and bandwidth can be produced. Because of the presence of both negative (SMF) and positive (DCF) dispersion fibers, the pulse is temporally stretched and compressed in round trip. This lowers the average peak power and therefore reduces the excessive nonlinearity compared to that would be experienced by pulses close to transform limit (such as soliton pulses) and help avoid APM saturation. As a result, pulses can accommodate more amplification and achieve higher energy. This is basically similar to chirped-pulse amplification technique.

As shown in Figure 2.1, the final configuration of our fiber laser is a stretched-pulse mode-locked fiber ring laser consisting of a WDM coupler, a Er-doped fiber (190 cm), a polarization controller, a 20/80 output coupler, a dispersion compensating fiber (65 cm), and a polarization-sensitive isolator connected in the order specified. The WDM coupler, output coupler, and isolator are all fiber pigtailed devices with SMF as leads. The total length of the cavity (6.45 m) consists of 190 cm of Er-doped fiber, 65 cm of DCF and 3.9 m of SMF, resulting in an overall cavity dispersion-length product of $\sim +0.05ps^2$.

This laser generates a stable train of femtosecond pulses at a 33 MHz repetition rate, with one pulse per cavity round trip time. The mode locking is self-starting with threshold of ~140 mw of 980-nm pump beam. Single-pulse operation region occurs for pump powers of 60-240 mw. The average output power is ~2 mw giving single-pulse energy of 60 pJ when pumped with 180 mw. The pulse energy is approximately increased linearly with pump power in the single-pulse regime. The low power conversion efficieny (180 mW pump generating only 2 mW output) may be because first the Er fiber used here is not of high efficiency and secondly the splicing losses of two SMF/DCF joints in the cavity are high. The power spectrum of the mode-locked pulses, as shown in Figure 2.2, is recorded by an optical spectrum analyzer. The spectrum with a full-width at half-maximum (FWHM) bandwidth of 55 nm exhibits several interesting features: sharp peaks at 1560 nm and 1610 nm, as well as clear sidelobes at 1510 and 1645 nm. These features may be evidence of

optical wave-breaking [26] occurring within our laser cavity, a nonlinear phenomenon which can only occur in a highly normal-dispersion environment.

2.3 Pulsewidth Measurement

The output pulses emitted from the ring cavity are in the femtosecond time scale which is too fast to be temporally resolved by the combined use of photodetectors and oscilloscopes. An indirect measurement techniques utilizing second harmonic generation (SHG) signals is used here to estimate the pulse width [27]. The measuring apparatus is basically a Mach-Zender interferometer as shown in Figure 2.3.

For autocorrelation the input pulse is split into two, one to signal arm of fixed length and the other to reference arm whose length is adjusted by a motorized translation stage with 1 μm resolution (corresponding to 6.6 fs in time). A stepper-motor controller moves the stage linearly to scan over a desired time interval. The two retroreflected beams are recombined in a noncollinear but parallel (in horizontal plane) configuration and focused on a SHG crystal ($LiIO_3$ of 1 mm in thickness). A photomultiplier tube (PMT) is used to detect the SHG signals. The aperture of the PMT is adjusted such that only the SHG signal generated from the overlap of the two beams are captured and those generated from either beam are blocked out. The signal from PMT is sent to lock-in amplifier for data acquisition. A computer software is used to control the scan time, acquire and process data. The signal at PMT is a direct measurement of second-order correlation function $G^{(2)}$ defined as

$$G^{(2)}(\tau) = \langle I(t)I(t+\tau)\rangle,$$

where τ is the time delay between the two pulses. The SHG signal is maximized when the two arms are exactly matched and thus the two pulses are completely overlapped (τ=0). The SHG signal decreases as the two pulses move away from each other. Therefore, from the intensity of SHG signals versus time delay we can deduce the widths of the pulses if the pulse shape is assumed. For example, for the secant hyperbolic pulses ($Sech^2$) the deconvolution factor is 1.55 while for the Gaussian

pulses it is 1.4. The output pulses emitted from the ring cavity are in general not at its transform-limited width. The chirp is compensated by adjusting the fiber length of the output coupler to obtain the possible shortest autocorrelation trace. Figure 2.4 shows the autocorrelation trace of the optimally chirped-compensated output pulse. The FWHM is 95 fsec corresponding to a deconvolved pulsewidth of ~62 fsec if the secant hyperbolic pulses are assumed.

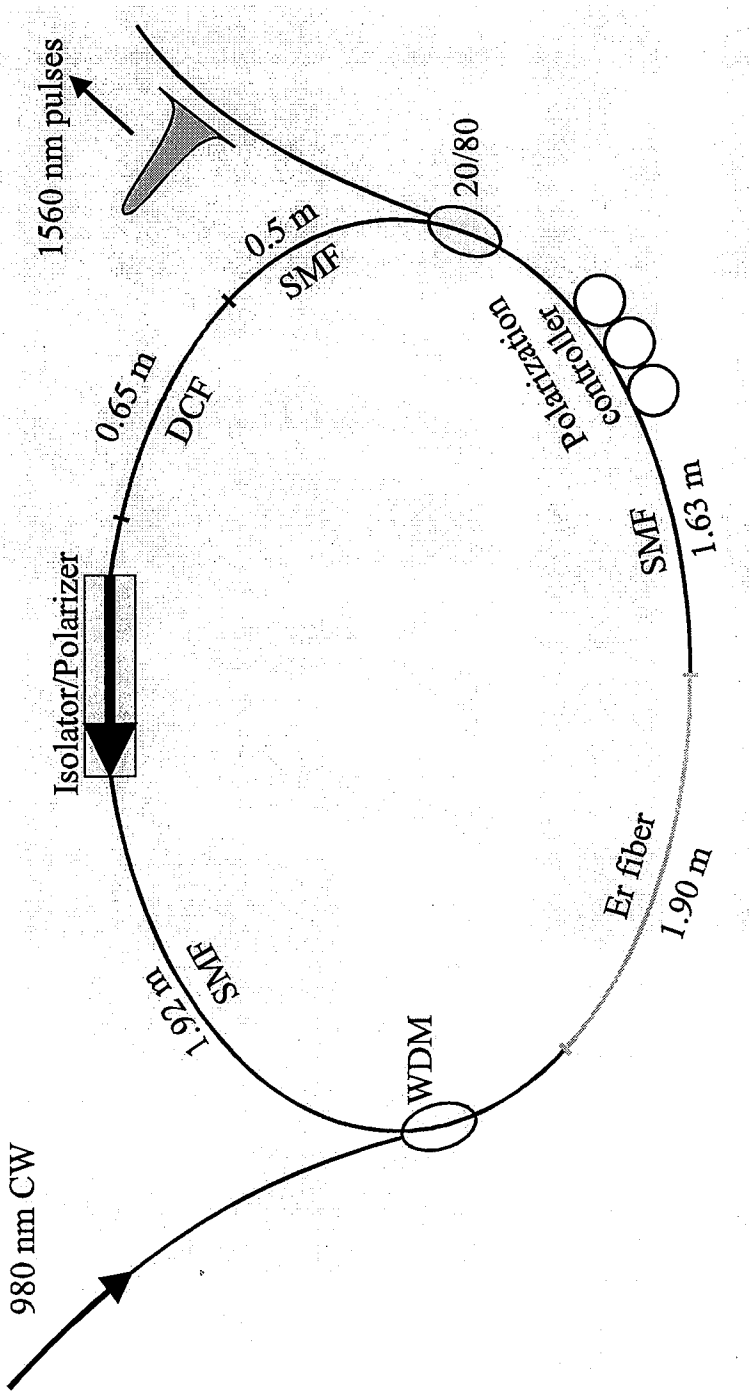

Fig. 2.1. Schematic of all-fiber Er-doped fiber ring laser. With the presence of DCF the overall dispersion of the cavity is normal and pulses are stretched and compressed during one round trip time.

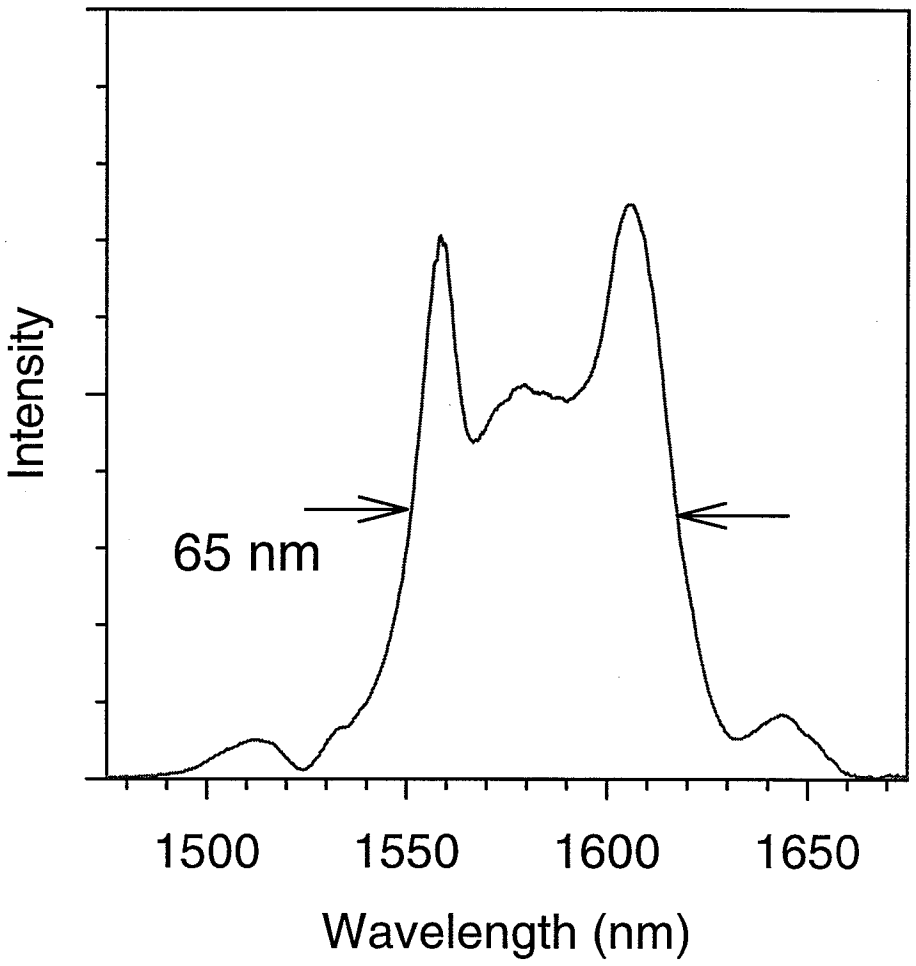

Fig. 2.2. Power spectrum from a stretched-pulse mode-locked fiber ring laser. Figure 2.1 shows the exact makeup of this laser. The FWHM is about 60 nm.

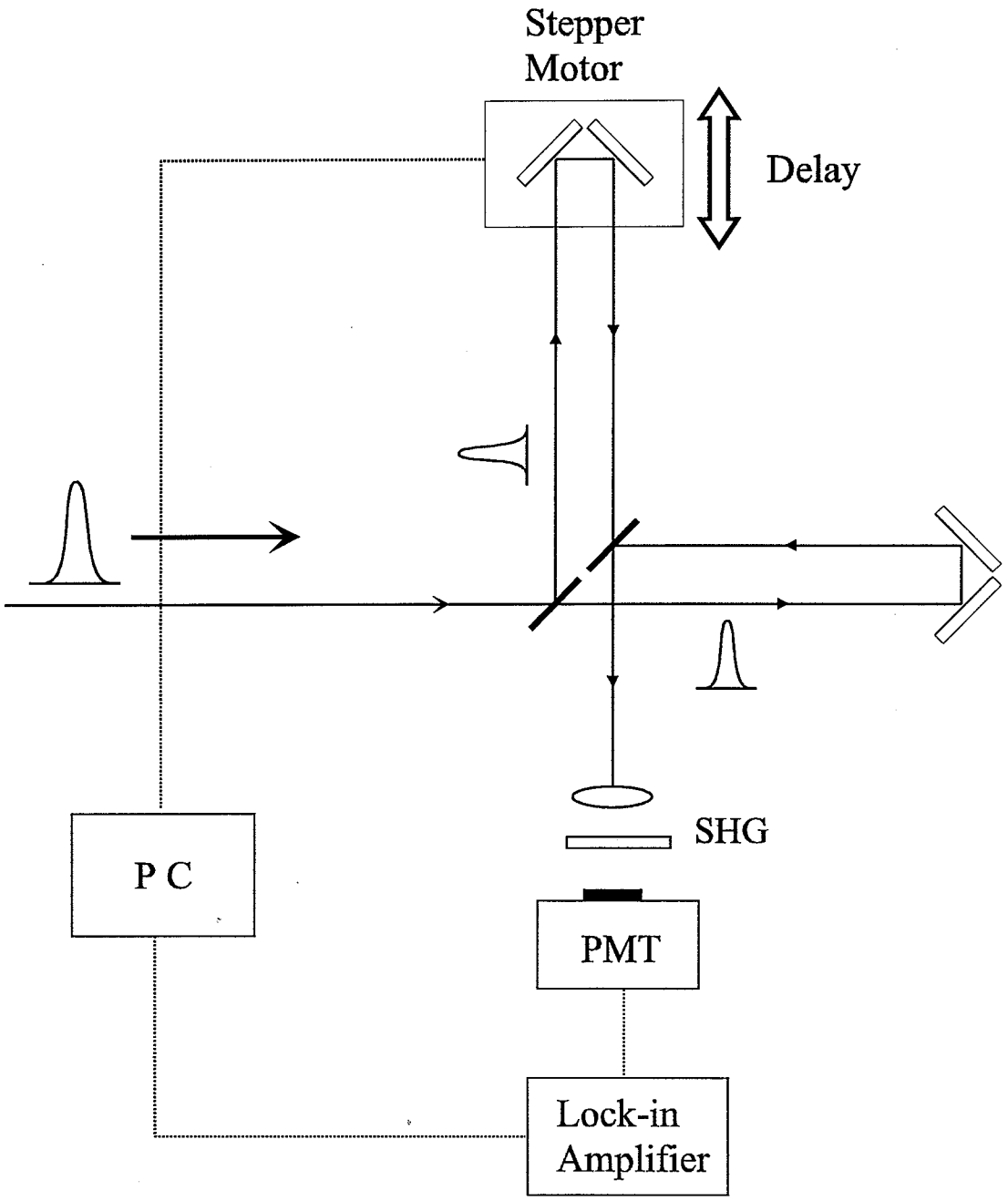

Fig. 2.3. Schematic diagram of a two-arm Mach-Zender intensity correlator. The linear delay is provided by a motorized translation stage.

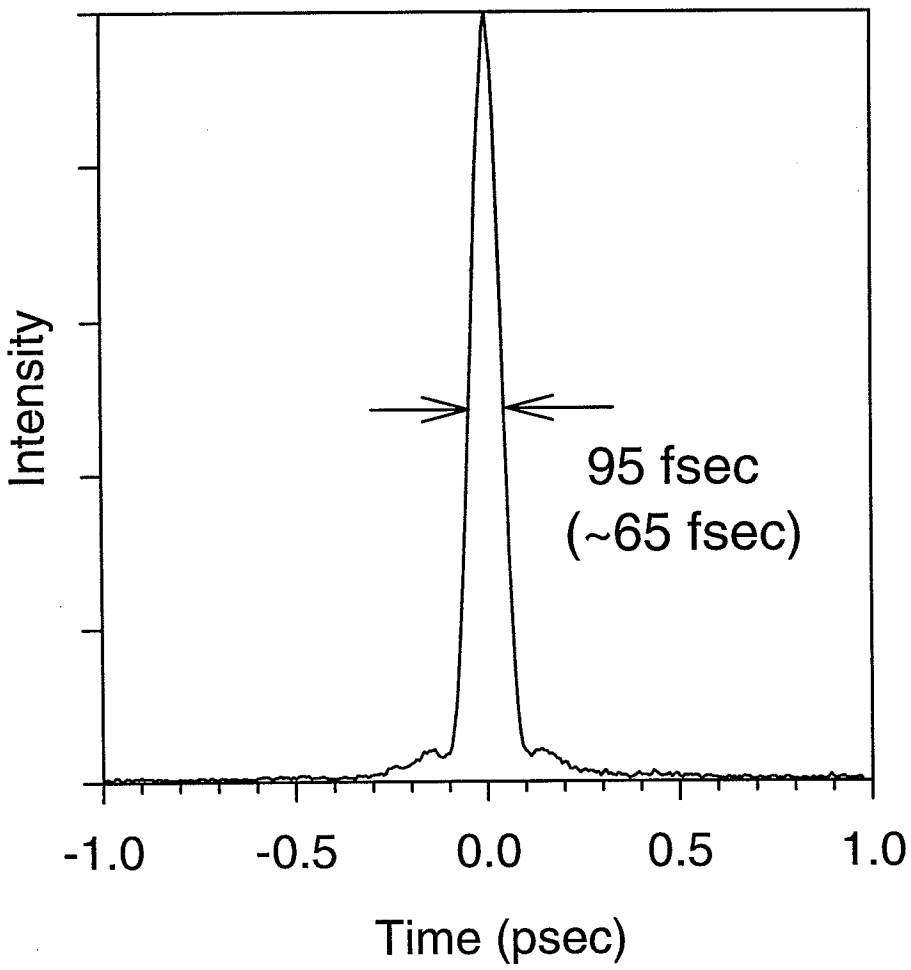

Fig. 2.4. Autocorrelation of pulses from the stretched-pulse mode-locked fiber ring laser shown in Figure 2.1. The 95-fsec autocorrelation width corresponds to a deconvolved pulsewidth of ~62 fsec.

3. FIBER DISPERSION COMPENSATION

With the advent of fiber amplifiers, fiber loss is no longer a fundamental limit for achieving long fiber transmission. As a result, fiber group-velocity dispersion (GVD) has become the major factor in limiting short pulse transmission. Fiber dispersion and dispersion compensation are then key issues for high-speed lightwave transmission systems, not only the femtosecond pulse code-division multiple-access (CDMA) systems [9, 10] we are investigating but also the time-division multiplexed (TDM) [1] and the wavelength-division multiplexed (WDM) systems [28]. For our CDMA system, nonlinear dispersion compensation schemes, such as soliton propagation using nonlinear self-phase modulation (SPM) to balance GVD, cannot be used because encoded pulses cannot propagate as solitons. The linear scheme we employ is using a special dispersion compensating fiber (DCF) to equalize the dispersion in conventional single-mode fiber (SMF).

3.1 Group Velocity Dispersion

The effects of GVD can be accounted for by expanding the group delay $T(\omega)$ per unit length, defined as $d\beta/d\omega$ (inverse of group velocity) about the center frequency ω_c as

$$T(\omega) = \frac{1}{v_g} = \frac{d\beta(\omega)}{d\omega} = \beta_1 + \beta_2 (\omega - \omega_c) + \frac{\beta_3}{2} (\omega - \omega_c)^2 + \cdots, \tag{3.1}$$

where

$$\beta_m = \left[\frac{d^m \beta}{d\, \omega^m} \right]_{\omega=\omega_c} \quad (m = 1, 2, 3, \cdots). \tag{3.2}$$

β_1 is the group delay for the center frequency ω_c, the time required for the center frequency component to travel unit distance. β_m is called the m-th order dispersion.

As frequency moves away from ω_c, the group delay deviates from β_1 on account of all orders of dispersion. Also, as pulses get shorter, the group delay spread increases because the spectral spread $(\omega - \omega_c)$ increases. Therefore, the dispersion effects increase as the pulse width decreases. Dispersion effects are also often expressed in terms of the variation in the group delay with respect to deviations in *wavelength* as follows:

$$D(\lambda) = \frac{dT(\omega)}{d\lambda} = \frac{d}{d\lambda}\left(\frac{d\beta}{d\omega}\right) = D(\lambda_c) + D'(\lambda_c)\,(\lambda - \lambda_c) + \cdots. \tag{3.3}$$

Here $'$ means derivative with respect to wavelength λ. $D(\lambda_c)$ and $D'(\lambda_c)$ are called dispersion and dispersion slope respectively (sometimes referred to as second- and third-order dispersion as well). β_2 and β_3 are closely related to D and D' as [29]

$$D = -(2\pi c/\lambda^2)\,\beta_2 \tag{3.4}$$

$$D' = (2\pi c/\lambda^2)^2\,\beta_3 + (4\pi c/\lambda^3)\,\beta_2. \tag{3.5}$$

$\beta_2 > 0$ $(D < 0)$ is called normal dispersion, while $\beta_2 < 0$ $(D > 0)$ is denoted anomalous dispersion. In the normal-dispersion regime, the higher frequency components of a pulse travel more slowly than the lower frequency components. The opposite occurs in the case of anomalous dispersion. Both kinds of dispersion broaden the pulses and introduce a frequency chirp (approximately linear when the second-order dispersion dominates). The difference is that the chirp is of opposite direction. For anomalous dispersion the instantaneous frequency decreases across the pulse (negative chirp). The frequency chirp caused by SPM effect is positive. Therefore, soliton can form in the anomalous-dispersion regime because of the balance between dispersive effects (GVD) and nonlinear effects (SPM). The basic idea of dispersion compensation is to provide a mechanism to balance the frequency chirp.

3.2 Dispersion Compensation Techniques

A variety of dispersion compensation techniques have been investigated, mostly for the purpose of upgrading embedded standard single-mode fibers (SMF) with a

large anomalous [illegible] at 1.55 μm), for use in the state-of-the-art 1.55 μm systems experiments operating at ~10 Gbit/s and above. These include techniques utilizing [illegible] [30]-[33], bulk grating-and-[illegible] [illegible] dispersion compensating fibers [39]-[42]. In addition, [illegible] fiber experiments exploring linear dispersion [illegible] beginning to appear. For pulses in the femtosecond regime, simultaneous compensation of both second- and third-order [illegible] is necessary [34, 43]. One [illegible] persion and partial dispersion slope compensation for [illegible] of 340 nsec pulses over 40 km of fiber to [illegible] ped fiber Bragg gratings [illegible] third-order dispersion for [illegible] 7.9 km of dispersion-shifted fiber (DSF) [31]. Recently, [illegible] fiber gratings with a high reflectivity bandwidth of ~5.2 nm have been used for dispersion compensation in 40 Gb/s system [illegible] The high reflectivity bandwidth still appear to limit these devices to picosecond applications [33]. Transmission of [illegible] respectively over 400 m and 3.2 [illegible] which can simultaneously [illegible] operating at wavelengths shorter than the fiber zero dispersion wavelength (λ_0). For the fiber transmission of femtosecond pulses in our (3.2)-(3.3) experiments, we employed the dispersion compensating fibers (DCF) method to compensate the dispersion of SMF because it provides an all-fiber system and is very simple in concept and in implementation.

3.3 [illegible]

The idea of using special dispersion compensating fiber (DCF) to compensate the dispersion in SMF was proposed as early as 1980 [44]. Early dispersion compensation experiments [38]-[41] used relatively long pulses (≥10 ps) and DCF

with negative (or normal) dispersion (opposite to of SMF) but positive dispersion slope (same as SMF) in the 1550 nm wavelength range. Consequently, although the second-order dispersion of the composite fiber link was compensated, the third-order dispersion was increased. Such DCFs are not desirable for femtosecond pulse propagation. In our experiments, we are interested in extending the dispersion-compensating fiber technique to achieve simultaneous second- and third-order dispersion compensation for femtosecond pulses. The possibility of simultaneous dispersion and dispersion slope compensation were first demonstrated using higher-order fiber modes to enable broadband dispersion compensation for several WDM channels [42]. Here we employ a single-mode DCF which exhibit both negative dispersion and *negative* dispersion slope [45] for femtosecond pulse dispersion compensation.

Our scheme of using dispersion compensating fibers (DCF) is to concatenate a SMF with a DCF whose dispersion is equal in magnitude and opposite in sign to that of the SMF. As a result, the pulses broadened by SMF were recompressed by the DCF, as schematically illustrated in Figure 3.1 (a). The concatenated SMF-DCF fiber link can be characterized by an equivalent dispersion D_{eq} which is equal to the overall dispersion averaged over the total length of the fiber link. The equivalent dispersion is then given by

$$D_{eq}(\lambda) = \left[R * D_{SMF}(\lambda) + D_{DCF}(\lambda)\right] / (1 + R) \tag{3.6}$$

where R is the length ratio of the SMF to DCF, D_{SMF} is the dispersion of the SMF and D_{DCF} is the dispersion of the compensating fiber. Since the conventional SMF has a positive (anomalous) dispersion $D(\lambda)$ and a positive dispersion slope $D(\lambda)'$ at 1550 nm wavelength range, a favorable DCF should be a single-mode fiber with a large negative (normal) dispersion and a negative dispersion slope. Such a DCF can be achieved by the proper design of the refractive index profile [45]. When concatenated with a SMF, such a DCF not only eliminates dispersion at certain wavelength but also significantly reduces the overall dispersion slope, as illustrated schematically

in Figure 3.1(b). Complete elimination of the second- and third-order dispersion simultaneously requires DCF satisfies the following relation:

$$\left(\frac{D'(\lambda_c)}{D(\lambda_c)}\right)_{DCF} = \left(\frac{D'(\lambda_c)}{D(\lambda_c)}\right)_{SMF}. \tag{3.7}$$

In practice it is difficult to make such a perfectly matched pair of SMF and DCF. When D'/D of the DCF is smaller (larger) than that of SMF, the concatenated SMF-DCF link has a residual positive (negative) overall slope D'. Therefore, with the combination of two DCFs, one with D'/D larger than SMF and the other with smaller D'/D, completely compensation of the dispersion and dispersion slope for a wide wavelength range should be possible since both DCF lengths can be adjusted, providing one more degree of freedom to adjust the overall dispersion. The residual dispersion of a SMF-DCF link can also be further compensated by other schemes, such as gratings-and-lens pulse shapers and chirped fiber Bragg gratings. As will be described in Chapter 4, the residual dispersion of our SMF-DCF is almost completely removed by the use of a programmable pulse shaper with a phase modulator.

3.4 Preliminary Experiments: 42-m Dispersion-Compensated SMF-DCF Link

The dispersion properties of the SMF and DCF used in our experiment were known to us to a very limited extent (only dispersion at a few wavelengths were measured with low precision). To learn more about the dispersion characteristics of these two fibers before we engage in long fiber transmission, we performed a preliminary test over a short length of SMF-DCF fiber link using very short pulses (62-fsec pulses from our stretched-pulse mode-locked Er-fiber ring laser). This experiment using extremely short pulses propagating over rather short fiber lengths may be of immediate interest for femtosecond chirped pulse fiber amplifier systems which have previously been limited to pulses ~400 fsec in duration [30] and also serve as an extremely sensitive test for femtosecond dispersion compensation and measurements of small amounts of residual dispersion in the compensated fiber link. The results of our

measurements can be used to extrapolate dispersion compensation performance for somewhat longer pulses (a few hundred fsec) over fiber links in the kilometer range which is suitable for our CDMA applications.

As illustrated in Figure 3.2, the basic idea of our experiments is to propagate low power femtosecond pulses through a concatenated SMF-DCF link and then measure the resulting output pulses. The 62-fsec pulses generated from the stretched-pulse mode-locked Er-doped fiber ring laser described in Chapter 2 are split into two using a 20/80 fiber coupler. The beam from the 80% port is sent to a concatenated fiber link (about 42 meters total) consisting of SMF and DCF. We measure the pulses propagating through this fiber link (which we denote signal pulses) by performing intensity cross-correlation measurements with the 62-fs reference pulses which emerge out of the 20% port of the fiber coupler. Two fiber polarization controllers (PC) were utilized in order to optimize the polarization of the signal and reference pulses for the best second harmonic signal in the correlator. The average optical power sent to the concatenated fiber link is 0.65 mw, corresponding to a peak power of 275 W ($\sim$2.8% of the N=1 soliton power for 62-fsec pulses in SMF) at the input of to the fiber link. Because the pulse width broadens rapidly in the first few meters of propagation, accumulated nonlinear phase shifts are expected to be very small, which means we are operating in the linear transmission regime as desired.

The output pulses from the SMF-DCF link are measured by an intensity cross-correlator obtained by modifying (inserting the output signal into the path stationary arm) the Mach-Zender auto-correlator described in Chapter 2. The length two arms of the correlator are matched in the sense that the #N pulse is correlating the #N+6 pulse. To minimize the overall link dispersion, we performed a series of cross-correlation measurements in which the lengths of SMF and DCF were iteratively adjusted and fine-tuned in order to reduce the duration of the output signal pulse. Figure reffig3:ratio shows the output pulsewidth as a function of the length ratio of SMF to DCF. The cross-correlation trace of the shortest output pulses is shown in Figure 3.4 (a). The correlation width is 125 fs FWHM, corresponding to a

deconvolved pulse duration of ~110 fs, which is within a factor of two of the reference pulse duration. Although we did not measure the pulses after the SMF section alone, we calculate that the pulses should be broadened to ~35 ps at this point. By virtue of the DCF, the final output pulse is recompressed by a ratio of 300. In order to illustrate the magnitude of pulse stretching and successful recompression, Figure 3.5 shows the trace of the optimally recompressed signal pulse together with the calculated broadened 35-ps pulse (the intensity of the 35-ps pulse is magnified 20 times in order to be discernible). The shortest output pulses are obtained for an optimal fiber length ratio R_{opt} ~4.57 (34.7 m / 7.6 m). As shown in Figure reffig3:ratio, the pulse duration increases by 10% when the length ratio is changed by ~0.15%. This indicates that accurate adjustment of the length ratio is important for the success of the DCF technique, as expected for our case of very high recompression ratio.

As shown in Figure 3.4, there is a small oscillation in the trailing tail of the output pulse, a phenomenon typical of positive third-order dispersion. This means that the second-order dispersion of the fiber link is almost completely compensated and the residual dispersion is dominated by third-order dispersion. To quantitatively characterize the performance of the DCF, the magnitude of this residual third-order dispersion and the zero-dispersion wavelength should be measured. However, since intensity cross-correlation measurements do not provide any phase information and since the laser power spectrum is of an irregular shape, it's difficult to make accurate estimates for the residual dispersion and zero dispersion wavelength from the intensity profile of the output pulse alone. In the next section we will present a spectral interferometry technique which is capable of measuring both phase and amplitude in order to characterize the residual dispersion of the fiber link.

3.5 Fiber Dispersion Measurements Using Spectral Interferometry

Fiber dispersion can be measured by a number of measurement techniques, as reviewed in [46, 47]. These include time-of-flight measurements and related frequency domain phase shift measurements, as well various interferometric measurements. The

time-of-flight and related techniques generally require a minimum of one kilometer of fiber in order to obtain reasonable precision with sufficient wavelength resolution. The interferometric techniques, either time-domain interferometry or spectral interferometry, are usually performed with very short fiber lengths on the order of one meter. This limitation stems from the need for a free-space reference arm with a delay equal to that experienced in the fiber. Here we demonstrate the use of spectral interferometry to characterize the 42-meter dispersion-compensated SMF-DCF fiber link. To our knowledge this is the first time that spectral interferometry has been used for measuring a fiber as long as tens of meters.

Spectral interferometry measurements can be performed using either incoherent or ultrashort pulse light sources. Incoherent white light sources have been applied principally for characterization of short ($\sim$1 m) single-mode fibers [48, 49]. Coherent ultrashort pulse sources have been applied, for example, to measure self-phase-modulation [50] and polarization mode dispersion [51]. Spectral interferometry measurements using ultrashort optical pulses have also become popular for measurement of various bulk optical systems used in ultrafast optics applications [52]. Here we apply ultrabroadband (>50 nm) femtosecond pulses from our modelocked fiber laser for fiber dispersion measurements. The periodic nature of the modelocked laser output allows us to correlate the pulses emerging from the fiber under test with pulses emitted substantially later from the laser. This eliminates the need for a long free-space reference arm and therefore leads to the ability to perform spectral interferometry measurements with much longer fibers. Our measurements reveal that the concatenated SMF-DCF fiber link has approximately zero second order dispersion and a reduced third order dispersion (dispersion slope) roughly six times smaller than that of dispersion shifted fiber.

Figure 3.6 shows the schematic of our femtosecond spectral interferometry measurements. As before, 62-fs pulses from the stretched-pulse-modelocked Er-doped fiber ring laser were split into the two arms of a Mach-Zender interferometer. One arm of the interferometer is a free space reference arm whose length can be varied

using a stepper motor driven translation stage to introduce a time delay τ. The other (signal arm) contains the optical system to be measured, which in our case is the 42-m dispersion-compensated SMF-DCF fiber link. If there are no nonlinear effects, the power spectrum $S(\omega)$ recorded by the optical spectrum analyzer at the output of the interferometer can be expressed as

$$\begin{aligned} S(\omega) &= \left| E(\omega)e^{j\omega\tau} + aE(\omega)e^{-j\phi_d(\omega)} \right|^2 \\ &= |E(\omega)|^2 \left\{ 1 + a^2 + 2a\cos[\omega\tau - \phi_d(\omega)] \right\}, \end{aligned} \tag{3.8}$$

where $E(\omega)$ is the spectrum of the 62-fs input pulse and a^2 is the power split ratio of the two arms. The argument of the cosine term in the above equation is the phase difference of the two arms (denoted as $\phi(\omega)$) which contains the linear phase shift $\omega\tau$ due to fixed time delay τ as well as the phase distortion $\phi_d(\omega)$ due to fiber dispersion. The optical path length of the reference arm is adjusted to equal that of the signal arm containing the fiber within a small adjustable delay τ, modulo the 30 nsec pulse repetition period of the laser pulses. In our experiments the signal pulses passing through the fiber correlate with the sixth successive pulses passing through the reference arm. This periodic correlation property of the modelocked laser circumvents the need for very long free-space delay arms and thus enables spectral interferometry to be applied to fibers more than an order of magnitude longer than previously. The setup used for intensity cross-correlation measurements in our dispersion compensation experiments in the previous Section can be easily modified for spectral interferometry measurements. As illustrated in Figure 3.2, both the signal and the reference beams are redirected by inserting a moving mirror in front of the SHG crystal and then coupled into a single-mode fiber patchcord connected to an optical spectrum analyzer (OSA) which records the spectrum of the superimposed pulses. Although the two beams are in a noncollinear configuration, the core of the single-mode fiber patchcord samples a spot smaller than a single spatial fringe and therefore maintains a high contrast spectral interference pattern. The biggest concern in our experiments is the need to ensure that the interferometer path difference does not drift during the course of a

measurement. In order to protect against such drift, we set the OSA for rapid scans, typically ~1-2 sec scan times over a 120 nm range, with a spectral resolution of 0.1 nm. We also checked for consistency by repeating each fiber measurement roughly ten times with various values of the delay τ.

As shown in Figures 3.7 (a) and (b), two examples of spectral interferograms were obtained for time delays of -2.9 ps (reference pulse ahead) and +1.7 ps respectively. Figures 3.8 (a) and (b) shows the inverse Fourier transform of the spectral interferograms in Figures 3.7 (a) and (b) respectively. Note that the main lobe (baseband) in Figures 3.8 (a) and (b) corresponds to the DC terms in Equation refeq:fringe while the sidelobes correspond to the modulating term (cosine term). Noise in the interferograms of Figure 3.7 can be suppressed by low-pass filtering (in the time domain); the results are shown in Figures 3.9 (a) and (b). The periodicity of the spectral fringes in Figure 3.9 should be inversely proportional to the constant time delay τ, as illustrated by the obviously different periodicities in Figures 3.9(a) and (b) which correspond to different time delays. Also note that the periodicity is not constant but varies slowly with frequency. These variations in periodicity arise from the phase distortions caused by the fiber dispersion; this is the information we would like to extract from the interferograms. These filtered interferograms are subsequently normalized by the spectrum of the input pulse, $|E(\omega)|^2$, in order to isolate the DC and the cosine terms in Equation 3.8. We then obtain the spectral phase $\phi(\omega)$ by locating the position of the maxima in the normalized filtered data and assigning a 2π phase shift between adjacent spectral peaks. The resultant phase vs. frequency data are fit to the following equation:

$$\phi(\omega) = \omega\tau - \phi_d(\omega) = b_0 + \tau(\omega - \omega_c) + \frac{\beta_2}{2} L\,(\omega - \omega_c)^2 + \frac{\beta_3}{6} L\,(\omega - \omega_c)^3 + \cdots, \quad (3.9)$$

where β_n is called the nth-order dispersion and L is the length of the fiber link. The linear phase term due to the fixed time delay, $\omega\tau$, is then subtracted to yield only the phase distortion $\phi_d(\omega)$ due to dispersion. Curves A and B in Figure 3.10 show the resulting phase shifts corresponding to $\phi_d(\omega)$ evaluated at the positions of the

spectral peaks in the data sets of Figure 3.9. The solid lines are the least-square fits of each data set to third order polynomials. From these data, as well as from several other measurements performed at different delays τ, the residual dispersion in the concatenated link is dominated by third-order dispersion with β_3 ~0.016±0.002 ps^3/km (D'~0.0088±0.001 ps/km/ nm^2)(which means ~85% of the dispersion slope of the SMF has been compensated) and with zero dispersion wavelength ($\beta_2 = 0$) at 1591±3 nm. This result is consistent with the intensity cross-correlation measurement shown in Figure 3.4 which displays an oscillatory trailing tail arising from this third-order dispersion. The measured third-order dispersion is roughly six times lower than that of dispersion-shifted fiber, where D'~0.05-0.06 ps/km/nm^2.

In order to further validate this spectral interferometry technique, we have also measured some short fibers with known dispersions. Curves C, D and E in Figure 3.10 show the measured results for three additional fiber configurations : 1-m dispersion-shifted fiber (DSF) spliced to 20-cm SMF, 1-m DSF spliced to 30-cm SMF, and 1-m DSF spliced to 10-cm DCF. The dispersion of SMF can be obtained from these measurements by taking the phase difference of curves C and D, which corresponds to the phase distortion caused by 10 cm of SMF. Similarly, the dispersion of the DCF can then be deduced from the difference of curves C and E after the dispersion of SMF has been obtained. Our measurements yield β_2~ − 21.0±1.5 (D~16.5 ps/km/nm) and 98.5±7.5 ps^2/km (D~77.3 ps/km/nm) at 1550 nm for SMF and DCF, respectively. Compared to the known second-order dispersions of SMF (β_2=-22 ps^2/km) and of this DCF (β_2=96 ps^2/km) at 1550 nm (obtained from the time-of-flight measurements), these results indicate that our spectral interferometry measurements yield accurate values for β_2, the leading-order dispersion term in these three fiber configurations. Therefore, we believe that the measured residual dispersion β_3 for the dispersion-compensated SMF-DCF link should also be valid, because third-order dispersion is the leading-order dispersion term for this compensated fiber link. Note that we directly measured the overall dispersion of the whole SMF-DCF fiber link, rather than

measuring the dispersion of the individual fibers separately and weighting them according to their lengths, because we are only interested in the overall uncompensated dispersion effect. Furthermore, measuring the whole link directly provides the most accurate estimate of the total link dispersion (which is dominated by third-order dispersion β_3), while in the individual SMF or DCF the β_2 is dominant.

To summarize for this section, we demonstrate the application of femtosecond spectral interferometry to measure the small residual third-order dispersion of a 42-m dispersion-compensated fiber link. By using a mode-locked pulsed source we were able to extend our spectral interferometric measurement technique substantially beyond the usual fiber lengths on the order of a meter. It should be possible to extend interferometric techniques to even longer fibers as well, limited ultimately by laser timing jitter.

3.6 2.5-km Dispersion-Compensated SMF-DCF Link

Substantially longer transmission distances should be possible with longer femtosecond pulses if the dispersion characteristics we have measured for the 42-m link can be scaled to longer concatenated SMF-DCF links. For a fiber link dominated by third-order dispersion, the propagation distance is proportional to the third power of pulse width for a fixed pulse broadening ratio [53]. Therefore, from the case of 62-fs pulses traveling over a 42-m SMF-DCF fiber link, we should expect a comparable pulse broadening ratio for 245-fsec pulses to propagate over a similar SMF-DCF link of 2.6 km in length. To demonstrate this, here we propagate 245-fs pulses over a 2.5-km dispersion-compensated fiber link made of the same SMF and DCF.

The 62-fsec pulses (power spectrum shown in Figure 2.2) used in the previous experiments can be spectrally tailored using a fiber-pitailed interference bandpass filter (20-nm FWHM centered at 1565 nm), as shown in Figure 3.11, to produce longer pulses. The center wavelength and bandwidth of the filtered spectrum can be tuned by rotating the interference filte. Figure 3.12 shows a filtered spectrum with a FWHM of ~9.8 nm, which would result in a transform-limited pulse width of 230

fsec. The modulation of ~1.2 nm in the filtered spectrum is likely due to the Fabry-Perot effect associated with the interference filter. The filtered pulses were measured to have pulsewidths of 245 fsec. Figure 3.14 (a) shows the cross-correlation trace of such filtered pulses with the original 62-fsec pulses as the reference. These filtered 245-fsec pulses with an average power of 50 μw at 33 MHz repetition rate are then sent to a ~2.5-km SMF-DCF fiber link. Similar to the the short fiber link case, the dispersion of the 2.5-km SMF-DCF link is optimized by adjusting the length ratio of the two fibers. To simplify the process, autocorrelation measurements (which do not require matching the lengths of the two arms of Mach-Zender correlator as would in the case of cross-correlation) were first performed to roughly dispersion compensate the link. Figure 3.13 shows a few autocorrelation traces corresponding to different SMF/DCF length ratios in the process of optimizing the link. Cross-correlation measurements were then used to fine tune the length ratio for final optimization. The cross-correlation traces of the input pulses and the optimally dispersion-compensated output pulses, measured using the original 62-fsec laser pulses as the reference, are shown in Figures 3.14 (a) and (b) respectively. The optimal length ratio R_{opt} is 4.63 (2060 m/445 m). This value is a little different from the short fiber link case (R_{opt}=4.57) because the center wavelengths are different (1558 nm vs. 1591 nm). The pulses initially broaden to ~400 ps (calculated) in 2060 meter of SMF(AT&T 5D) and are then recompressed to ~500 fsec FWHM using 445 meters of DCF (AT&T JRFDC1074C1DC) , resulting in a compression ratio of ~800. Note that because the path of the signal pulses (2.5 km of fiber) is much longer than that of the reference pulses (~2 m of free space), the #N output pulse is correlating with the #N+387 instead of the #N reference pulse. As in our previous 42-m experiments using shorter 62-fsec pulses, the output pulse shown in Figure 3.14 (b) displays an oscillatory behavior in the trailing edge, indicating some uncompensated third-order dispersion (or dispersion slope). The spectral interferometry technique used to measure the previous 42-m link cannot be applied here to this 2.5-km SMF-DCF link because the timing jitter of the pulse source washes out the interference of the #N and #N+387 pulses.

Nevertheless, a simple numurical simulation was performed to obtain a rough estimation of the residual third-order dispersion β_3 to be 0.026 ps^3/km. The darker line in Figure 3.15 indicates the numerical result of pulse propagation over a 2.5-km fiber with only third-order dispersion β_3 of 0.026 ps^3/km. Compared to the experimental result shown in the lighter line, the general match is good except a little discrepancy in the oscillatory behavior in the tail.

Compared to previous experiments using sub-500-fsec pulses and fiber gratings to compensate the dispersion of ~250-m of single-mode fiber [30], our experiments achieve an ~8x longer propagation distance over SMF. It is also interesting to compare to the TDM systems experiments of Kawanishi et al [1], in which 0.98 psec pulses were transmitted over 40 km with a broadening ratio of ~1.6. Those experiments employed a dispersion-slope compensating fiber to reduce the overall dispersion slope D' from 0.06 to ~0.02 $ps/km/nm^2$ (or β_3=0.033 ps^3/km). Our SMF-DCF link achieves a somewhat lower residual dispersion slope compensation and should therefore allow even a longer transmission distance if the same 0.98 psec pulses are applied.

We use this 2.5-km dispersion-compensated SMF-DCF link as the transmission link of our CDMA system experiments. To make up the losses in the link as well as in the coding devices, an Er-doped fiber amplifier (EDFA) (denoted as the pre-amplifier of our CDMA system) built by a collegue was installed directly after the filtered pulse source to boost the signal power level. Figure 3.16 [54] shows the schematic of this EDFA which is based on chirped pulse amplification [55] to reduce the nonlinear and saturation effects in the EDFA. The filtered pulses from the laser is first stretched by ~60 m of SMF followed by 18 m of Er fiber served as the gain medium. The amplified pulses are finally compressed by ~12 m of DCF. When pumped with ~24 mW of 980-nm beam the average signal power was increased from 50 μW to 1.2 mW, the power level we used in our CDMA system experiments. Due to the gain narrowing effects in the Er fiber the amplified pulses are broadened to ~350-500 fsec in duration depending on the pump level. Figure 3.17 (a) shows the intensity profile of an amplified pulse which has a pulsewidth of ~470 fsec and an average power of

$\sim$1.2 mw. Figure 3.17 (b) shows 650-fsec recompressed output pulses obtained after propagating over the 2.5-km dispersion-compensated fiber link. Due to narrower bandwidth of the amplified pulses, the output pulses are less broadened and exhibit a reduced oscillation in the pulse tail compared to the case of 250-fsec input pulses. As we will demonstrate in the next chapter, this oscillation due to residual third-order dispersion can be almost completely removed by a programmable pulse shaper which also serves as the encoder of the CDMA system.

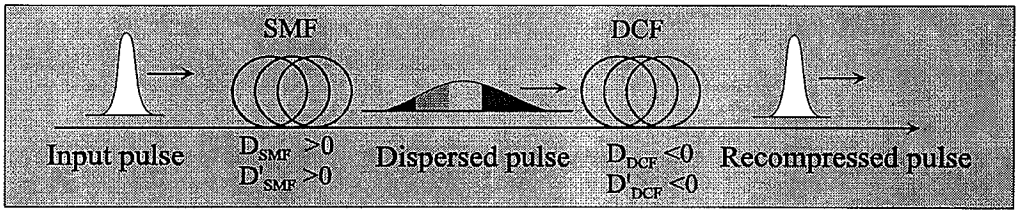

(a)

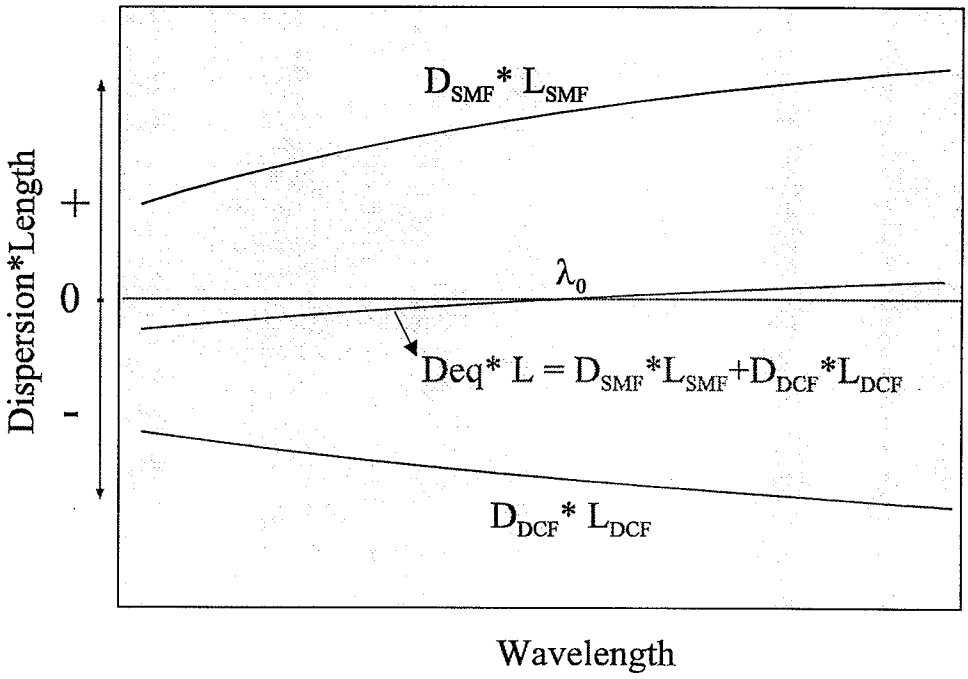

(b)

Fig. 3.1. Schematics of dispersion compensation using DCF. (a): schematic of a concatenated SMF-DCF link. (b): schematic dispersion curves of a SMF, a DCF, and a concatenated SMF-DCF link.

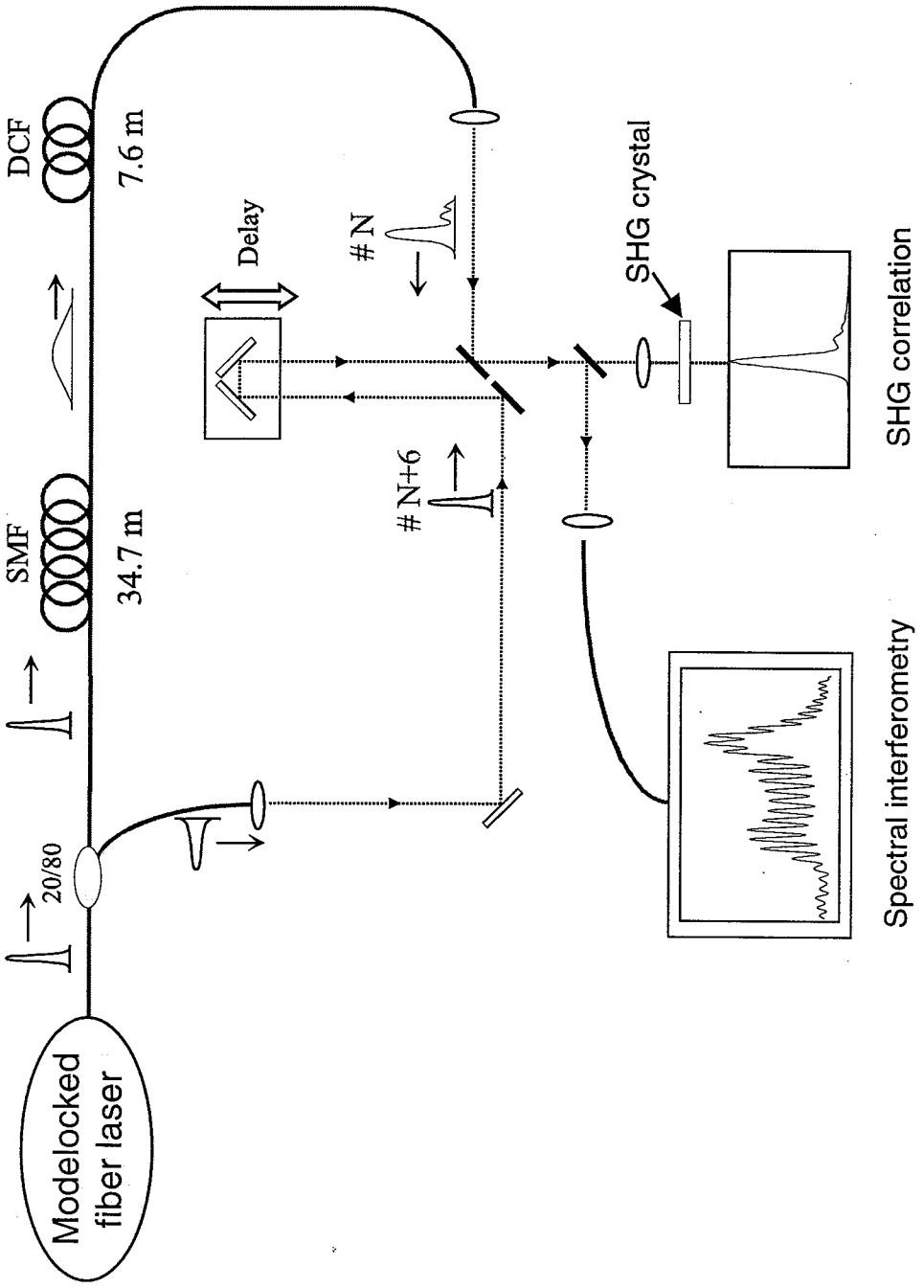

Fig. 3.2. The experimental layout for dispersion compensation experiments. 20/80: 20/80 fiber coupler; SMF: standard single-mode fiber; DCF: dispersion compensating fiber; SHG: second harmonic generation. The setup for SHG correlation measurements can be easily modified for spectral interferometry measurements by inserting a mirror in front of SHG crystal.

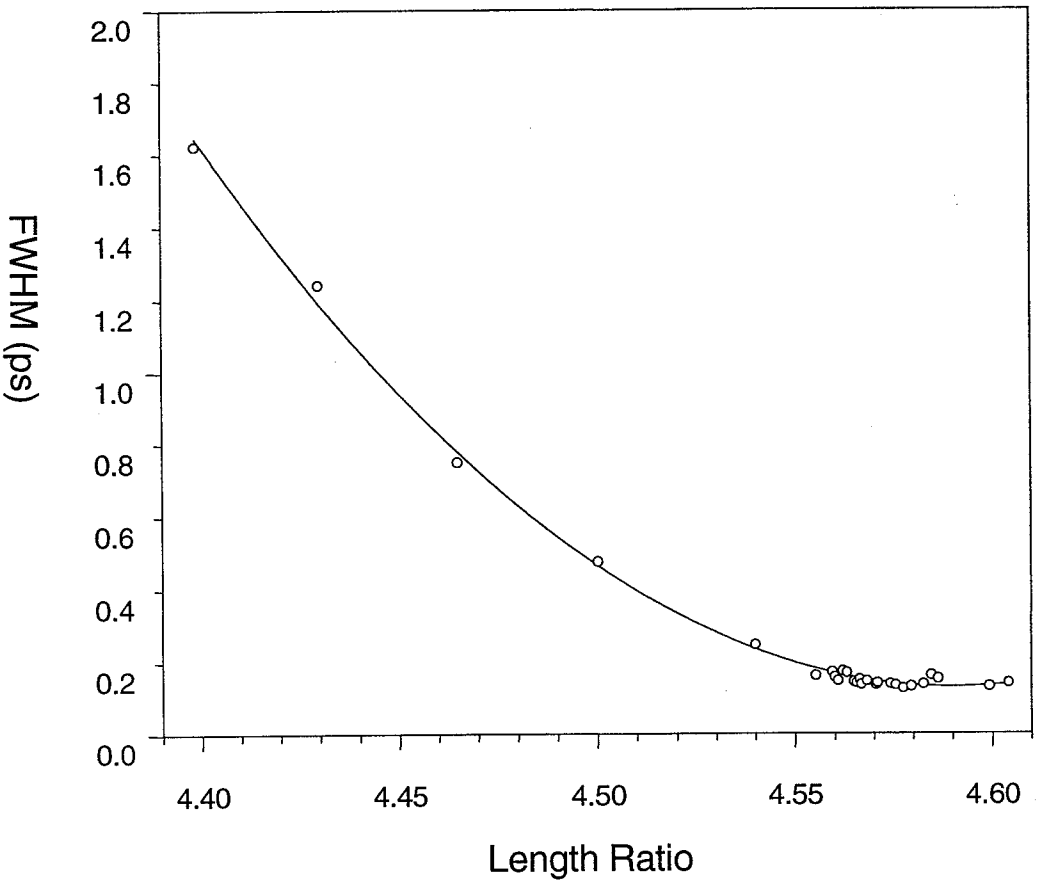

Fig. 3.3. Output pulse width as a function of the SMF-DCF length ratio

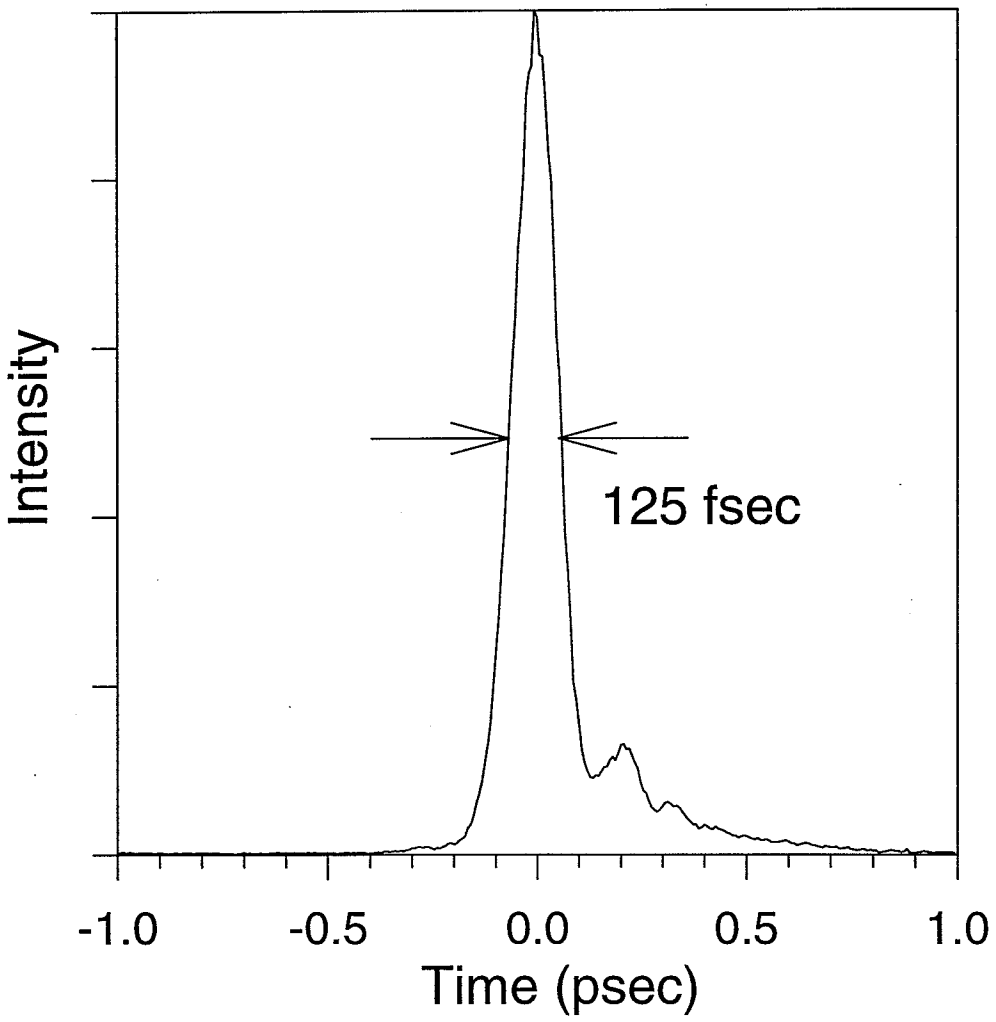

Fig. 3.4. Intensity profile of the output pulse from the optimally 42-m dispersion-compensated fiber link, measured by cross-correlation using a reference pulse directly from the laser. The 125-fsec cross-correlation width corresponds to a deconvolved pulsewidth of ~110 fsec.

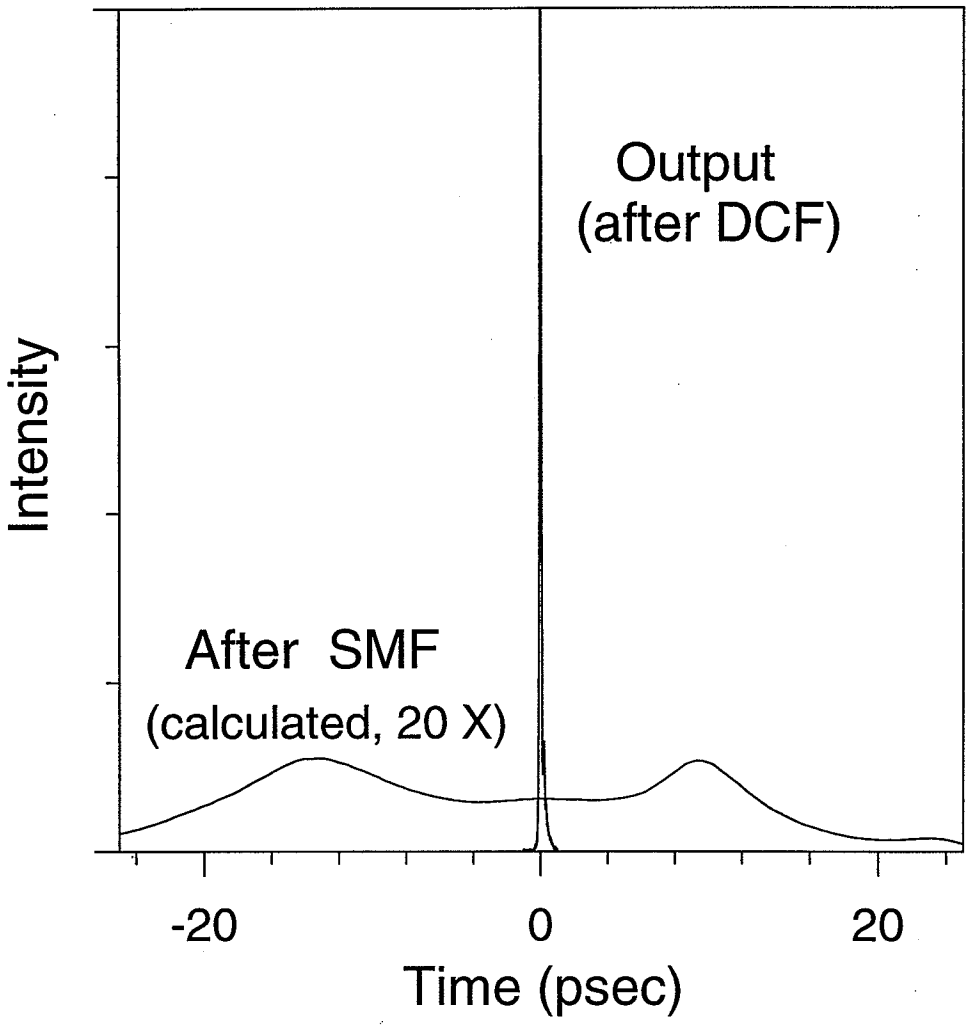

Fig. 3.5. The optimally dispersion-compensated pulse from Figure 3.4 is superimposed with the calculated pulse after propagation through SMF alone (magnified by 20 times). This shows a recompression ratio of 300.

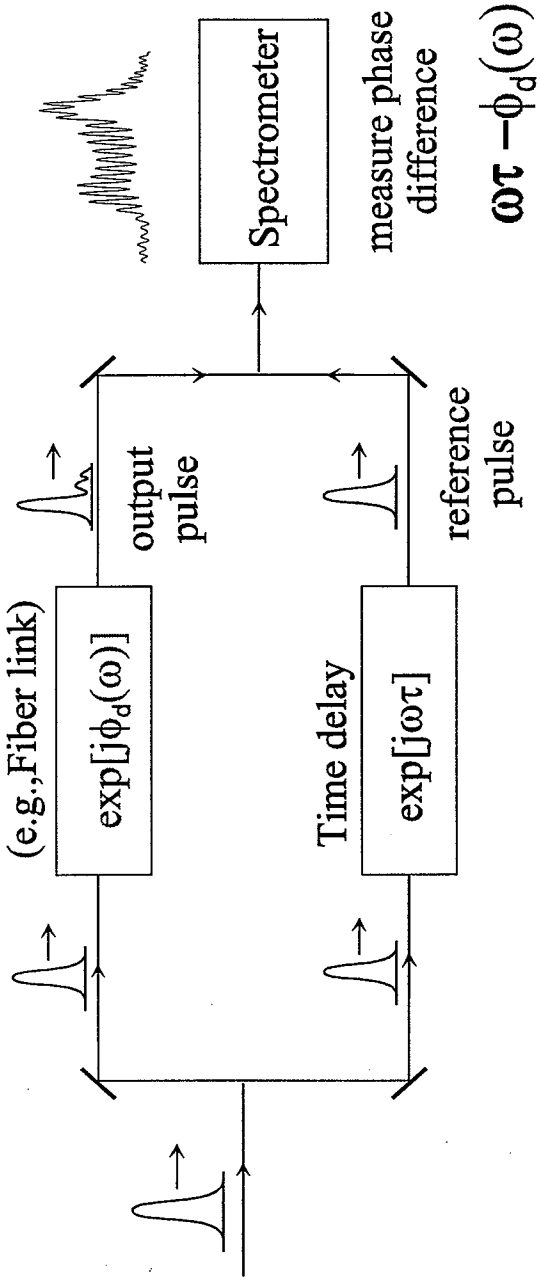

Fig. 3.6. Schematic of spectral interferometry. Pulses from a mode-locked erbium fiber laser are sent to a Mach-Zender interferometer. The coherent superposition of the distorted pulse and the time-delayed but undistorted pulse are recorded by an optical spectrum analyzer.

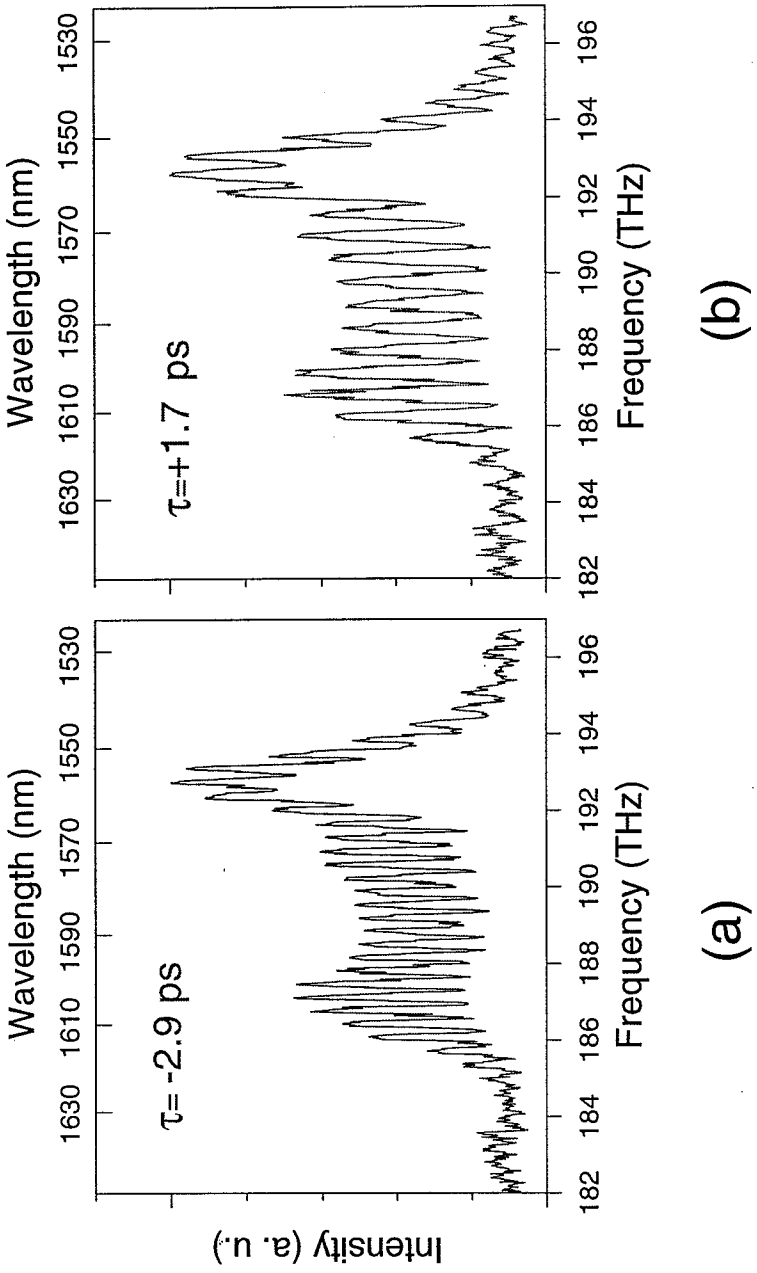

Fig. 3.7. Spectral interference patterns. (a) and (b) are the the interferograms recorded by the OSA corresponding to time delay of -2.9 ps (reference pulse ahead) and +1.7 ps, respectively.

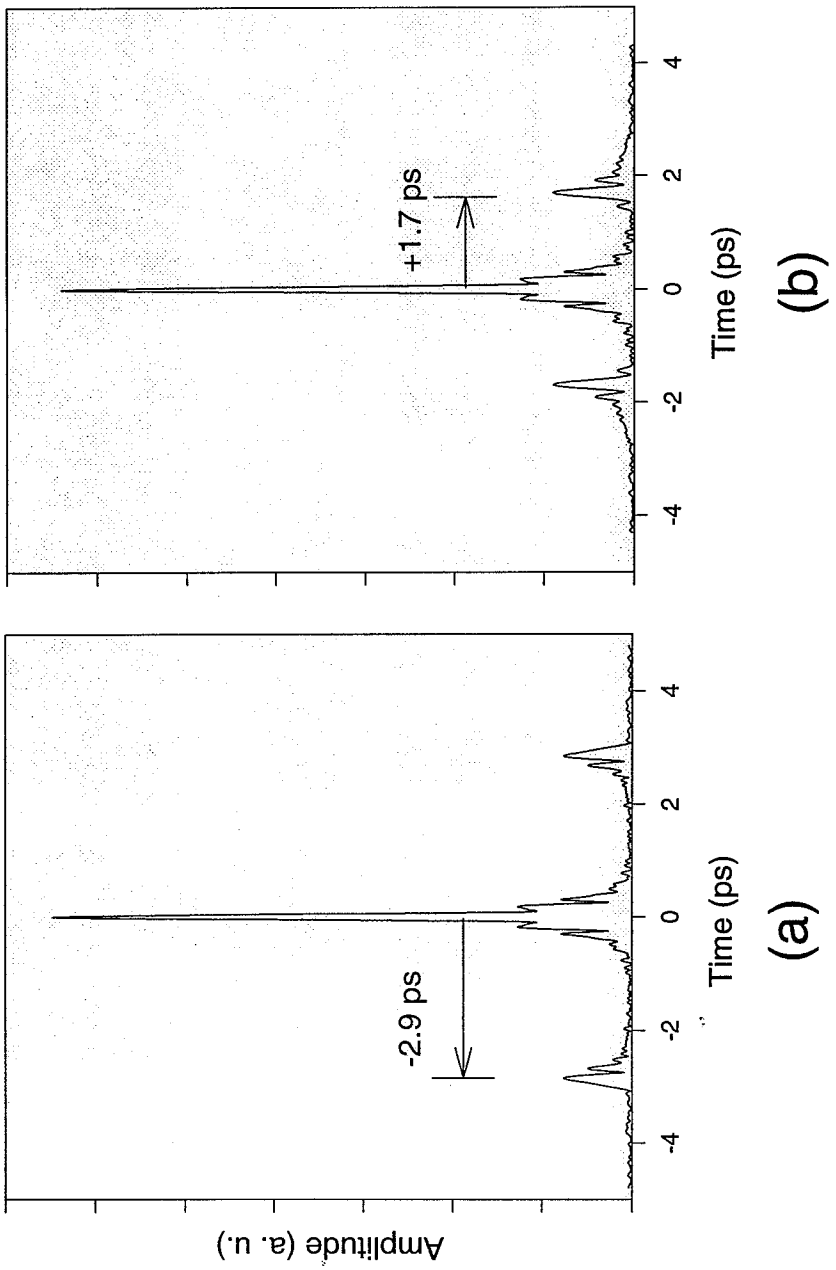

Fig. 3.8. (a) and (b) are the inverse Fourier transforms of the spectral interference patterns in Figure 3.7 (a) and (b), respectively.

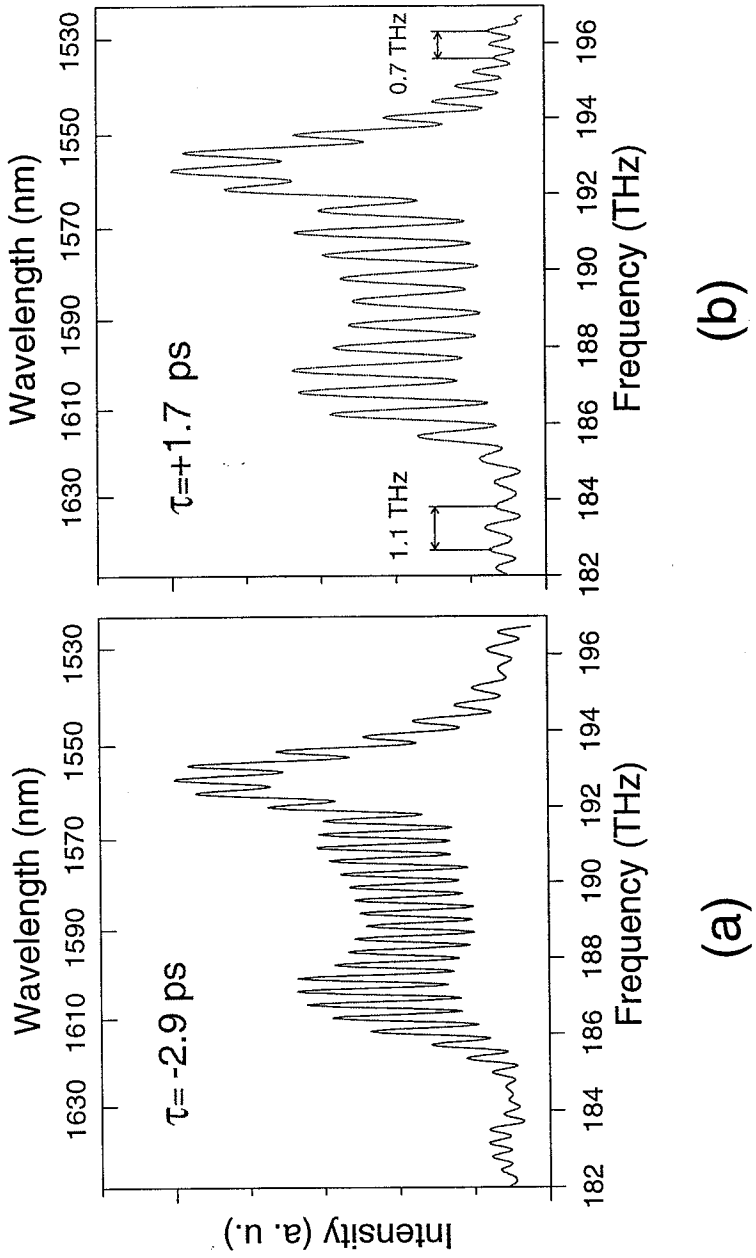

Fig. 3.9. Filtered spectral interference patterns. (a) and (b) correspond to the filtered version of the interferograms of Figure 3.7 (a) and (b), respectively. Small variations in the periodicity of the intensity peaks across the spectrum are caused by the residual dispersion of the 42-m fiber link.

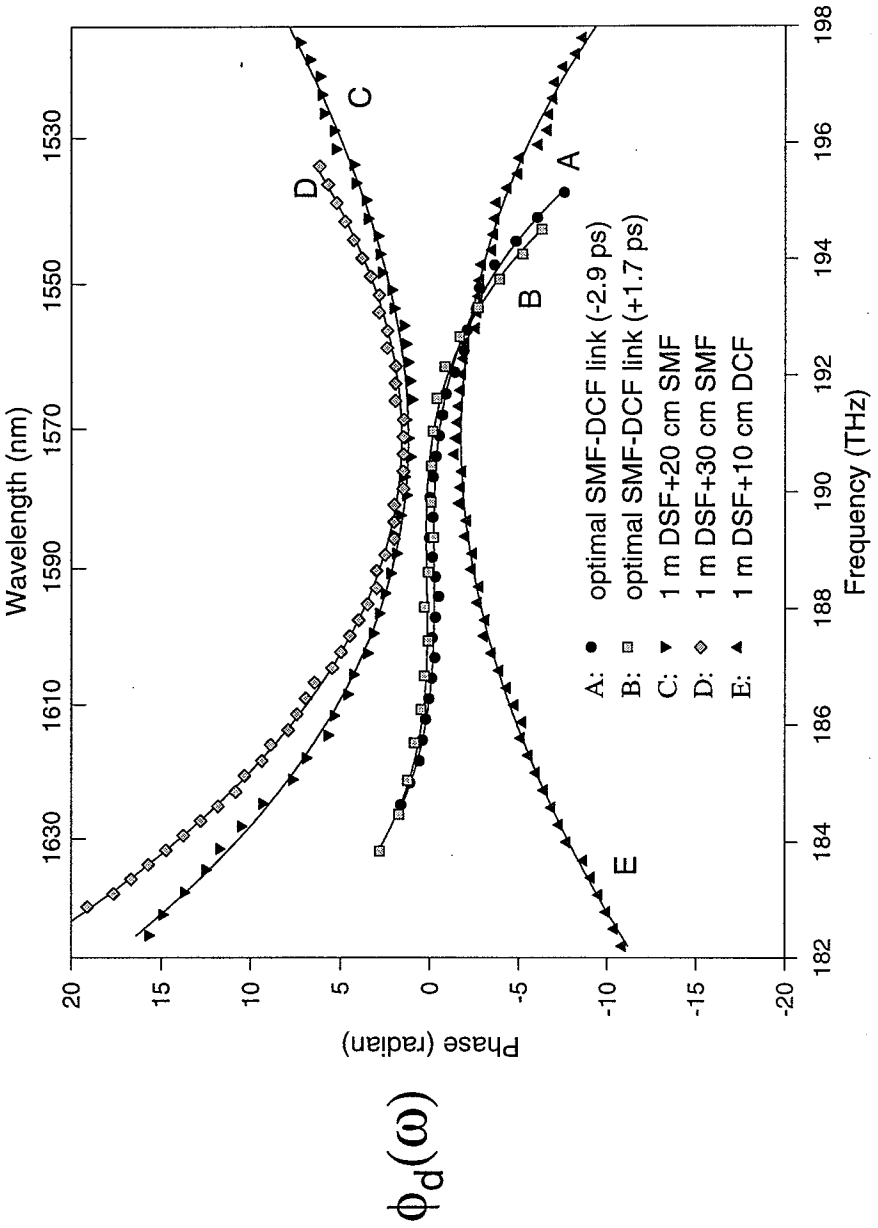

Fig. 3.10. Spectral phase shifts for interferograms. Curves A and B showing the phase distortion $\phi_d(\omega)$ of the optimally dispersion-compensated link are derived from the interferograms in Figures 3.9, respectively. Curves C, D, and E correspond to the phase distortion $\phi_d(\omega)$ of three fiber configurations respectively: 1-m DSF+ 20-cm SMF, 1-m DSF+ 30-cm SMF, and 1-m DSF+10-cm DCF.

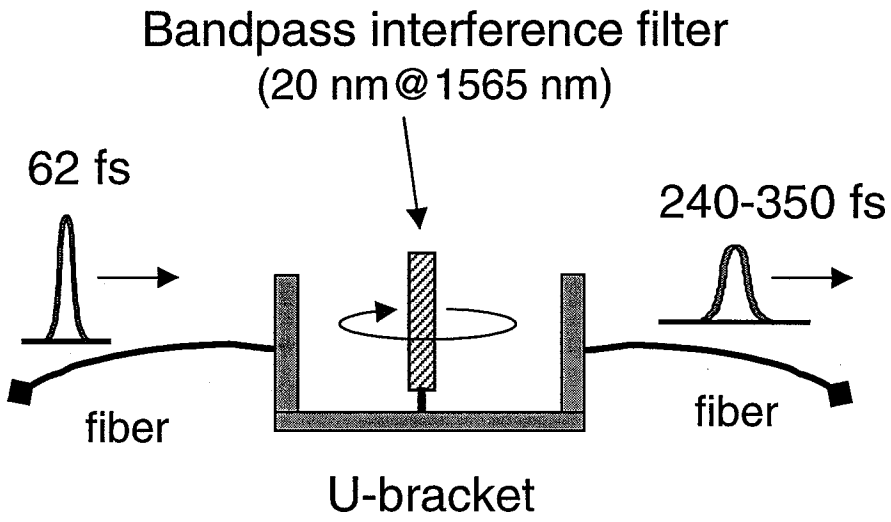

Fig. 3.11. Schematic of fiber-pigtailed bandpass interference filter. The center wavelength and bandwidth of the filtered spectrum can be tuned by rotating the interference filte.

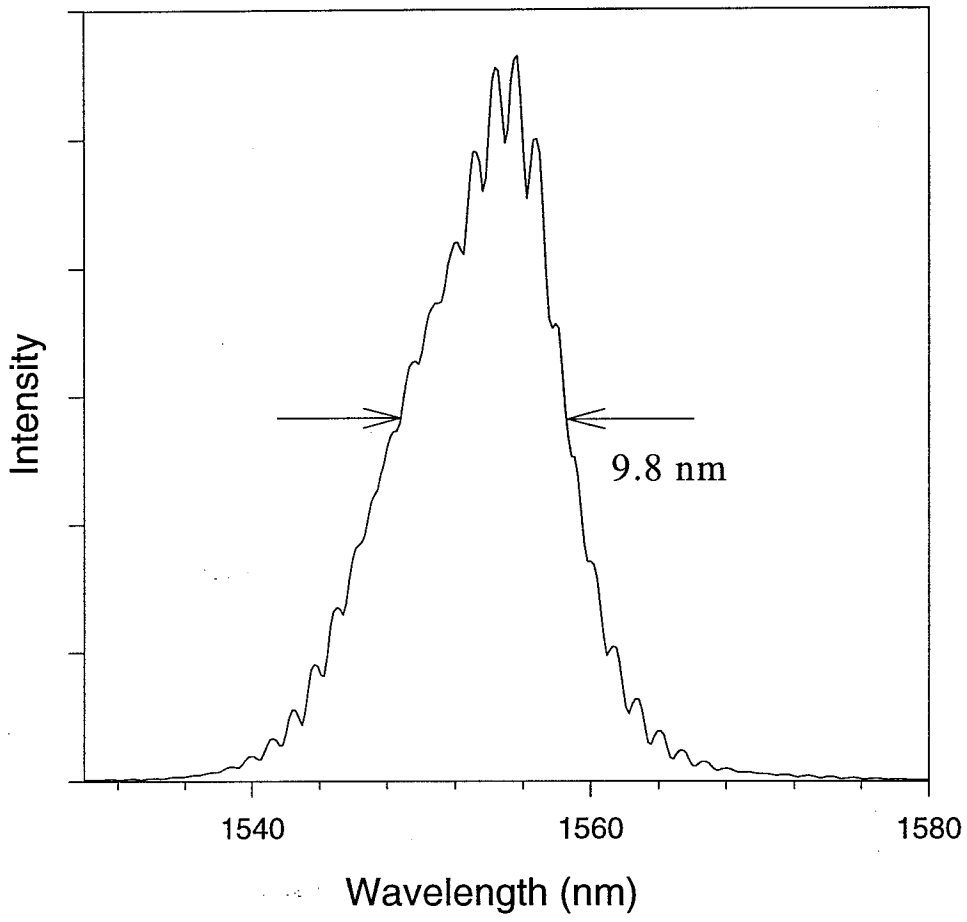

Fig. 3.12. Spectrum of the pulses after passing through the bandpass interference filter. The filtered spectrum corresponds to a bandwidth-limited pulsewidth of 230 fsec. The modulation in the spectrum is likely due to the Fabry-Perot effect of the interference filter.

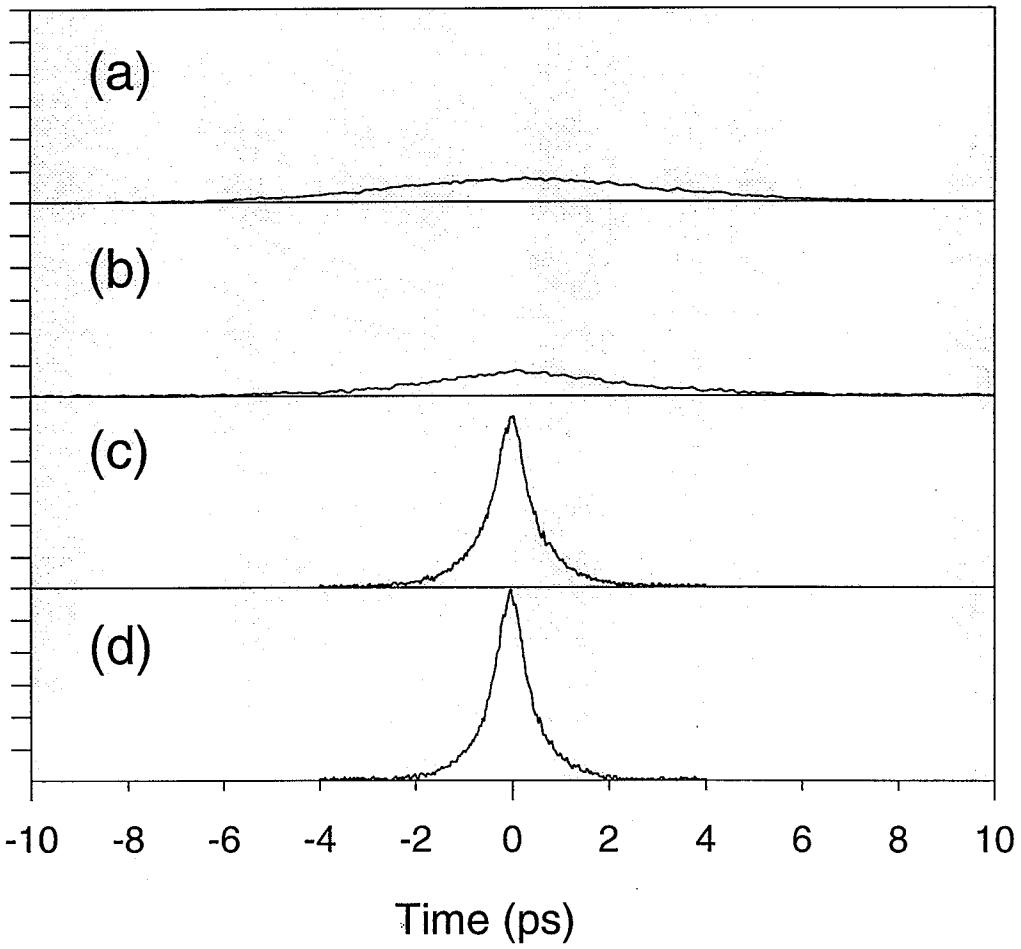

Fig. 3.13. Autocorrelation traces for output pulses from 2.5-km fiber link corresponding to different SMF/DCF length ratios (4.564, 4.575, 4.620, and 4.625 corresponding to (a), (b), (c), and (d), respectively) in the process of optimizing the link.

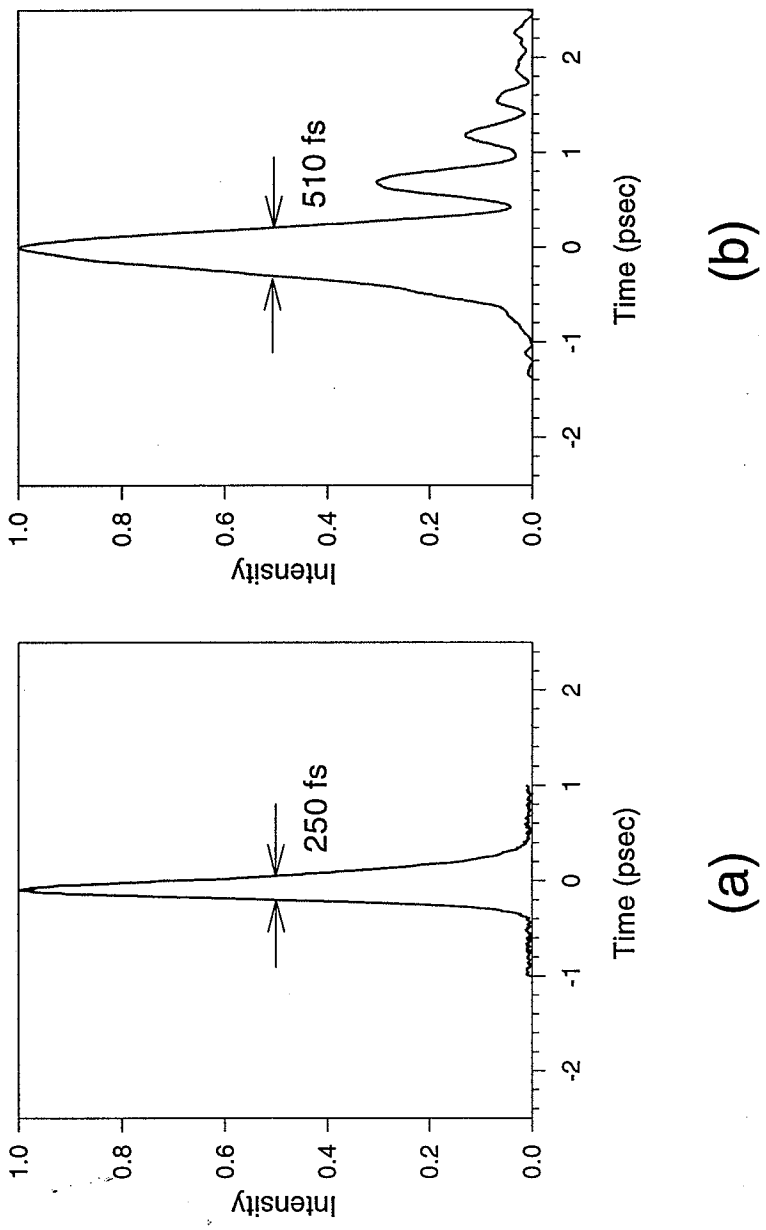

Fig. 3.14. 2.5-km fiber transmission for 245-fsec pulses. Intensity profiles of (a) the input 245-fsec pulse and (b) the output pulse of the 2.5-km optimally dispersion-compensated fiber link, measured by cross-correlations using a 62-fsec reference pulse directly from the laser. 255 fsec and 510 fsec correspond respectively to ~245 fsec and ~505 fsec in pulse duration after deconvolution.

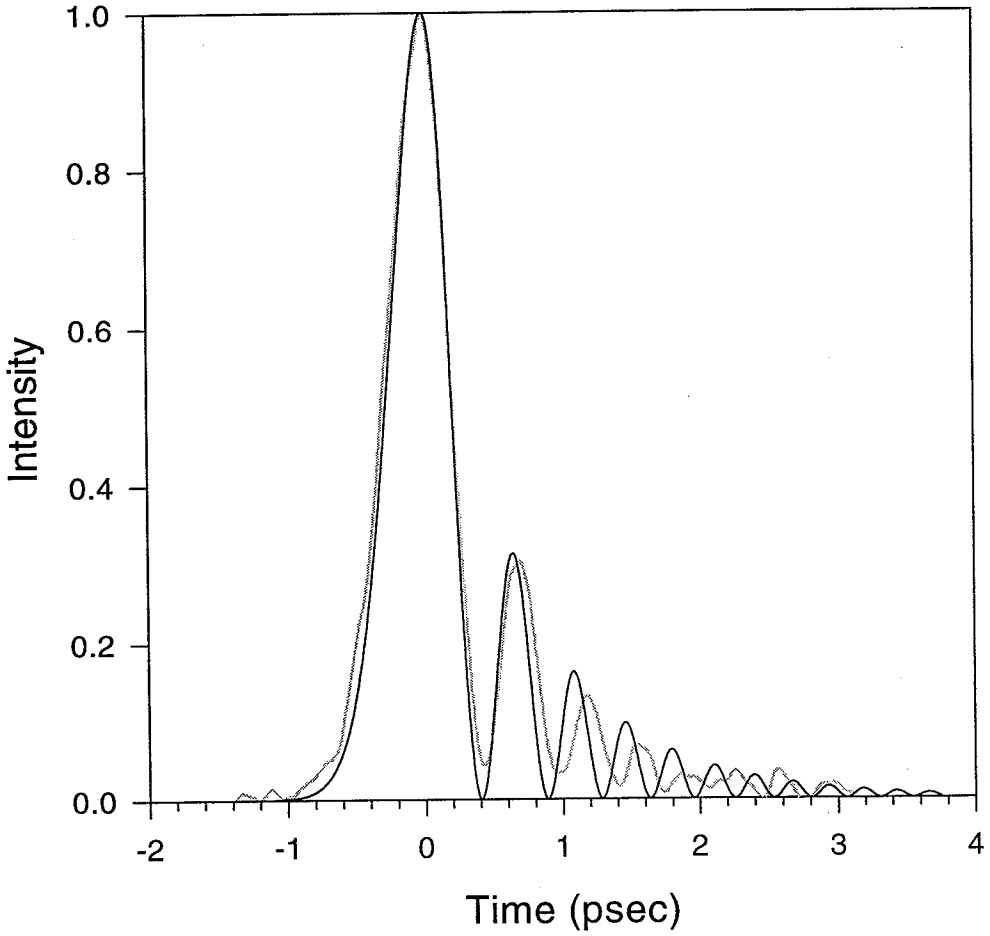

Fig. 3.15. Comparison of numerical and experimental results for 2.5-km pulse propagation. The darker line is the numerical simulation while the lighter line is the experimental result.

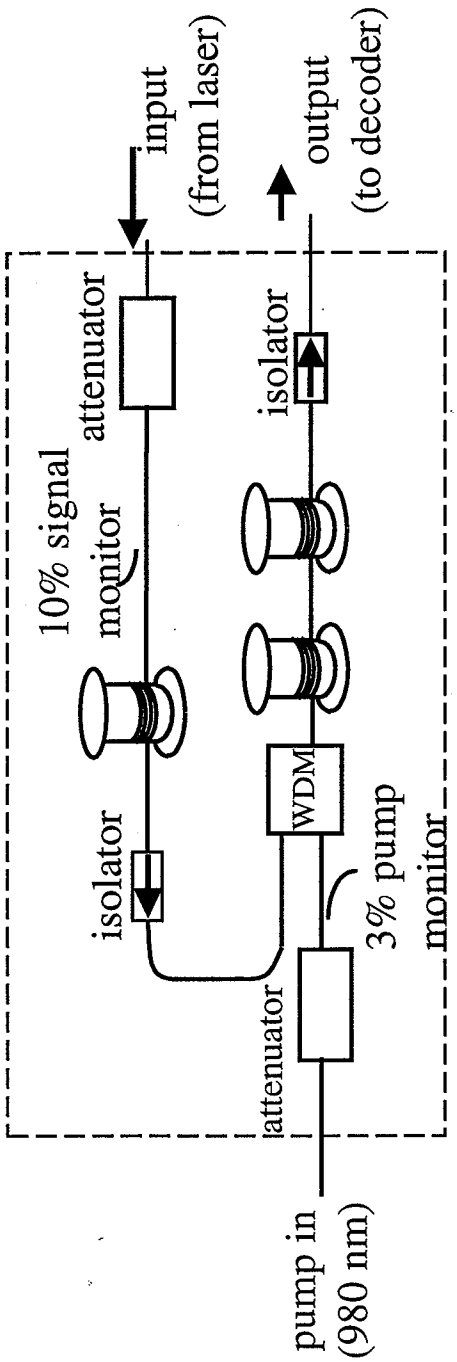

Fig. 3.16. Configuration of an all-fiber chirped-pulsed EDFA [54]

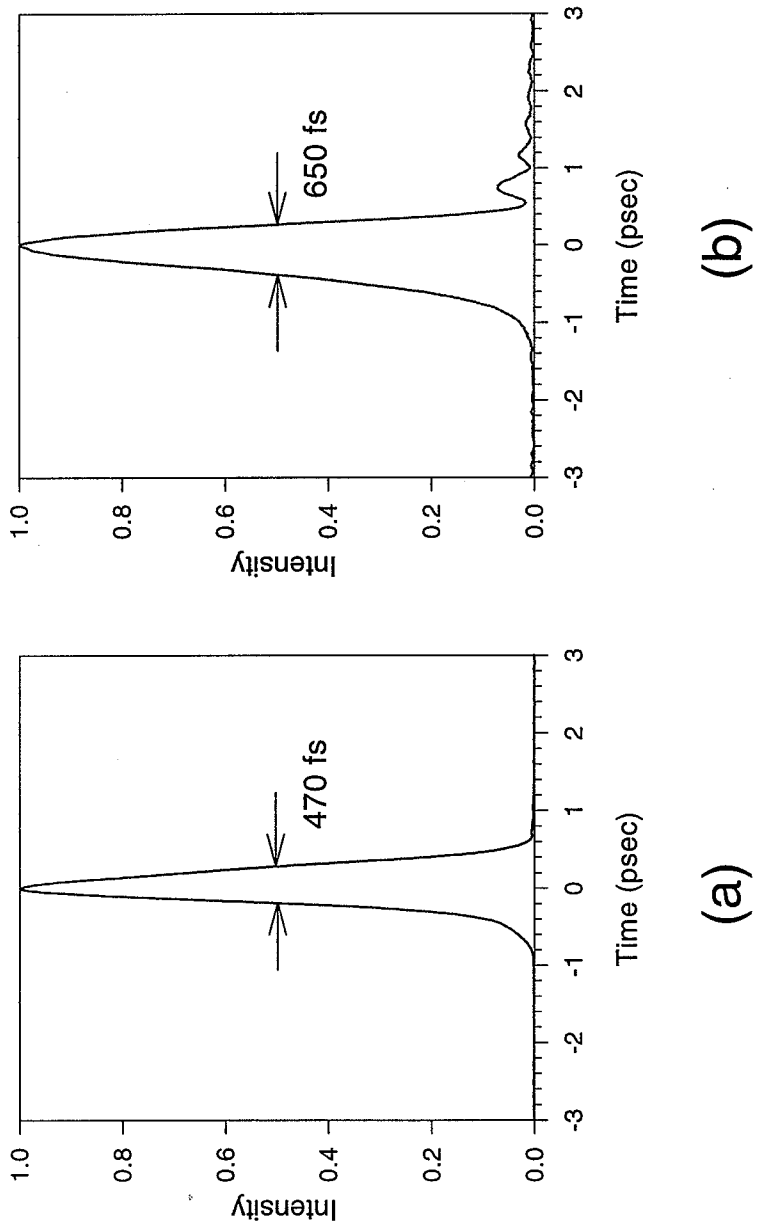

Fig. 3.17. 2.5-km fiber transmission for amplified 470-fsec pulses. Intensity profiles of (a) the input 470-fsec pulse and (b) the output pulse of 650 fsec FWHM from the 2.5-km optimally dispersion-compensated fiber link, measured by cross-correlations using a 62-fsec reference pulse directly from the laser.

4. FEMTOSECOND ENCODER AND DECODER: PROGRAMMABLE PULSE SHAPER

Ultrashort pulse code-division multiple-access (CDMA) communication network is based on spectral phase encoding and subsequent decoding of coherent ultrashort pulses [7]-[10]. Therefore, the success of femtosecond CDMA is crucially depending on the design of a competent individual phase encoder/decoder pair which can restore the intended encoded signals to original short pulses and keep the unwanted ones remain as low-intensity noise bursts. Grating-lens-lens pulse shapers based on Fourier transform technique have been shown capable of pulse shaping of high complexity through the spatial filtering of the various frequency components [56, 57] and are ideal candidates as our CDMA phase coders. Here, we employ a pair of programmable pulse shapers containing a programmable 128-element liquid crystal phase modulator array in the mask plane as our CDMA coding devices to provide spectral phase coding for optical pulses in the 1.5-μm wavelength band.

4.1 Fiber-pigtailed Programmable Pulse Shaper

Grating-and-lens pulse shapers was originally introduced by Froehly [58]. Such pulse shapers consisting of a pair of diffraction gratings, lenses, and a pulse shaping element can be arranged in a configuration which is capable of picosecond and femtosecond optical waveform synthesis through spectral filtering (by a spatial mask) in the mid-plane (called Fourier plane) and in the meantime introdues no temporal dispersion. The output pulse waveform is given by the Fourier transform of the pattern transferred by the mask onto the spectrum. Figure 4.1 shows the setup of our programmable pulse shaper. It is basically a conventional grating-and-lens pulse shaper with a programmable 128-element phase modulator array as the pulse shaping

element. In constructing this pulse shaper as our coding device, several parameters, such as grating period, lens focal length, input beam size and angle, have to be chosen with two considerations: the spectral resolution of the pulse shaper has to be small enough to resolve physical features as small as the pixel width (100 μm) of the phase modulator (more simplely, focused Gaussian beam radius w_0 has to be smaller than pixel width [60]) and the spatial dispersion α of the pulse shaper spreads the coded bandwidth (~15 nm) over within the phase modulator width (12.8 mm). In terms of equations, they can be expressed as

$$w_0 = \frac{cos(\theta_{in})}{cos(\theta_d)} \left(\frac{F\lambda}{\pi w_{in}} \right) < 100\ \mu m \tag{4.1}$$

$$\alpha = \frac{\Delta x}{\Delta \lambda} = \frac{F}{d\, cos(\theta_d)} < \frac{12.8\ mm}{15\ nm} = 0.85\ mm/nm, \tag{4.2}$$

where θ_{in} is input beam angle, θ_d is the diffracted angle, F is the lens focal length, w_{in} is the input beam radius, and d is the grating period. Furthermore, θ_{in} and θ_d have to satisfy grating equation given as

$$sin(\theta_d) = \frac{\lambda}{d} - sin(\theta_{in}). \tag{4.3}$$

For our pulse shapers, we use d=1100 lines/mm, F=190 mm. Although w_o and α can be calculated from the above equations once w_{in}, θ_{in} and θ_d are measured, they can also be estimated by matching numerical simulation results with experimental results as we will describe in the next section.

As shown in Figure 4.1 the various frequency components of the pulses are spatially dispersed across the Fourier plane by the first grating and lens and recombined by the second identical grating and lens. In the Fourier plane a programmable liquid crystal modulator array (LCM) is placed to spectrally manipulate the pulses. A pair of zero-order half-wave plates are placed before and after the LCM to rotate the polarization from horizontal to vertical and vice versa because while the gratings require horizontal polarization for good diffraction efficiency, the LCM was designed for vertical polarized beam. In general, the output pulse emerging from the shaper is the Fourier transform of the pattern transferred by the mask phase function provided

by LCM onto the spectrum of the input pulse. The main modification of our pulse shaper over a conventional pulse shaper [57] is that the input and the output ports are fiber pigtails (~1.5 m SMF each end) with connectors. A pair of achromatic lenses (F=40 mm) are inserted in front of the bare fiber end of the input and output fiber for collimating and coupling respectively. The major advantage of fiber-connectorized ports is the flexibility and ease of hooking up any optical fiber devices without any beam alignment. The down sides are the fiber pigtails scramble polarization and introduce a small amount of dispersion. Therefore, a pair of polarization controllers are placed at each end to adjust the polarization state for best power throughput. To compensate the dispersion of the fiber pigtails the position of the second grating is adjusted so that the pulse shaper is in the minimum dispersion configuration such that when 0 phase (or any arbitrary constant phase) is applied to all pixels of the LCM, the pulses are at their shortest possible width right at the output fiber end of the pulse shaper. Figure 4.2 shows the autocorrelations of the input (a) and output pulses (b) when the pulse shaper is in least-dispersion configuration. The small broadening of output pulses compared to the input pulses may be due to a somewhat narrower output spectum, as shown in Figure 4.3. The narrowing of spectrum can be attributed to some polarization effects which reduce the diffraction efficiency from the gratings for the spectral components in the wings of the the spectrum . With careful design and alignments, our fiber-pigtailed femtosecond pulse shaper with a liquid crystal phase modulator (LCM) in place achieves a very low insertion loss (5.3 dB fiber-to-fiber) and a high-fidelity pulse transmission when no pulse shaping is applied.

4.1.1 Liquid Crystal Modulator Array

Femtosecond pulse shaping of high complexity using a programmable home-made 128-element liquid crystal phase modulator has been demonstrated [57]. Here we use a similar but improved, commercially available (supplied by Cambridge Research and Instrumentation) liquid crystal phase modulator array. The array contains 128 phase-modulating pixels on 100 μm centers with ~3 μm interpixel gaps.

Each pixel is connected to its own corresponding electrical connection. A computer-controllable drive circuit can generate 128 separate, variable amplitude signals to achieve independent gray-scale phase modulation for all 128 elements in the way described as follows. When no field is applied, the liquid crystal molecules are aligned with their long axes along the vertical direction and therefore have no effect on the incoming vertically polarized light. However, when an applied electric field changes the orientation of the molecules, the refractive index changes for the vertically polarized light. The amount of phase change induced in an individual pixel depends on the index change which is increased with the applied drive voltage level. Since the beam is spatially dispersed across the LCM, different wavelength components hit on different pixels. Drive voltage between 0 to 10 volts is divided into 4000 levels to provide an almost continuous gray-scale phase modulation of 0 to 3.5 π radians for each pixel. This feature enable the programmable pulse shaper not only to encode femtosecond pulses with some pseudorandom binary phase codes but also in the mean time provide arbitrary phase correction functions to compensate the residual dispersion of the fiber link. Figure 4.4 shows the schematic of LCM with several different applied phase functions: length-63 maximal length binary sequence (M-sequence) (a), cubic phase variation (b), quadratic phase variation (c), and length-63 M-sequence combined with quadratic phase function (d). We will demonstrate in the next section the use of this programmable pulse shaper to further remove the residual dispersion of the 2.5-km SMF-DCF link.

4.2 Dispersion Compensation Using Programmable Pulse Shaper

As shown in Figure 4.5, a programmable pulse shaper is inserted before the 2.5-km transmission fiber link to provide fine tuning of the phase correction and also serves as a CDMA encoder in later system experiments. When no phase or constant phase is applied to the LCM, the pulse coming out of the pulse shaper with a duration of ~480 fsec FWHM , as shown in Figure 4.6 (a), serves as the input pulse to the 2.5-km SMF-DCF link described in Chapter 3. The pulses would broaden to ~200 ps

after propagating over 2060 m of SMF and the subsequent 445-m DCF compensates most of the dispersion in SMF and recompresses the pulses to ~580 fsec, as shown in the cross-correlation trace in Figure 4.6 (b). The output pulses again shows small oscillation in the tail indicating small residual positive third-order dispersion, as we have observed in the previous chapter.

To further compensate this residual dispersion slope we applied a cubic phase variation across the LCM. Using our earlier estimation of dispersion slope of SMF-DCF link as a starting point, we iteratively adjust the amount of cubic phase applied to LCM to completely remove the oscillation in the pulse tail. Figure 4.6 (c) shows the cross-correlation of the output pulse from the 2.5-km link when an optimal positive cubic phase [shown in Figure 4.6 (d)] was applied. The quadratic and cubic phases provided by pixel #N of the LCM can be formulated as

$$\Phi_n = \frac{\phi_2}{2}(n-64)^2\ \delta\omega^2 + \frac{\phi_3}{6}(n-64)^3\ \delta\omega^3, \tag{4.4}$$

where n=1,2,3,....,128, ϕ_2 (in ps^2) and ϕ_3 (in ps^2) are the second- and third-order phase dispersion respectively, and $\delta\omega$ is the angular frequency increment (which is 1.1×10^{11} rad/sec in our case) between adjacent pixels. Note that the pixels are numbered in such way that higher frequency components impinge on higher number pixels. The phase variation is discretely sampled over the entire 128 pixels but since the phase difference between the first and the last pixel is quite small ($\sim2.1\pi$), it can be basically considered as continuous sampling. Therefore exact phase correction is feasible as we can see in Figure 4.6 (c) so that the small cubic phase is compensated and the pulse (of ~490 sec) is almost restored to the input pulsewidth. The optimal applied cubic phase in Figure 4.6 (d) corresponds to a third-order dispersion ϕ_3 of 0.06 ps^3. Since the phase accumulated in passing through fiber of length L can be expressed as

$$\Phi_F(\omega) = -\frac{\beta_2}{2}(\omega-\omega_0)^2\ L - \frac{\beta_3}{6}(\omega-\omega_0)^3\ L + ..., \tag{4.5}$$

the residual third-order dispersion coefficient β_3 of the 2.5-km dispersion-compensated SMF-DCF link is $+0.024(\pm0.006)$ ps^3/km. This number is 4 or 5 times lower than

that of dispersion-shifted fiber (DSF) and roughly consistent with our earlier measurement of a 42-m fiber link (+0.018 ps^3/km) using spectral interferometry described in Chapter 3. Note that though phase curve in Figure 4.6 ranges from ~-1.1π to ~1.0π, in reality the phase applied to each pixel is between π to 3π modulo 2π.

To demonstrate the ability to program the magnitude and the sign of the cubic phase term, in Figures 4.7 (a) and (b) we show the intensity profiles of the output pulses from the 2.5-km fiber link when cubic phase variations ϕ_3 of -0.25 ps^3 and +0.25 ps^3 are applied to the LCM respectively. The larger applied cubic phases clearly result in more pronounced oscillating tails in the time domain data. By choosing the sign of the cubic phase we can select the oscillatory tail either before or after the main pulse. Note that the oscillation in Figure 4.7 (a) is more pronounced than (b) because the total amount of cubic phase in case (A) (-0.31 ps^3, including the SMF-DCF link) is larger than the case (b) (+0.19 ps^3, including the SMF-DCF link).

Although the demonstrated dispersion-free transmission length of 2.5 km here is already suitable for local-area-networking CDMA applications, we have not reached the phase modulation capacity of the LCM. To test our LCM for higher cubic phase compensation, we added a 500-m DSF which has zero dispersion wavelength (1559 nm) close to the center wavelength (~1558 nm) of our pulses. Figures 4.8 (a), and (b) respectively show the intensity cross-correlations of the input pulses (FWHM~490 fsec) and the output pulses (FWHM~770 fsec) of the 3-km SMF-DCF-DSF link when no phase correction is applied to the LCM. As demonstrated in Figure 4.8 (b), the added 500-m DSF transmission results in more negative cubic phase variation (ϕ_3) indicated by the more pronounced tail as well as some quadratic phase which partially washes out the oscillation in the tail. By applying a cubic phase compensation ϕ_3 of 0.125 ps^3 and a small quadratic phase correction ϕ_2 of 0.05 ps^2 [Figure 4.8 (d)], we have been able to compress the pulses to 500 fsec, almost the original pulsewidth, as shown in Figure 4.8 (c). From the cubic phase curves in Figure 4.6 (d) and Figure 4.8 (d), the cubic phase contributed by the 500-m DSF is easily calculated to be ϕ_3=-$\beta_3 L$=-0.065 ps^3. Therefore the β_3 of the DSF is 0.13 ps^3/km which is 5.4

times higher than the equivalent β_3 (=0.024 ps^3/km) of the dispersion-compensated SMF-DCF link.

We briefly discuss the maximum dispersion compensation capacity of our setup. There are two major factors limiting the capacity of a pulse shaper. One is the discrete sampling of continuous phase functions due to the finite pixel width. The other is the finite spectral resolution due to the finite focused spot size on the Fourier plane. When the pulse shaper has sufficient spectral resolution, the dispersion is limited by the requirement that the time delays due to the phase variation have to be smaller than the pulse shaping time window which is inversely proportional to δf, the frequency increment per pixel. This can be expressed as [57]

$$\frac{\delta\phi}{\delta\omega} \leq \frac{1}{2\delta f} \quad \text{or} \quad \delta\phi \leq \pi\,. \tag{4.6}$$

That is, the maximum phase shift from one modulator pixel to the next remain less than π, so that the discrete array adequately samples the desired phase function. For the cubic spectral phase, the maximum phase jump occurs between last (#N) and the last second (#N-1) pixels. Combining Equation 4.4 and Equation 4.6 results in

$$|\phi_3| \leq \frac{8\pi}{N^2\delta\omega^3}, \tag{4.7}$$

where N is the number of pixels in the array. For our parameters, $|\phi_3|$ <1.15 ps^3. When the individual frequency components are focused to spots larger than individual pixels, this reduces the spectral resolution and restricts the available time window for pulse shaping. Because of the finite focus beam spot and thus finite spectral resolution, the effective filter tranfer function of the pulse shaper is no longer just a scaled version of the applied phase mask but modified to be [59, 60]

$$H(\omega) = \left(\frac{2}{\pi {w_0}^2}\right)^{1/2} \int M(x) e^{-2(x-\alpha\omega)^2/{w_0}^2}\, dx, \tag{4.8}$$

where w_0 is the focused Gaussian beam radius, M(x) is the applied phase function (e.g., an M-sequence code), and α the spatial disperstion. Basically, physical features on the mask plane smaller than w_0 can not be resolved [59, 60]. To determine the

value w_0 and α, we simulate encoded output power spectra using Equation 4.8 in which w_0 and α are adjusted to match the experimental results. Figure 4.9 shows the experimental encoded power spectra (recoded by an optical spectrum analyzer) and Figure 4.10 shows the matching numerical simulation results using appropriate w_0 and α. As a result, w_0 and α are estimated to be $\sim$130 μm (which is larger than the pixel width 100 μm) and 0.75 mm/nm, respectively. Fairly good match between these two figures validates the physical parameters we use in our simulation. The spectral resolution, wich is given as $\delta f \sim (\ln 2)^{1/2} w_0/\alpha$, of the current pulse shaper setup is $\sim$0.02 THz (0.16 nm), corresponding to $\sim$1.3 pixels. This results in a time window for pulse shaping $|t|<11$ ps, which implies $|\phi_3|<0.45$ ps^3. The spectral resolution, time window, and maximum cubic phase can be adjusted through choice of the pulse shaper and incoming pulse parameters.

Note that there are spectral notches (or holes) in the encoded power spectra (Figure 4.9) which appear in the $0 \leftrightarrow \pi$ transition points and give rise to energy loss at the output fiber end. Although the occurance of these spectral notches can be simulated by using the tranfer function in Equation 4.8 which takes into account of finite focused beam size, the physical explaination can be given as follows. As illustrated in Figure 4.13, for some wavelength components focused near the $0 \leftrightarrow \pi$ transition points, due to the finite focused beam spot part of the wavelength part of the beam hits on 0-phase pixel while the remaining part hits on π-phase pixel. When collected and focused into the output fiber core, the two parts (positive and negative) of the same wavelength components experience destructive interference and therefore the spectral intensity corresponding to those wavelength components are reduced. For these wavelength components, the most part of the energy goes to the constructive interferece point which is outside of the fiber core and can not be captured. Longer codes have more $0 \leftrightarrow \pi$ transitions therefore they produce more spectral notches and thus lower output power.

To summarize for this section, using the technique of a fixed fiber method for coarse dispersion compensation together with the LCM apparatus for fine tuning of

the residual dispersion, we demonstrate nearly dispersion-free 2.5-km fiber transmission for sub-500-fsec pulses. The distortionless transmission distance can be extended to >15 km if the LCM is exploited to its current capacity which is limited by the spectral resolution of the pulse shaper. In contrast to other schemes [33, 34, 61] for dispersion-slope compensation, our programmable pulse shaper approach can easily provide tunable fine-tuning of cubic phase alone (as well as potentially higher order terms) without needing any mechanical adjustment.

4.3 Phase Encoding and Decoding of Femtosecond Pulses

Although successful encoding and decoding of femtosecond pulses has been previously demonstrated, it was operated at visible wavelengths and encoding/decoding was performed by using a pair of conjugate phase masks adjacent to each other in the same grating-and-lens pulse shaper [7, 8]. In our CDMA system, encoding and decoding have to be carried out in two separate pulse shapers connected by 2.5-km transmission fiber link. Therefore, for successful decoding the two pulse shapers have to be carefully lay out adjusted to have an identical configuration and an excellent alignment in the Fourier plane. In this section we will investigate the encoding and decoding performance of our coding pair by connecting them back to back excluding the dispersion effect of the transmission fiber link.

4.3.1 Coding scheme: M-sequence

The phase coding scheme we use for our CDMA project is the M-sequence [62] pseudorandom binary phase ("0" or "π") codes which have been widely used in the spread-spectrum communication. The code length L_M of the M-sequence is of the form 2^N-1 (e.g., L_M=15,31,63,127...). Two properties of M-sequence are of great importance to spread spectrum communication whose addressing scheme is based on matched filter operation. The first property is that any shifted version of a M-sequence code results in another M-sequence code which is "orthogonal" to the original code. By orthogonal we mean that the two codes have the smallest correlation value of

1 or -1. The second property is the sum of two orthogonal codes result in another code which is orthogonal to the original two codes. M-sequence of length L_M has L_M different orthogonal codes.

Since our LCM has 128 pixels, the maximum code length of M-sequence we can apply is 127. However, because the spectral resolution of the pulse shaper can not resolve physical features smaller than ~1.3 pixels, for our CDMA experiments we primarily employ length-31 (4 pixels per code element) and length-63 (2 pixels per code element) M-sequence codes to investigate the encoding/decoding performances of our CDMA system. When an M-sequence binary ("0" or "π") phase code is applied to the LCM, the short pulses entering the pulse shaper are encoded into relatively wide (>10 ps) pseudonoise bursts with reduced peak intensity. Figure 4.11 and Figure 4.12 show the encoded output pulse data [intensity profile (a) and power spectrum (b)] when a length-31 and a length-63 M-sequence are applied, respectively. As shown in the part (a) of these two figure, the spread in time increases with code length.

4.3.2 Alignment of the Encoder and the Decoder

To decode the encoded signals back femtosecond pulses, a complementary (or phase-conjugate) binary phase pattern (0 or π) has to be applied to the same wavelength components in the decoder. Therefore, the decoder pulse shaper has to be made identical to the encoder so that both have the same spectrum-to-space correspondence in the LCM plane. This means that the same frequency components have to pass through corresponding pixels of the encoder and decoder LCMs so when a pair of phase-conjugate codes are applied all the output wavelength components experience the same overall phase shift, as illustrated in the Figure 4.14 (a). If there is some misalignment between the two pulse shapers, the total phase shift will not be the same for all wavelengths even phase-conjugate code sequences are used, as demonstrated in Figure 4.14 (b). To achieve the same spectrum-to-space correspondence, all the components, such as fiber pigtails, gratings, lenses, and LCMs, used in both pulse shapers are identical and they were carefully and iteratively adjusted

to yield exactly the same configuration. To check if the two pulse shapers are well aligned in the spectrum-to-space correspondence, we applied 0 phase to all pixels on both LCMs except three pixels, #10, #64, and #110, being applied with phase of π and compared the output power spectra from the two pulse shapers when the same input pulses were used. As we can see from Figure 4.15, the two output power spectra are almost identical with the three notches ($0 \leftrightarrow \pi$ transitions) occurring at the same wavelength points. This indicates very good alignment between the encoder and decoder, a prerequisite for successful decoding.

4.3.3 Decoding of Encoded Signals

Before we integrate the encoder/decoder pair into the CDMA system in which the encoder and decoder are connected by transmission fiber link, we evaluate their performance alone by connecting the two pulse shapers back to back. The coded signals exiting the encoder were immediately sent to the decoder. If no phase or a constant phase are applied to both LCMs, there is no coding involved and the output pulses (denoted as "uncoded pulses") from the encoder is almost the same as the input pulses only with reduced intensity. If a pair of phase conjugate M-sequence codes are applied respectively to the encoder and decoder LCM, the noise-like coded waveforms after the encoder are restored to short pulses (denoted as "properly decoded pulses") by the conjugate code in the decoder. If the M-sequence phase code applied to the decoder LCM is non-conjugate (or orthogonal) to the encoding M-sequence, the output signals from the decoder remain as low-intensity wide-spread noisebursts (denoted as "improperly decoded pulses"). Figure 4.16 and Figure 4.17 show the intensity cross-correlations for the uncoded (a), properly decoded (b), and improperly decoded pulses (c) and their corresponding power spectra (d), (e), and (f) for length-31 and length-63 M-sequence codes, respectively. As shown in these two figures, the properly decoded pulses are very well restored to the uncoded pulses except for some tiny sidelobes and the reduced intensity due to the higher insertion loss associated with M-sequence codes. High contrasts in peak intensity (8.5 dB for

-31 and 9.0 dB for length-63 M-sequence) and duration between properly and improperly decoded pulses are demonstrated in these two figures. Notches appear ... in the power spectrum of the improperly decoded pulses but also in that ... erly decoded pulses, which give rise to the tiny sidelobes in the time-domain cross-correlations. There are more notches in the improperly decoded spectrum than ... properly decoded one because the former one has more $0 \leftrightarrow \pi$ transitions.

In summary, we successful demonstrate femtosecond pulse encoding and decoding ... two identical programmable pulse shapers connected in tandem. The high ... asts in peak intensity and duration between the properly and in properly decoded ... can be further enhanced by the use a nonlinear thresholder [63] which we will ... er in the next chapter.

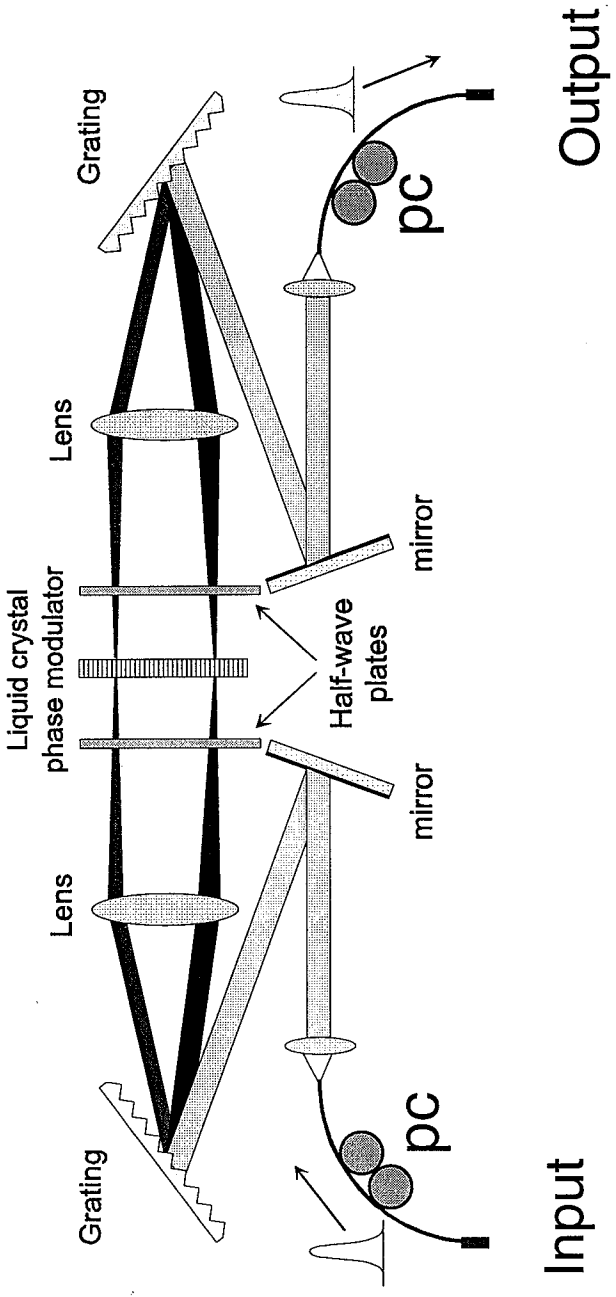

Fig. 4.1. Schematic of a programmable fiber-pigtailed femtosecond pulse shaper. a programmable 128-element liquid crystal phase modulator array (LCM) is placed at Fourier plane for spectral filtering. PC: polarization controller

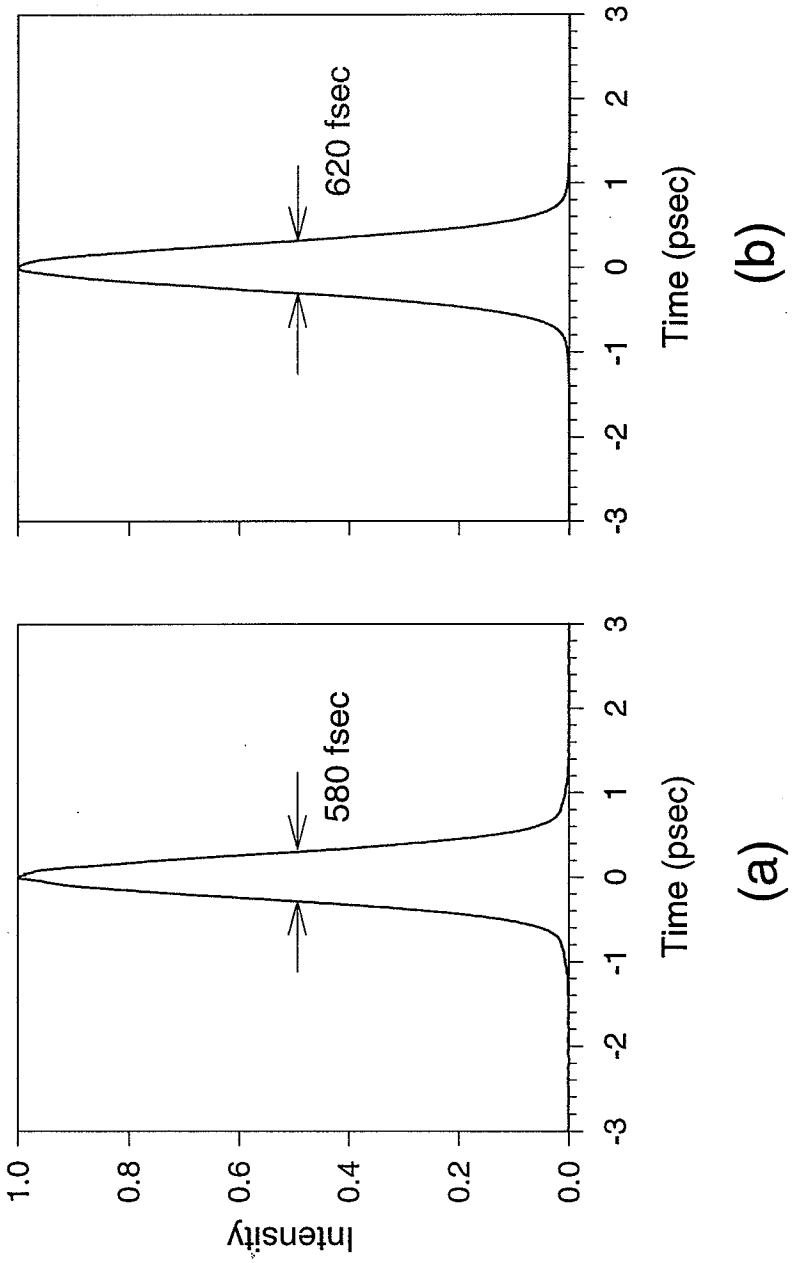

Fig. 4.2. Autocorrelation traces for the input (a) and output (b) pulses of a single pulse shaper. Autocorrelation widths of 580 fsec and 620 fsec correpond to pulsewidth of 410 fsec and 430 fsec, respectively.

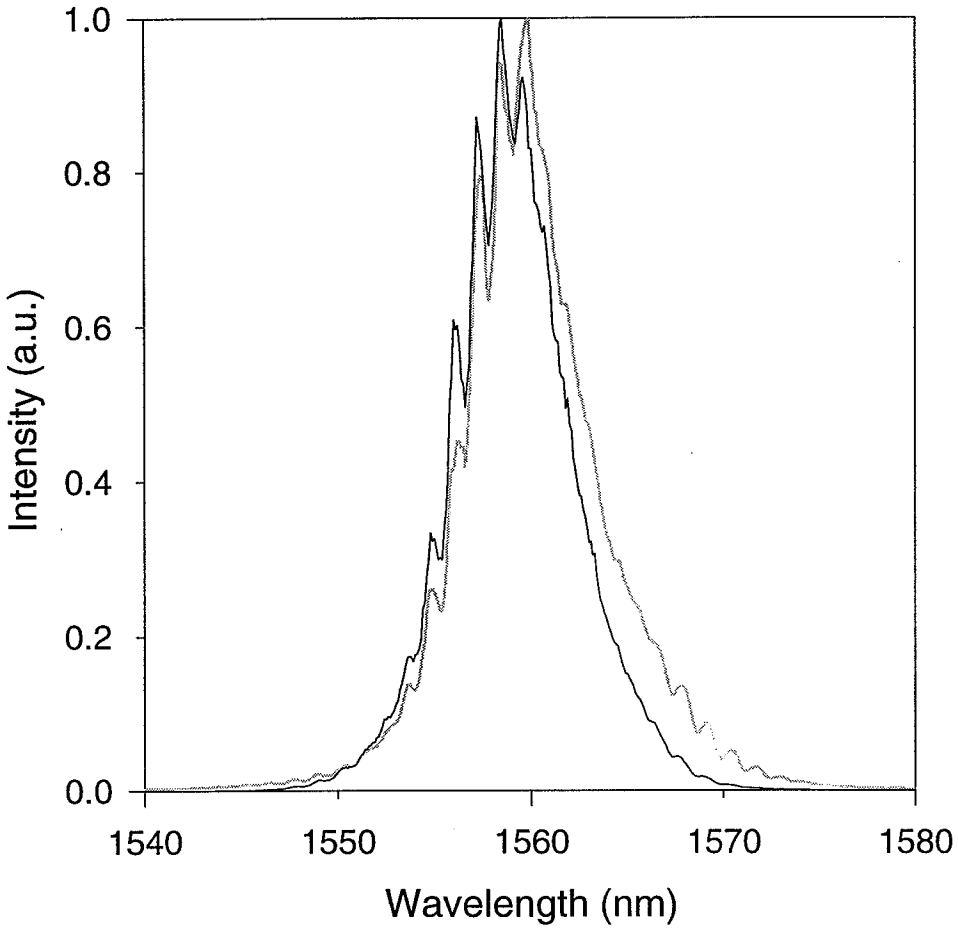

Fig. 4.3. Input (lighter line) and output (darker line) power spectra from a single pulse shaper. The slight narrowing in the output spectrum can be attributed to some polarization effects.

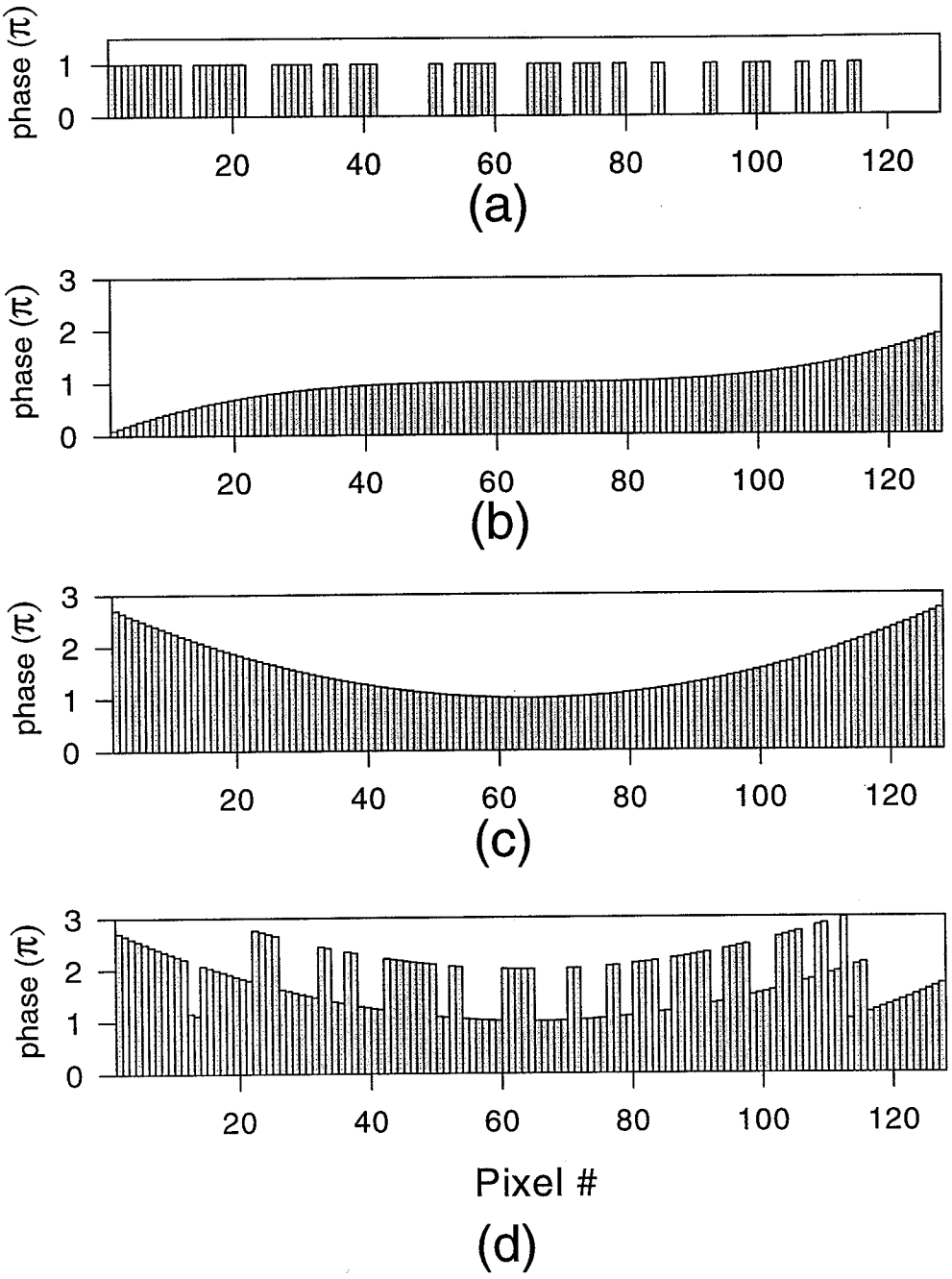

Fig. 4.4. Schematic diagrams of several different phase functions applied to LCM. (a):length-63 maximal length binary sequence (M-sequence); (b): cubic phase variation; (c): quadratic phase variation; (d): length-63 M-sequence combined with quadratic phase function.

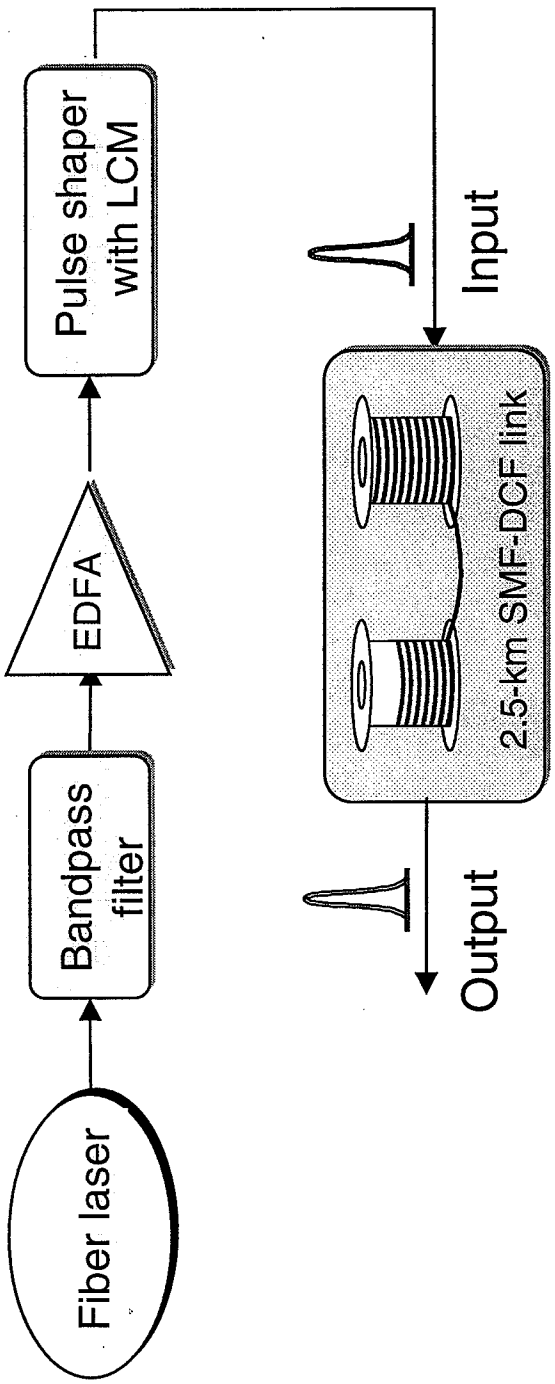

Fig. 4.5. Block diagram for the dispersion compensation experiments using the combination a DCF and a programmable pulse shaper. The DCF is used for coarse dispersion compensation and the programmable pulse shaper is used for dispersion fine-tuning.

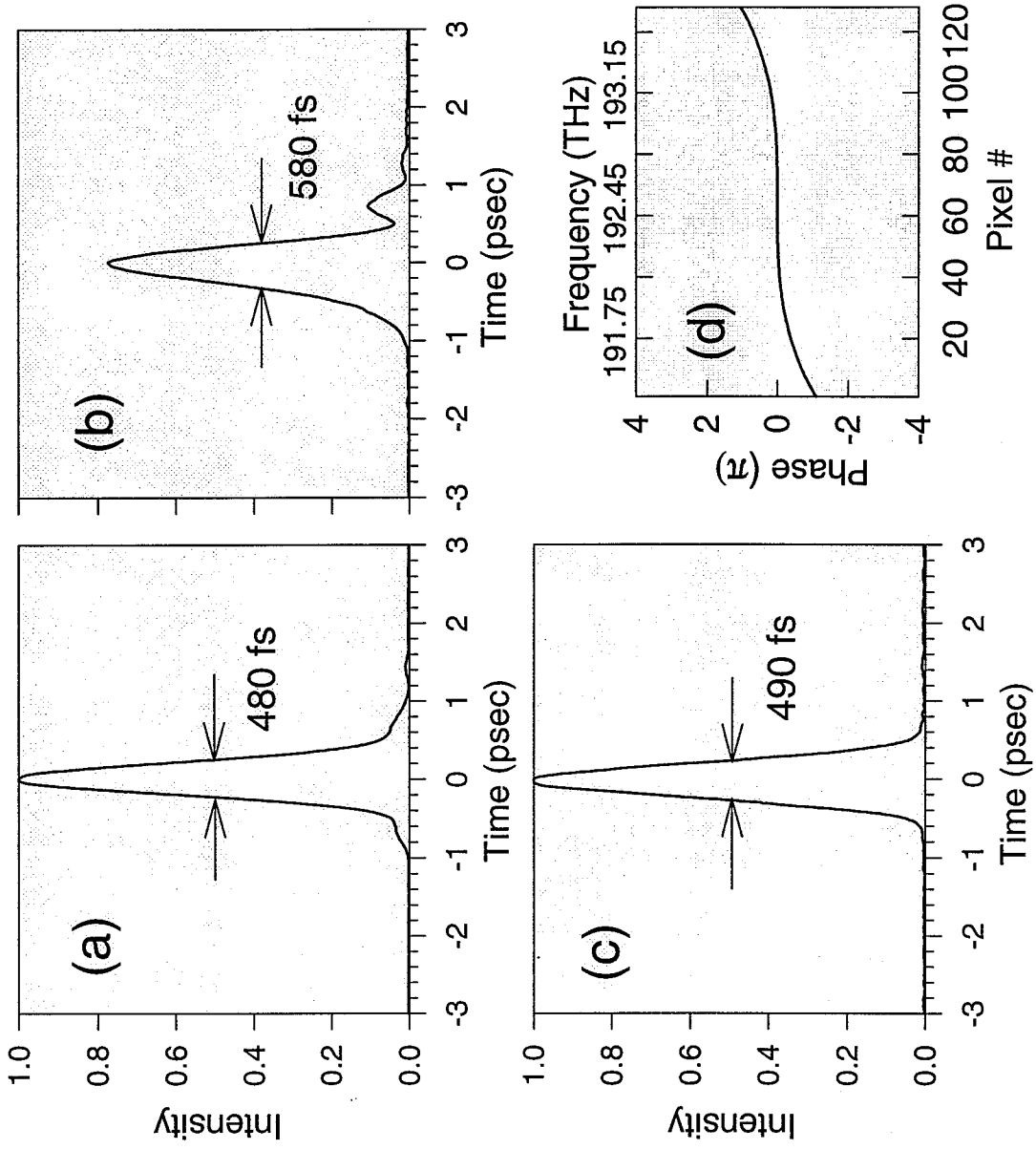

Fig. 4.6. Input pulse to the 2.5-km fiber link (a) and output pulse from the fiber link when constant phase (b) or cubic phase correction (c) is applied to LCM. Part (d) shows the cubic phase correction function.

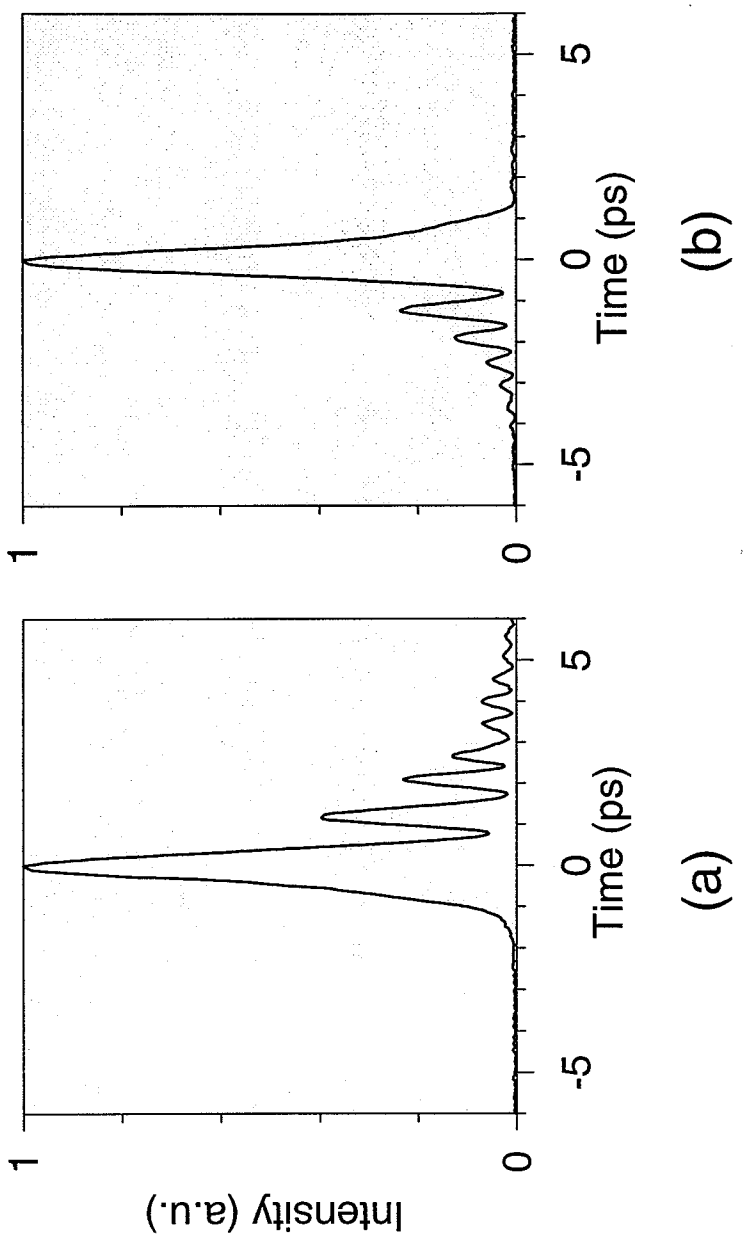

Fig. 4.7. Examples of pulse shaping using LCM applied with a cubic phase. Intensity cross-correlation measurements of the output pulses from the 2.5-km SMF-DCF link when cubic phase of -0.25 ps^3 (total -0.31 ps^3) (a) and +0.25 ps^3 (total +0.19 ps^3) (b) is applied to the LCM

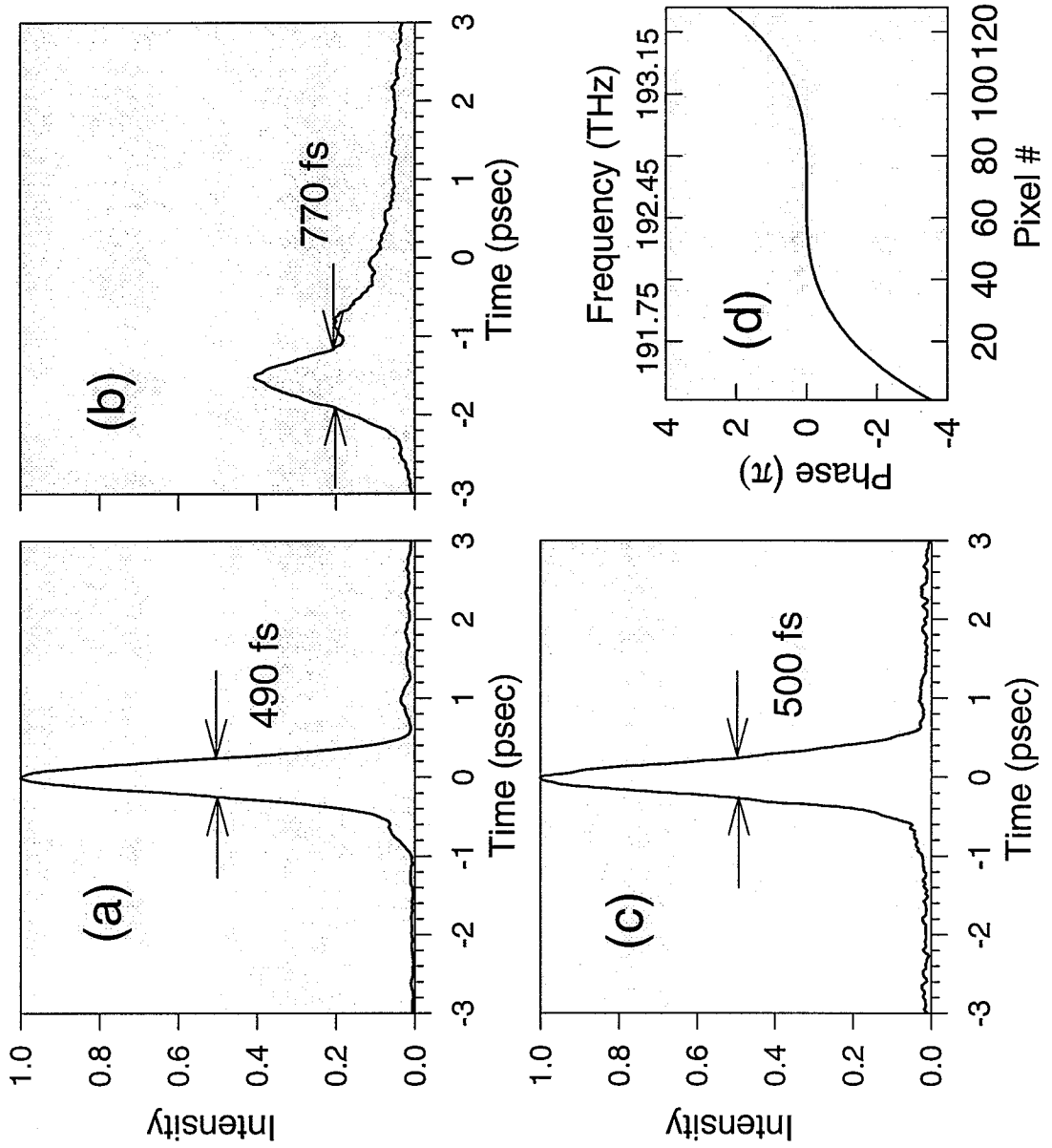

Fig. 4.8. Input pulse to the 3-km SMF-DCF-DSF fiber link (a) and output pulse from the fiber link when constant phase (b) or cubic phase correction (c) is applied to LCM. Part (d) shows the cubic phase correction function.

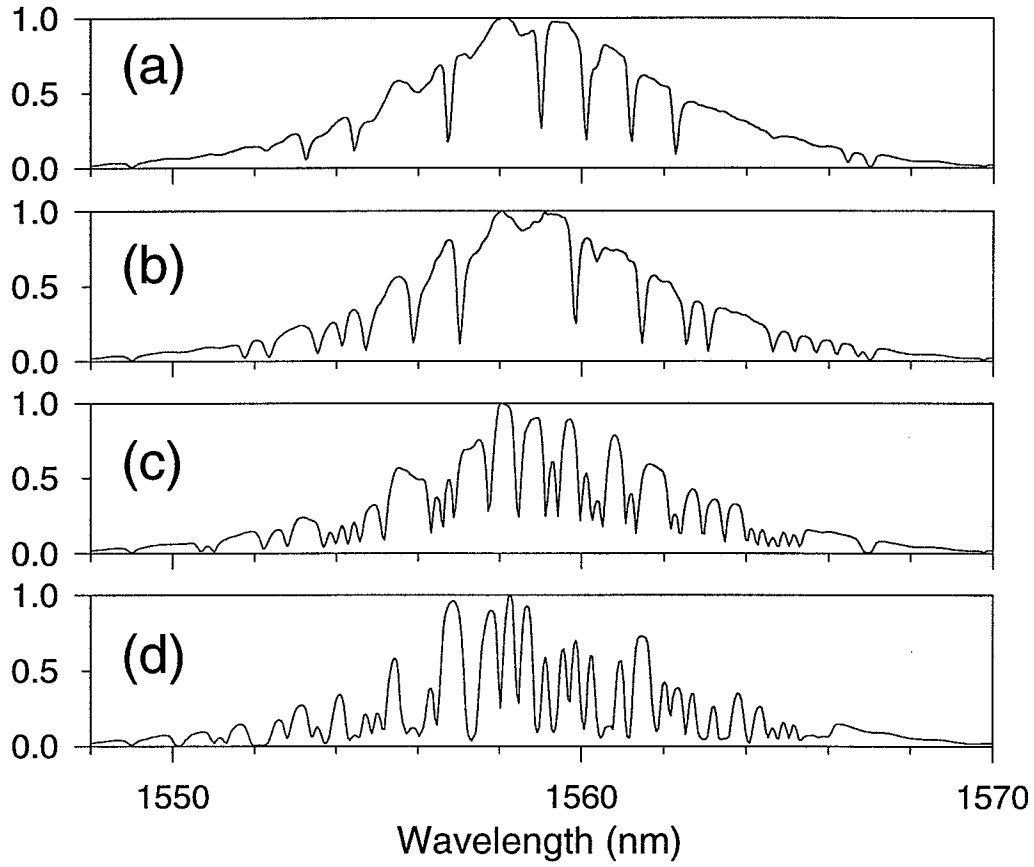

Fig. 4.9. Experimental encoded power spectra correspond to (a) length-15, (b) length-31, (c) length-63, and (d) length-127 M-sequence codes.

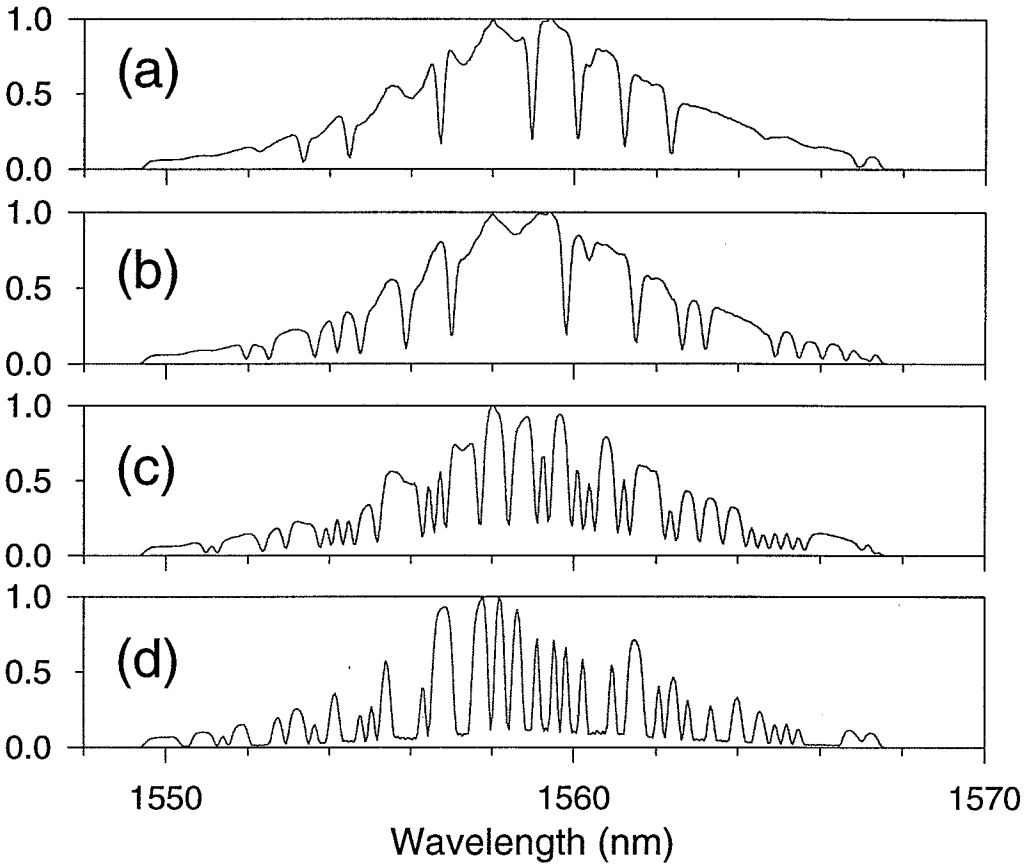

Fig. 4.10. Numerical simulation for encoded power spectra corresponding to (a) length-15, (b) length-31, (c) length-63, and (d) length-127 M-sequence codes

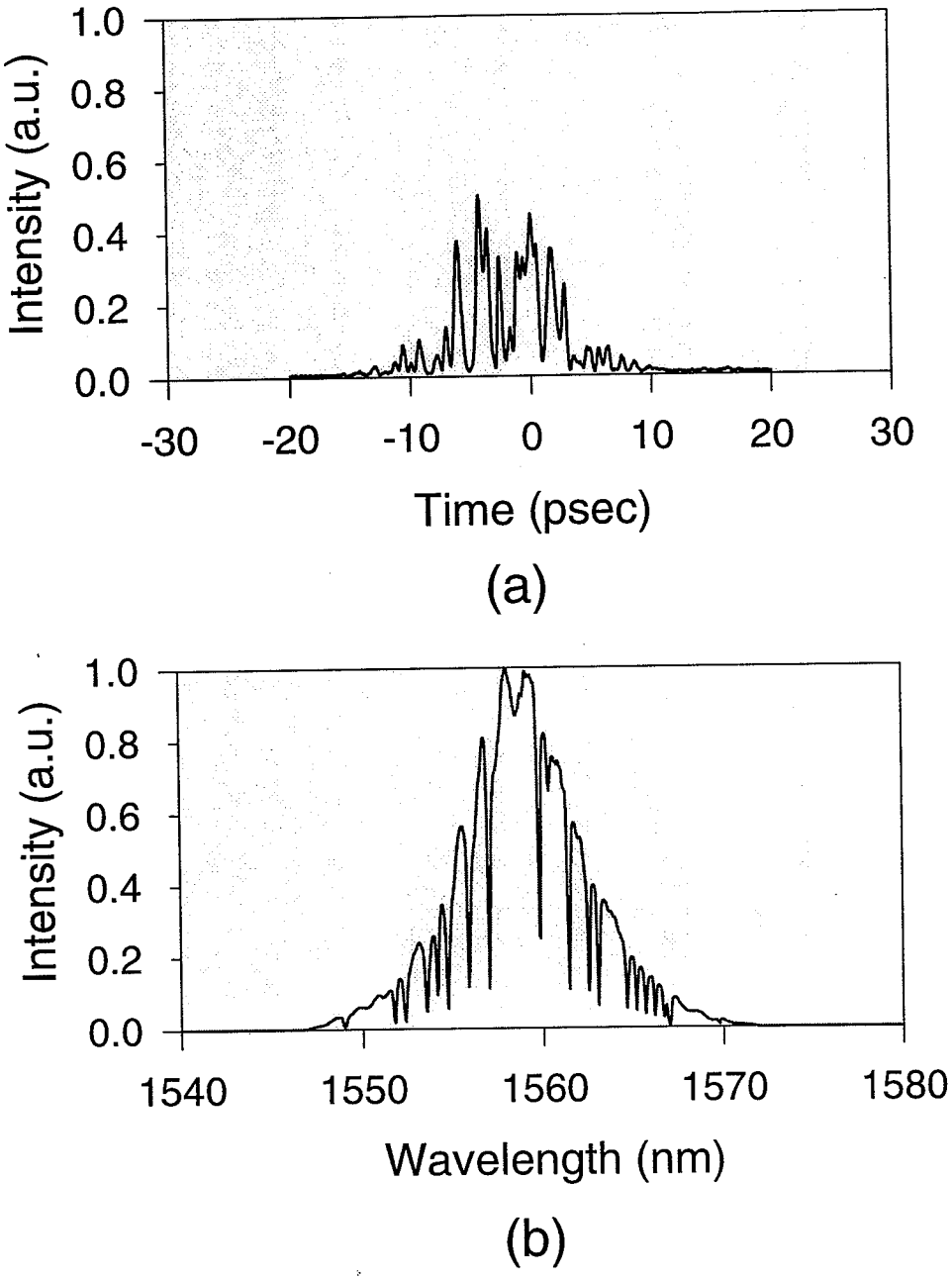

Fig. 4.11. Intensity profile (a) and power spectrum (b) of a pulse encoded with Length-31 M-sequence code

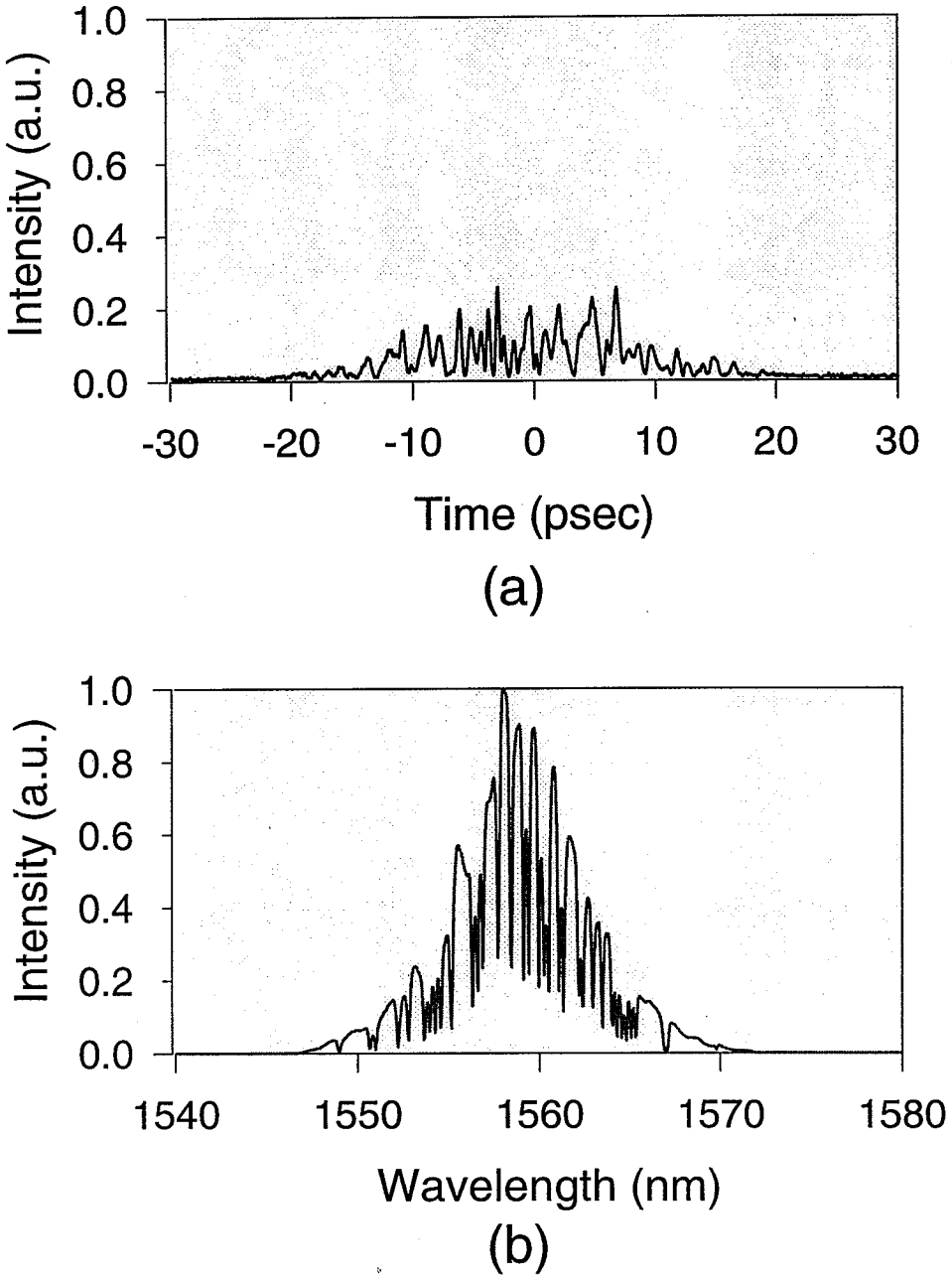

Fig. 4.12. Intensity profile (a) and power spectrum (b) of a pulse encoded with Length-63 M-sequence code

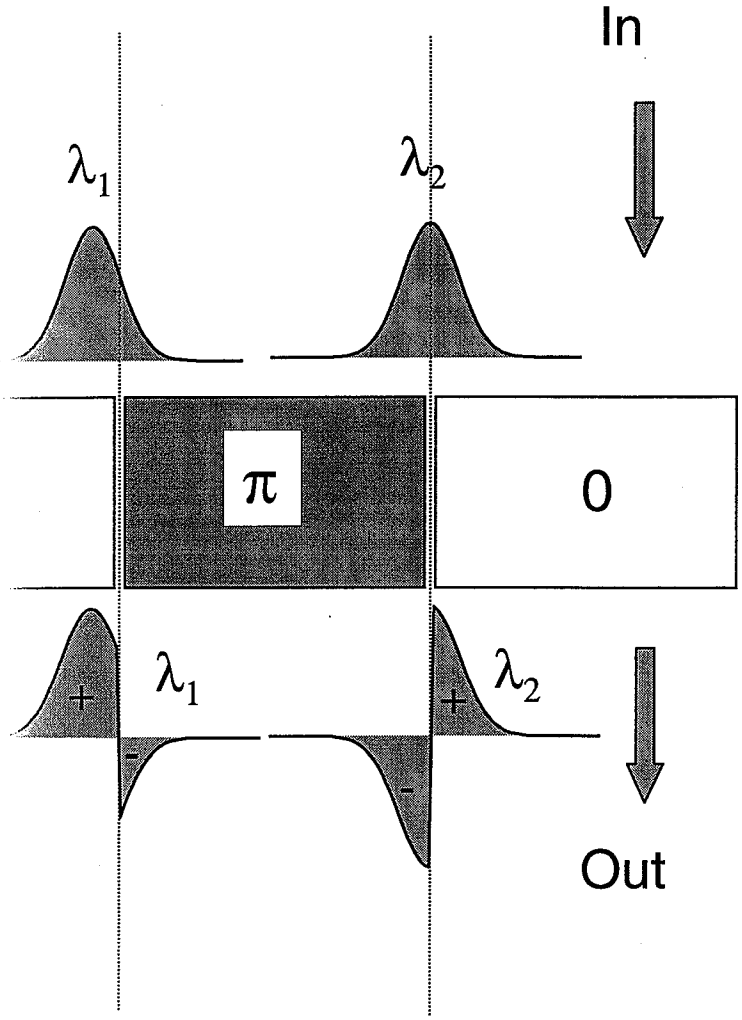

Fig. [illegible] distribution Gaussian beams before and after LCM. The positive and negative parts of the beam cancel each other at the fiber core due to destructive interference. The spectral intensity at wavelength λ_2 would be lower than that at λ_1 because the positive and negative parts of λ_2 are more of equal magnitude and cancel out more.

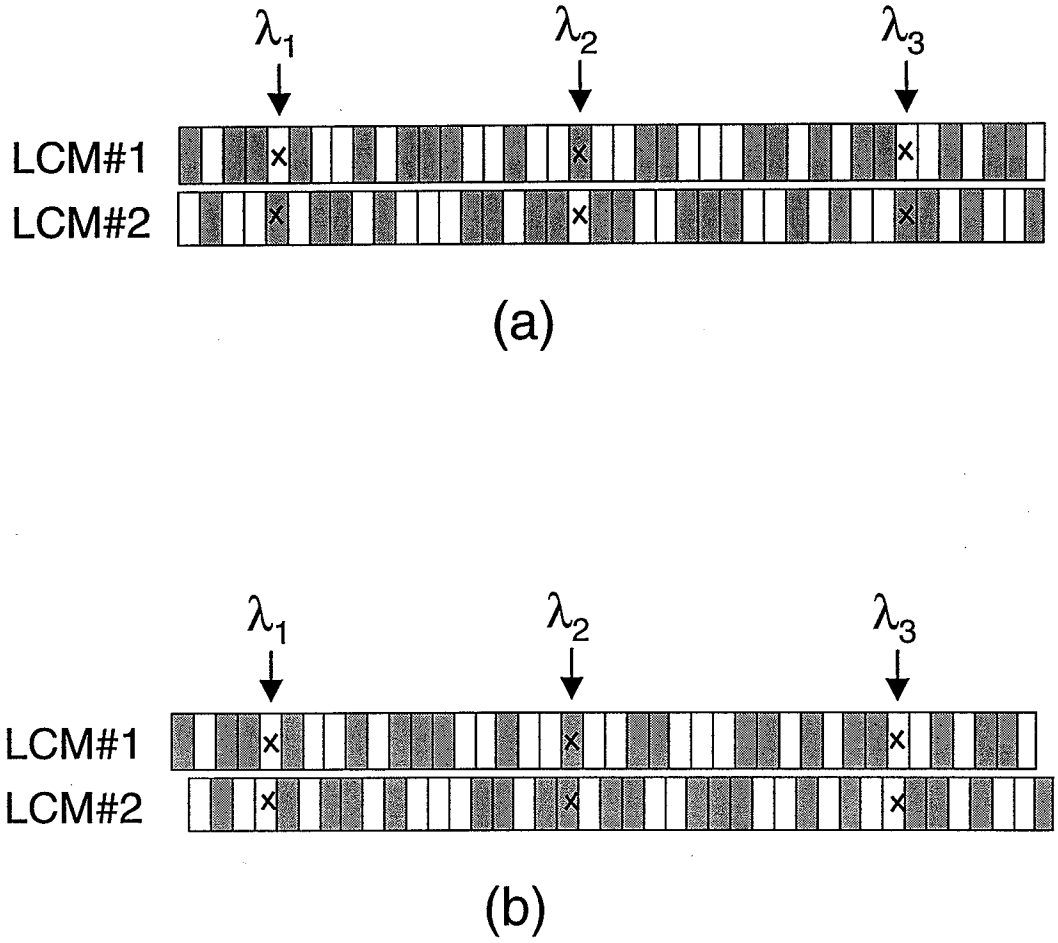

Fig. 4.14. Schematics of alignment of the encoder and decoder pulse shapers. (a) shows the two pulse shapers are aligned so the same wavelength components hit on the the same corresponding pixels in two LCMs. (b) shows some misalignment between the two pulse shapers.

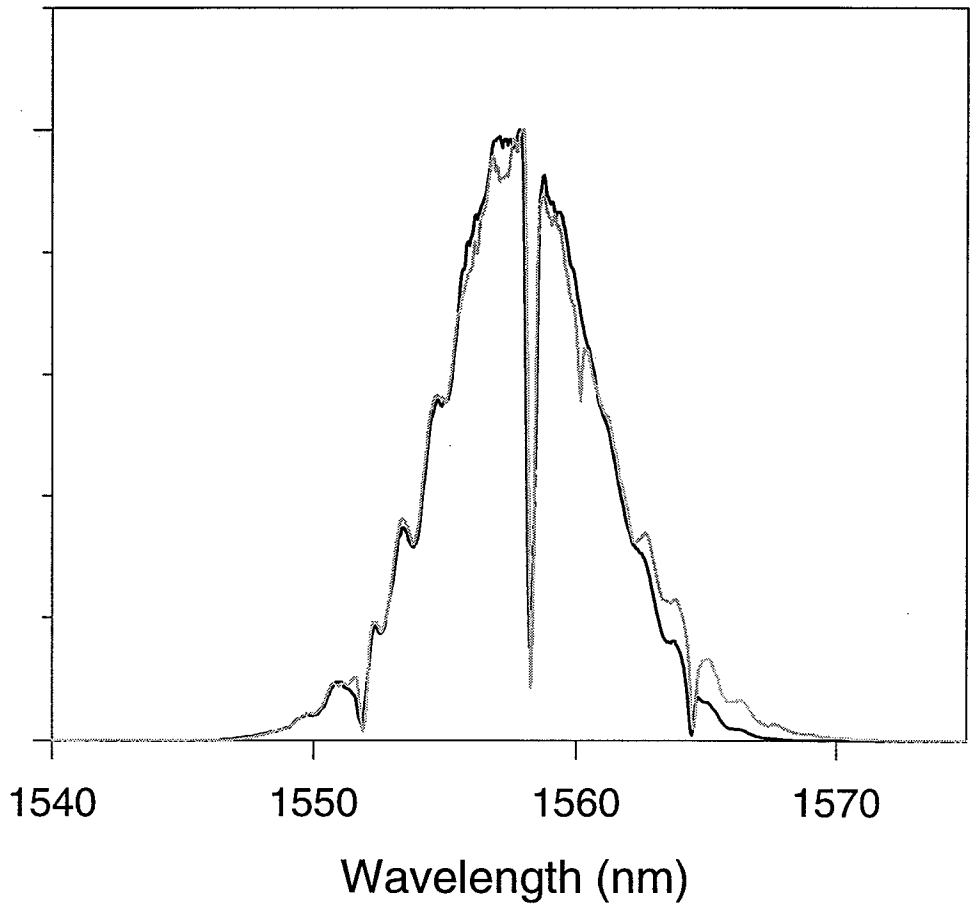

Fig. 4.15. Alignment of the encoder and decoder pulse shapers. Output Power spectra from both pulse shapers when three pixels, #10, #64, and #110, are applied with a π phase jump. The darker and lighter lines corresponds to the encoder and decoder output spectra, respectively

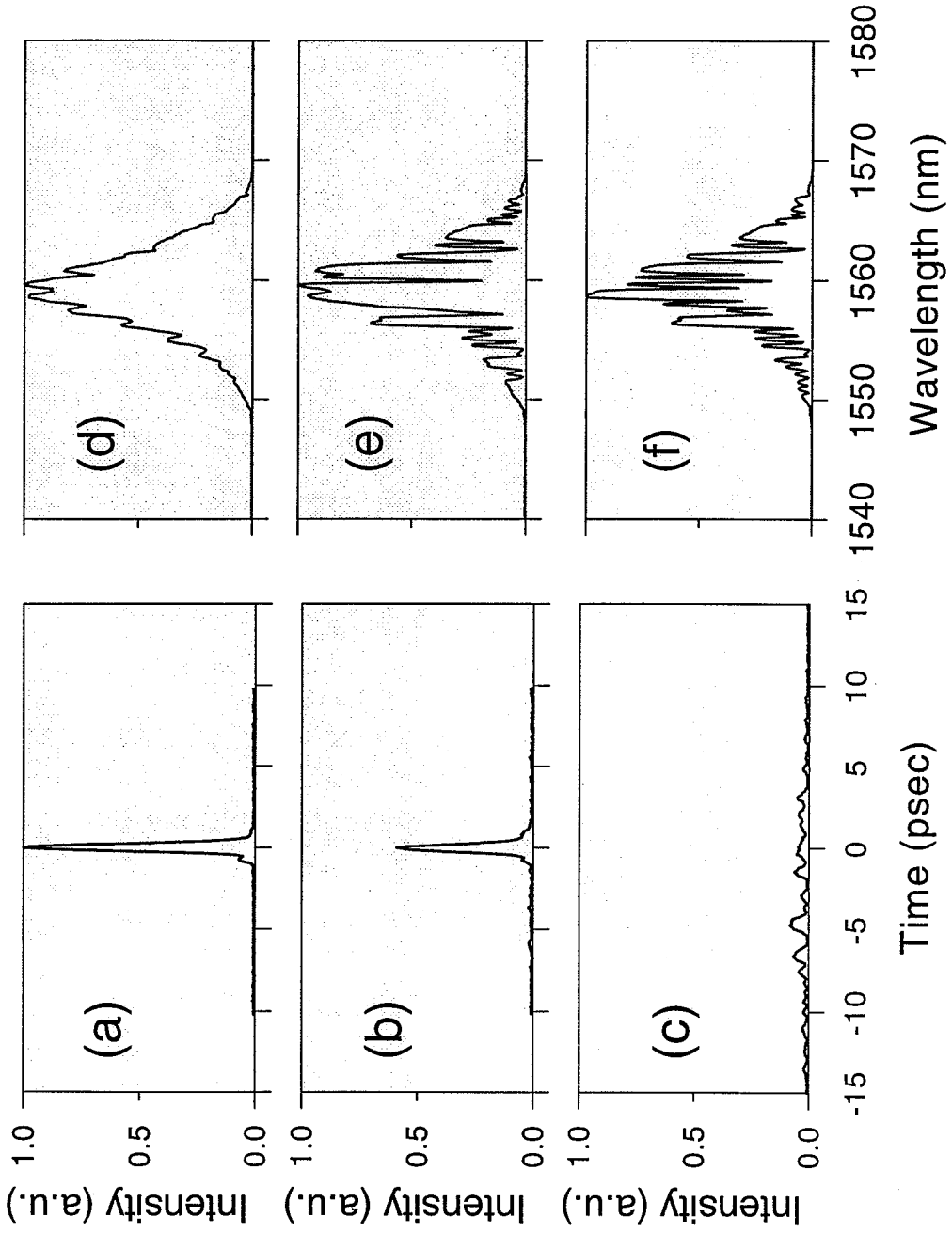

Fig. 4.16. Intensity profile of an uncoded (a) properly decoded (b), and improperly decoded pulses (c) and their corresponding power spectra (d), (e), and (f) for length-31 M-sequence codes

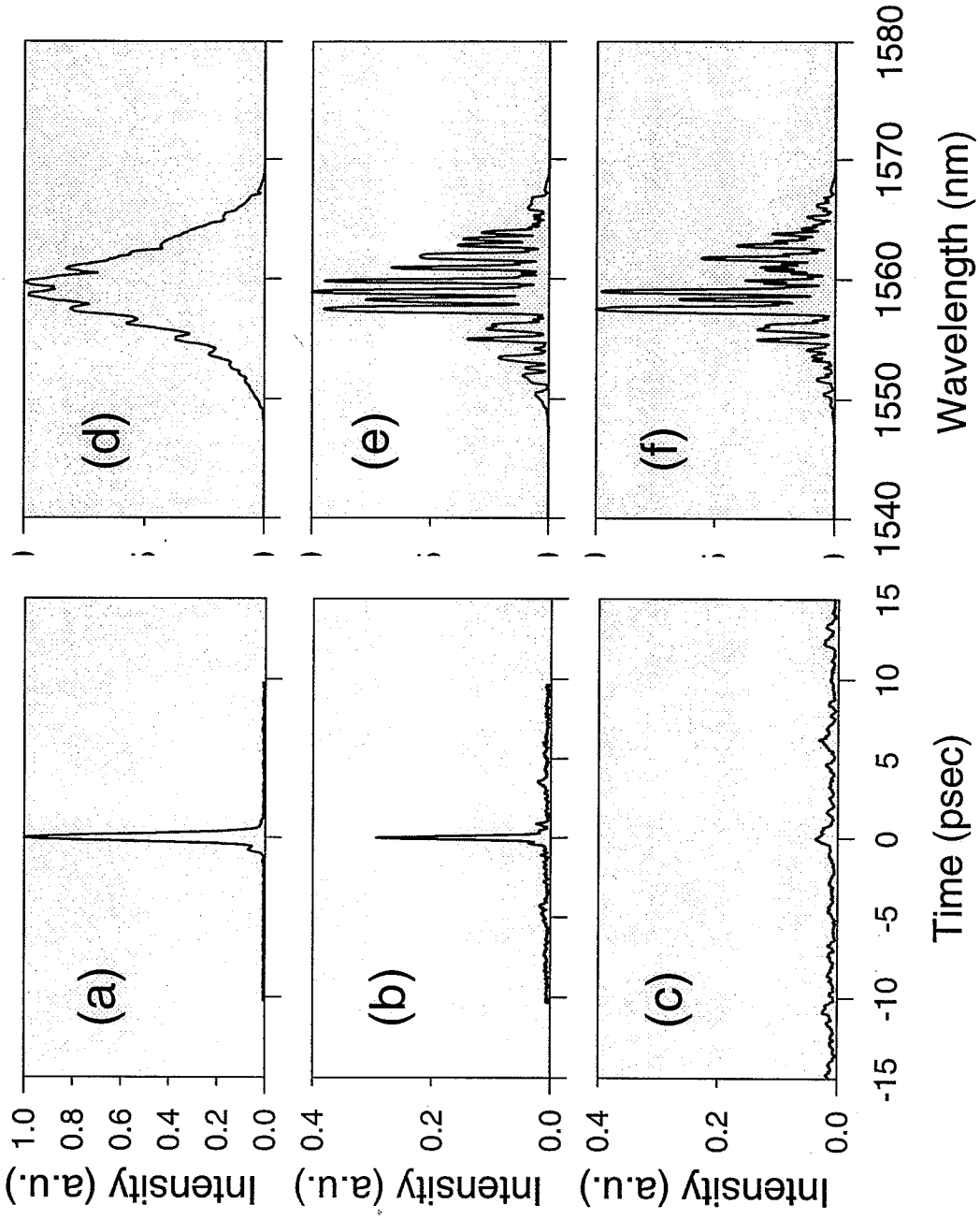

Fig. 4.17. Intensity profile of an uncoded (a) properly decoded (b), and improperly decoded pulses (c) and their corresponding power spectra (d), (e), and (f) for length-63 M-sequence codes

5. SYSTEM INTEGRATION

Successful operation of a CDMA system depends on the performances of three key sub-systems : low-dispersion transmission fiber link (dispersion compensation), high-fidelity encoding/decoding (identical pulse shapers), and high-contrast nonlinear thresholder. As discussed in the previous chapters, we have successfully demonstrated excellent performances of the first two sub-systems. A nonlinear fiber-optic thresholder with 30 dB contrast has also been developed [63]. Here in this chapter we will demonstrate the integration of these sub-systems into a single-user CDMA system and use it as a CDMA testbed to perform some system experiments.

5.1 Coded Pulses Fiber Transmission

The very first step in system integration is to combine the first two sub-systems (fiber link transmission and encoding/decoding) to study the very essence of a femtosecond CDMA system: generation, propagation, and decoding of femtosecond *coded* pulses. To do so, the two pulse shapers (encoder and decoder) are connected with 2.5-km SMF-DCF link in between. Femtosecond (350-500 fsec FWHM and ~1 mW average power) pulses from the fiber laser source (including mode-locked fiber laser, interference filter, and EDFA) are sent to the encoder pulse shaper (insertion loss ~5.5 dB) for phase coding; the encoded pulses then propagate over 2.5-km transmission fiber link before entering the second pulse shaper (decoder). Because the coded pulses have low average power (~200 μW) and long duration (10 psec) there is no noticeable nonlinear effect in the fiber transmission. Linear fiber transmission of the encoded pulses is a necessary condition for subsequent successful decoding. The

output pulses from the decoder having an even lower power of ~50 μW are amplified by a second chirped-pulse EDFA (denoted as post amplifier) before sent to an intensity autocorrelator for time-domain measurement.

Figure 5.1 shows the autocorrelation traces of output pulses for length- 15 (a), 31 (b), 63 (c), and 127 (d) M-sequence codes. The thicker lines in the figure corresponds to the properly decoded pulses while thinner lines the improperly decoded pulses. As expected, the contrast ratios in terms of the autocorrelation peaks between properly and improperly decoded pulses increase with the code length with the exception of the 127-element codes. The reason may be that the decoding of 127-element codes degrades due to the fact the spectral resolution cannot resolve physical features smaller than 1.3 pixel width and therefore the detailed structures of the 127-element code sequences are smeared out. Another way to look at it is that the notches (due to finite spectral resolution) in the power spectrum for length-127 codes are so many that they create a lot of sidelobes [see Figure 5.1 (d)] and significantly reduce the magnitude of the main peak in the correlation. The plots in the Figure 5.1 do not show the relative correlation peak intensity between codes of different length since they are normalized to their individual properly decoded signal peak. Figure 5.2 puts together the autocorrelations of the uncoded pulses and properly decoded pulses for various code lengths with all of the correlations normalized to the peak of the uncoded pulses. It's clearly shown in this figure that the magnitude of the correlation peak decreases with code length because longer codes have lower output power due to more notches in the power spectrum.

The transmission fiber link between the encoder and the decoder introduces frequency chirps to the pulses due to dispersion. Encoded pulses experience almost the same amount of dispersion as that would by uncoded femtosecond pulses with the same bandwidth. If there is some dispersion in the fiber link the decoded pulses will have a broader pulse width than the case when there is no dispersion in the transmission. The properly and the improperly decoded pulses will have the same broadening but because the properly decoded pulses have much shorter pulse width

their peak intensity are much more reduced. As a result, the contrast ratio decreases with the amount of dispersion. Figure 5.3 (a) shows the contrast between properly and improperly decoded pulses when there is some residual third-order dispersion in the 2.5-km SMF-DCF link. As we demonstrated in Chapter 4 (Figure4.4), the phase correction function together with M-sequence phase codes can be applied to LCM simultaneously to provide coding and dispersion fine-tuning. Figure 5.3 (b) shows the contrast between properly and improperly decoded pulses when a phase correction function is applied on top of the encoding M-sequence code. Compared to the decoding results shown in Figure 5.3 (c) corresponding to back-to-back configuration (no fiber link in between), Figure 5.3 (b) has nearly the same contrast ratio. This again proves the phase-optimized 2.5-km fiber link is almost dispersion-free, as we have demonstrated in Chapter 4.

5.2 Thresholding Results

Because properly and improperly decoded pulses have comparable average power level and very short duration, ordinary photodetectors cannot be used to determine if the intended signal is received. Instead, a nonlinear thresholder needs to be employed to distinguish correctly decoded pulses from incorrectly decoded pseudonoise bursts based on the pulse intensity and duration. As shown in Figure 5.4, our nonlinear thresholder consists of a passive optical fiber, a spectral filter, and a photodetectors [63]. The passive fiber used here is a 500-m dispersion-shifted fiber with zero dispersion wavelength of 1559 nm (which coincides with the mean wavelength of the spectrum used in our CDMA system). The spectral filter is a long wavelength pass filter consisting of a grating, a lens and a knife-edge mounted on a translation stage, as shown in Figure 5.4. The cutoff wavelength can be adjusted by moving the translation stage. Any output pulse energy filtered through the long wavelength pass filter is detected by a slower photodetector which can operate at speeds comparable to the repetition rate of the system.

The decoded pulses after amplification by post EDFA were sent to the passive optical fiber. Nonlinear effects (such as self-phase modulation) in the fiber cause the spectrum of the properly decoded pulse to split and spread [64] to either side of the zero dispersion point. The improperly decoded pulse propagates the same length of the thresholder fiber but experiences negligible spectral shifts due to its lower intensity and larger pulse width. Figure 5.5 (a) and (b) respectively show the autocorrelations of the amplified properly and improperly decoded pulses (length-63 codes) while Figure 5.5 (c) and (d) shows their corresponding power spectra after passing through the 500-m thresholder fiber. Clear spectral shift to longer wavelengths appears in Figure 5.5 (c) but not in (d). This differences in the longer wavelength components between these two spectra can be converted into a contrast in energy by the longpass spectral filter and photodetector. Also notice that the peak at 1530 nm observed on both the spectra is due to the amplified spontaneous emission (ASE) from the post-EDFA. Figure 5.6 shows the contrast ratios between the properly and improperly decoded signals for various signal power (corresponding to different EDFA pump power) in the nonlinear thresholder fiber. The nonlinearity in the thresholder can lead to enhanced contrast ratio compared to that obtained directly from the decoding. As seen in Figure 5.6 contrast ratios as high as 15 dB and 20 dB are demonstrated for length-63 and length-31 M-sequences respectively when the filter cutoff wavelength is chosen at 1573 nm. The reason length-31 encoding/decoding has higher contrast ration for the same pump level is that as we mentioned earlier insertion loss of coders increases with the code length and therefore the output power is lower and thus the spectral shift is less for length-63 codes compared to length-31 codes.

The number of orthogonal M-sequence codes which limits the maximum number of CDMA users is determined by the code length. For example, a CDMA system using M-sequence of length 63 (which has 63 orthogonal codes) can support 63 different users. If a CDMA system can use two or more M-sequences of different lengths, it can accommodate more users. For example, a CDMA system in which some users are assigned length-31 M-sequence codes and the others length-63 codes can provide a

maximum of 94 users. The question is that can M-sequence codes of different lengths co-exist? Or are length-31 codes "orthogonal" to length-63 codes? The scheme of mixing code lengths would work if the decoded interference signals coming from users of different code lengths still remain as low-intensity wide-spread noisebursts and introduce only negligible spectral shift in the thresholder fiber. Encoding/decoding of various code length combination were conducted: (1) 31-31 non-conjugate (or orthogonal); (2) 63-31 non-conjugate; (3) 31-31 conjugate; (4) 63-63 non-conjugate (or orthogonal); (5) 31-63 non-conjugate; (6) 63-63 conjugate. The first number is the code length applied to encoder while the second code length applied to decoder. For example, 63-31 non-conjugate means the encoder is applied with a length-63 code and decoder with a length-31 code. Figure 5.7 (a), (b), and (c) show the output power spectra from thresholder fiber corresponding to case (1), (2), and (3) respectively. Figure 5.8 (a), (b), and (c) show the output power spectra from thresholder fiber corresponding to case (4), (5), and (6) respectively. These power spectra all correspond to post-EDFA pump power of 64 mW, the maximum pump level available in our current pumping setup. As seen in the part (b) of Figure 5.7 and Figure 5.8, no obvious spectral shift are observed in the 31-63 and 63-31 coding schemes.

In evaluating the energy contrast performances of the various encoding/decoding scenarios at photodector's end, we compared the energy detected for 63-31 and 31-31 non-conjugate coding schemes to that for 31-31 (63-63) conjugate codes because this corresponds to the situation where the intended received signals are of code length 31 and the interference signals are of length 63 (63-31 non-conjugate) or 31 (31-31 non-conjugate). Similarly, 31-63 and 63-63 non-conjugate thresholding results are compared to that of 63-63 conjugate. Figure 5.9 shows contrast ratios at four different EDFA pump level for a decoder with length-31 codes when interference signals are encoded with length-63 (line A) or length-31 (line B) codes and for a decoder with length-63 codes when interference signals are encoded with length-63 (line C) or length-31 (line D). The fraction of pulse energy detected by the photodetector depends on the amount of spectral shift and the cutoff wavelength. By adjusting the filter

cutoff position and the post-EDFA pump power, optimal energy contrast ratios can be obtained. In the earlier thresholding results shown in Figure 5.6, the contrast ratio is limited by the amplified spontaneous emission (ASE) from the second EDFA which spreads somewhat into the wavelength range over 1573 nm. This limitation can be alleviated by moving the cut-off wavelength to an even longer wavelength (1573 nm). As a result, contrast ratios as high as 28 dB for length-31 codes (line B) and 26 dB for length-63 codes (line C) are demonstrated. This is a great improvement compared to the results in Figure 5.6. The reason why line A (63-31) has higher contrast that line B (31-31) is that 63-31 improperly decoded pulses cause even less spectral shift than the 31-31 improperly decoded pulses because of less power and longer duration for the former case. Same reason applies to why line C (63-63) has higher contrast ratios than line D (31-63).

To summerize, in this chapter we have integrated one by one the three sub-systems of our single-user CDMA testbed. First, we combined fiber dispersion compensation with femtosecond encoding/decoding by demonstrating encoded pulse fiber transmission and subsequent decoding of output encoded pulses back to femtosecond pulses. The third sub-system, namely nonlinear thresholder, is finally added to convert the high contrast in peak intensity between properly and improperly decoded pulses to even higher contrast in detected energy. M-sequence codes of different lengths are shown to be "orthogonal" in a way and can be simultaneously used in the same CDMA system to increase the number of users.

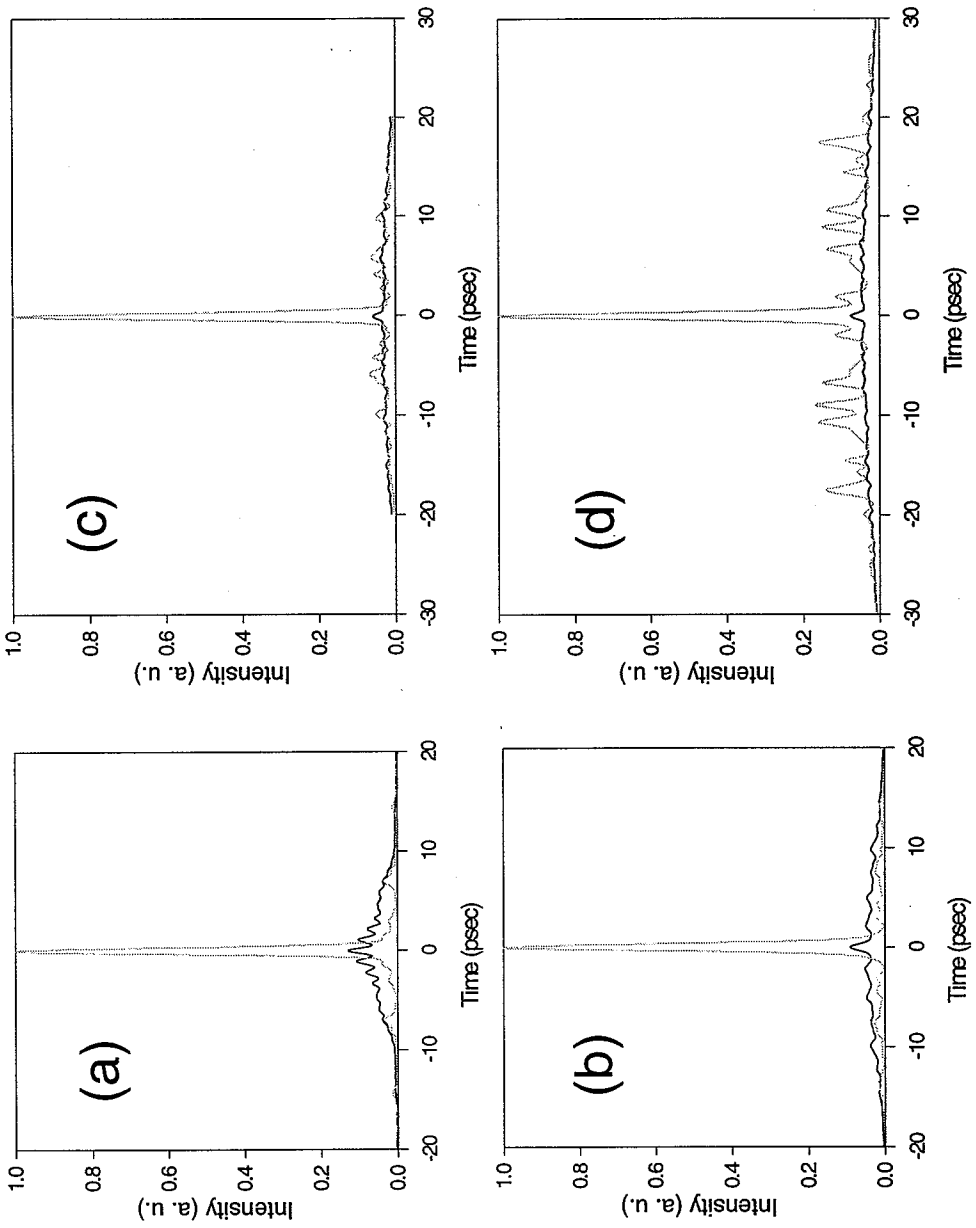

Fig. 5.1. Autocorrelation traces of output decoded pulses for length- 15 (a), 31 (b), 63 (c), and 127 (d) M-sequence codes. The lighter lines corresponds to the properly decoded pulses while darker lines the improperly decoded pulses.

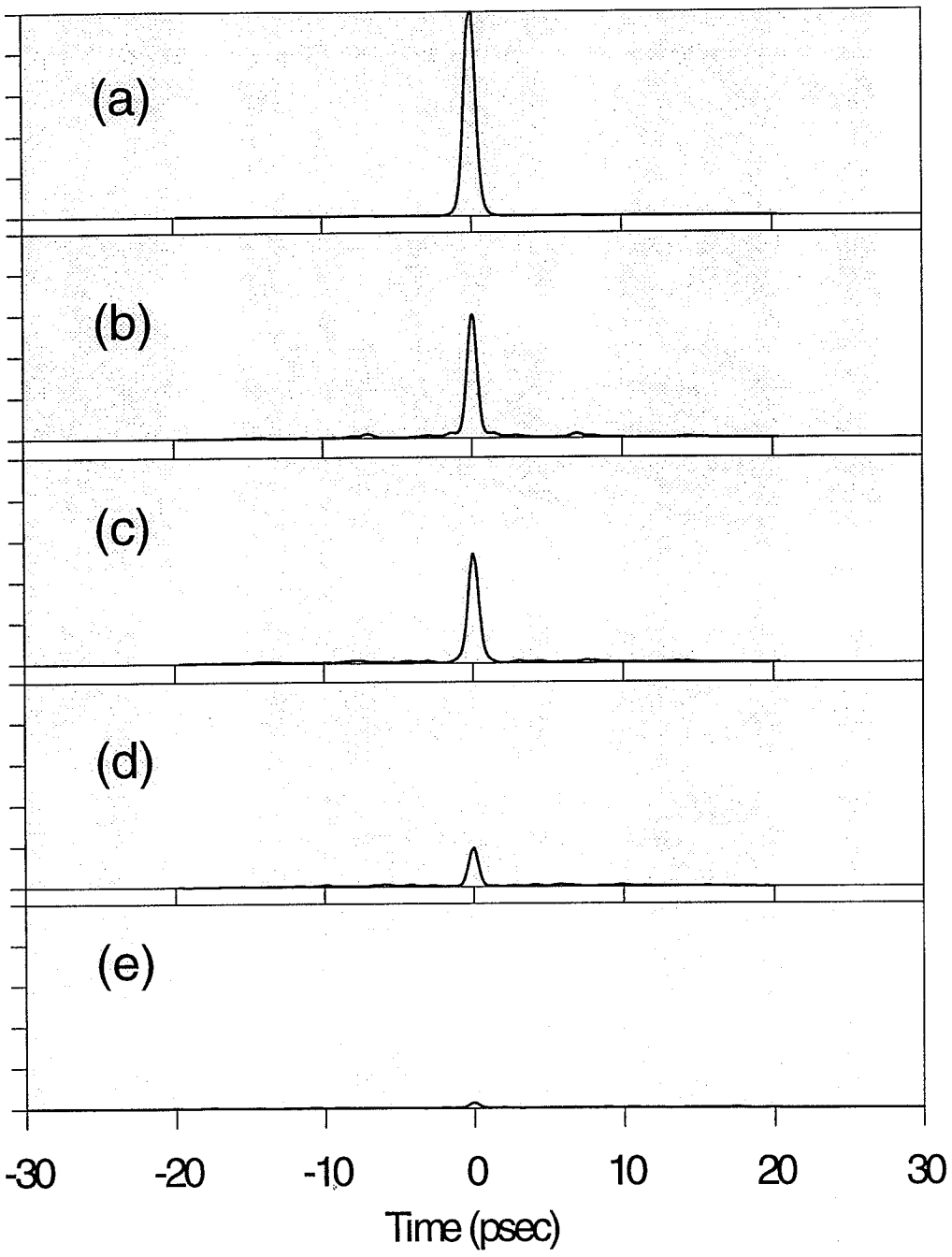

Fig. 5.2. Autocorrelation traces of the uncoded pulses (a) and properly decoded pulses for length-15, 31, 63, and 127 codes (corresponding to (b), (c), (d), and (e), respectivey) with all of the correlations normalized to the peak of the uncoded pulses

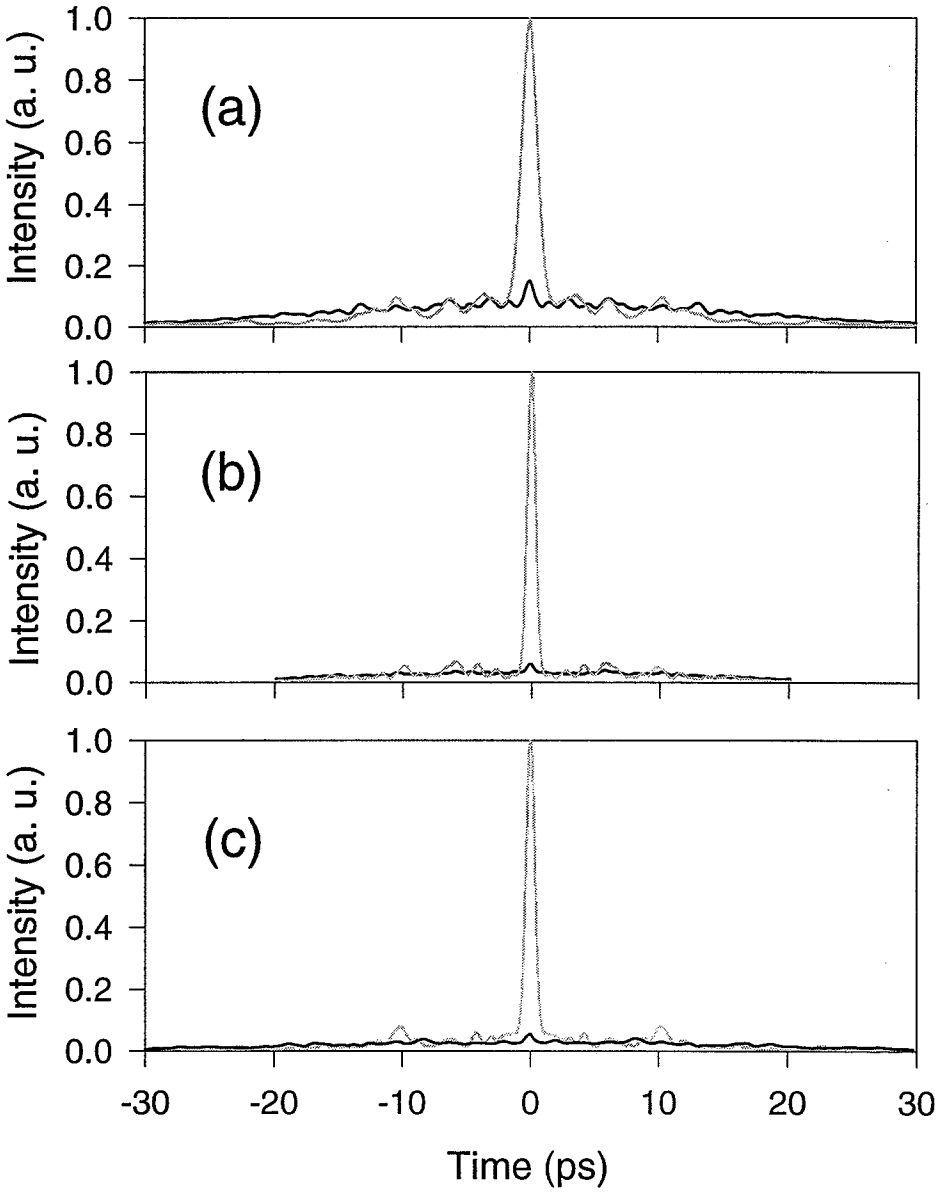

Fig. 5.3. Autocorrelation traces of the properly decoded pulses (a): when there is some residual third-order dispersion in the 2.5-km SMF-DCF link; (b): when the residual third-order dispersion is removed by cubic phase correction; (c): when no link between the encoder and decoder.

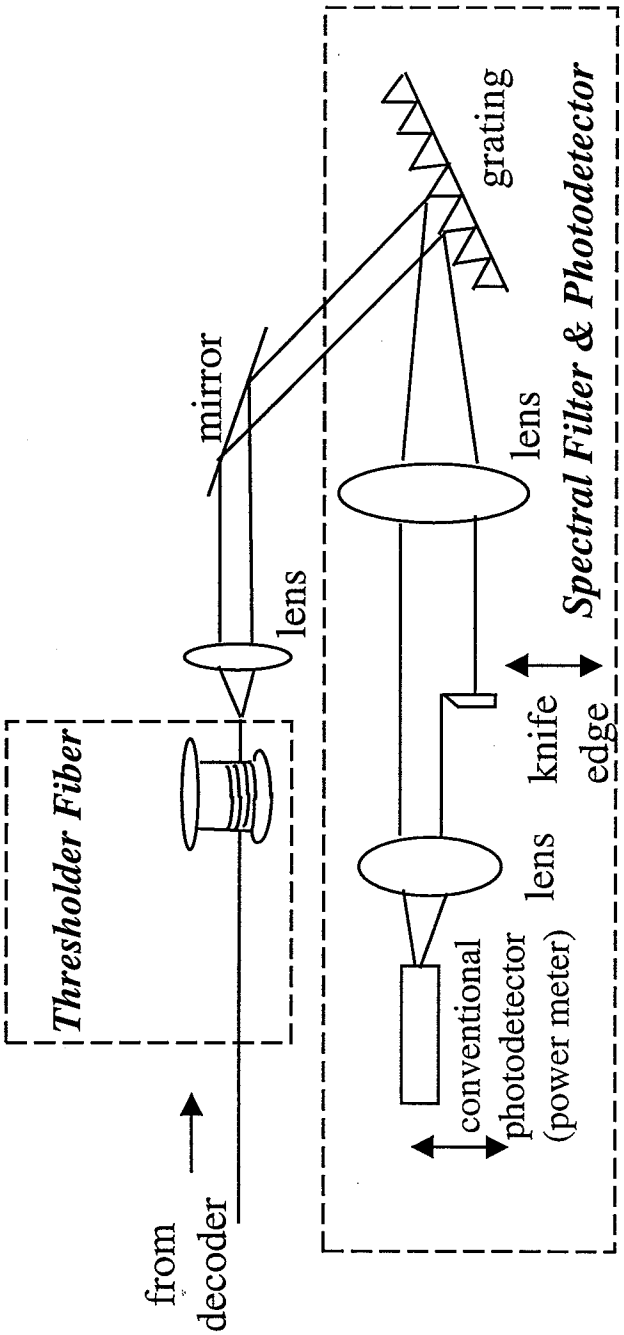

Fig. 5.4. Schematic of the nonlinear fiber-optic thresholder [54]

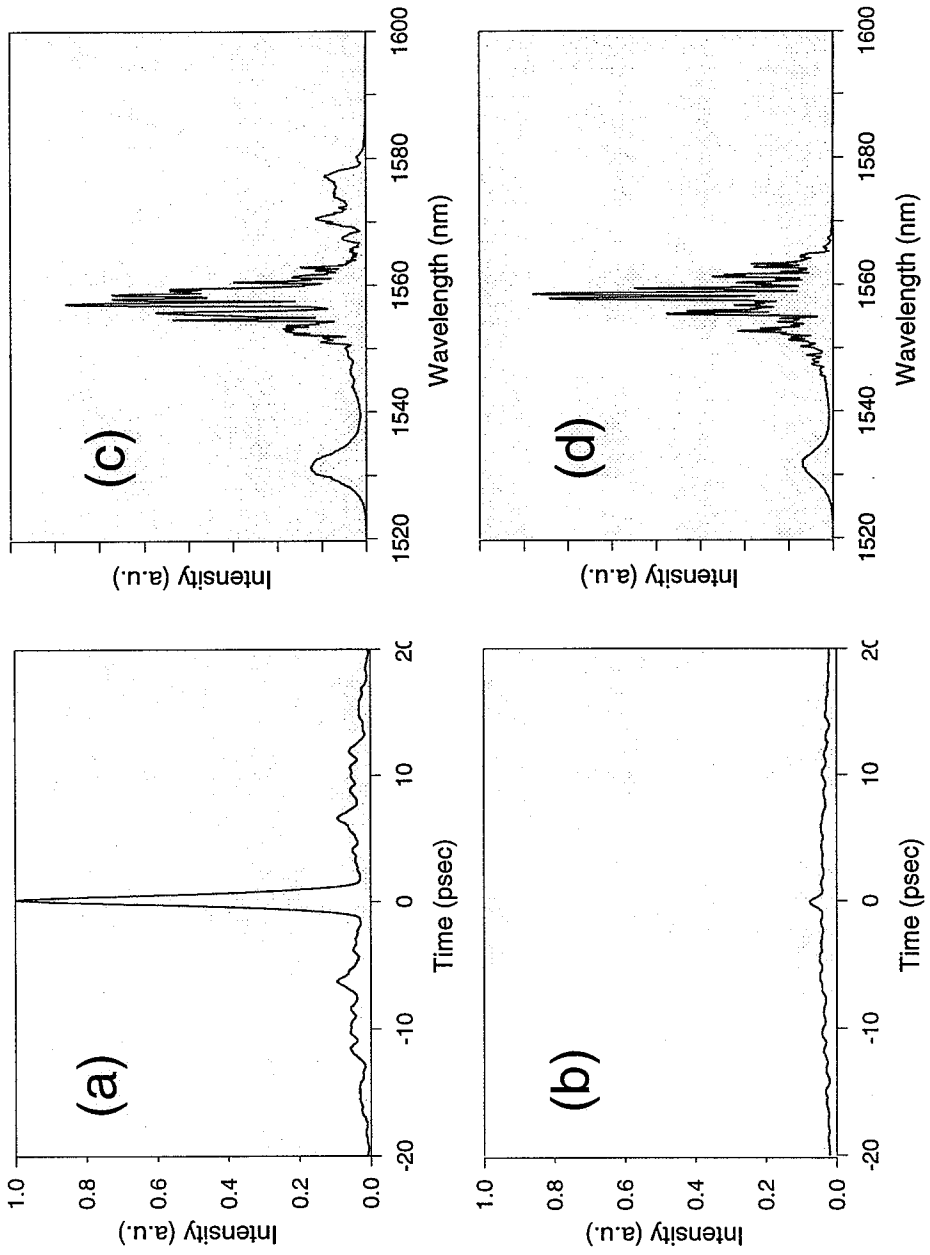

Fig. 5.5. (a): Intensity auto-correlation at the decoder output for a correctly decoded pulse, (b) intensity auto-correlation at the decoder output for an incorrectly decoded pulse, (c) and (d) power spectrum after the thresholder fiber corresponding to (a) and (b) respectively. The M-sequence phase code length is 63 elements and post-EDFA pump power is 64 mW in each case.

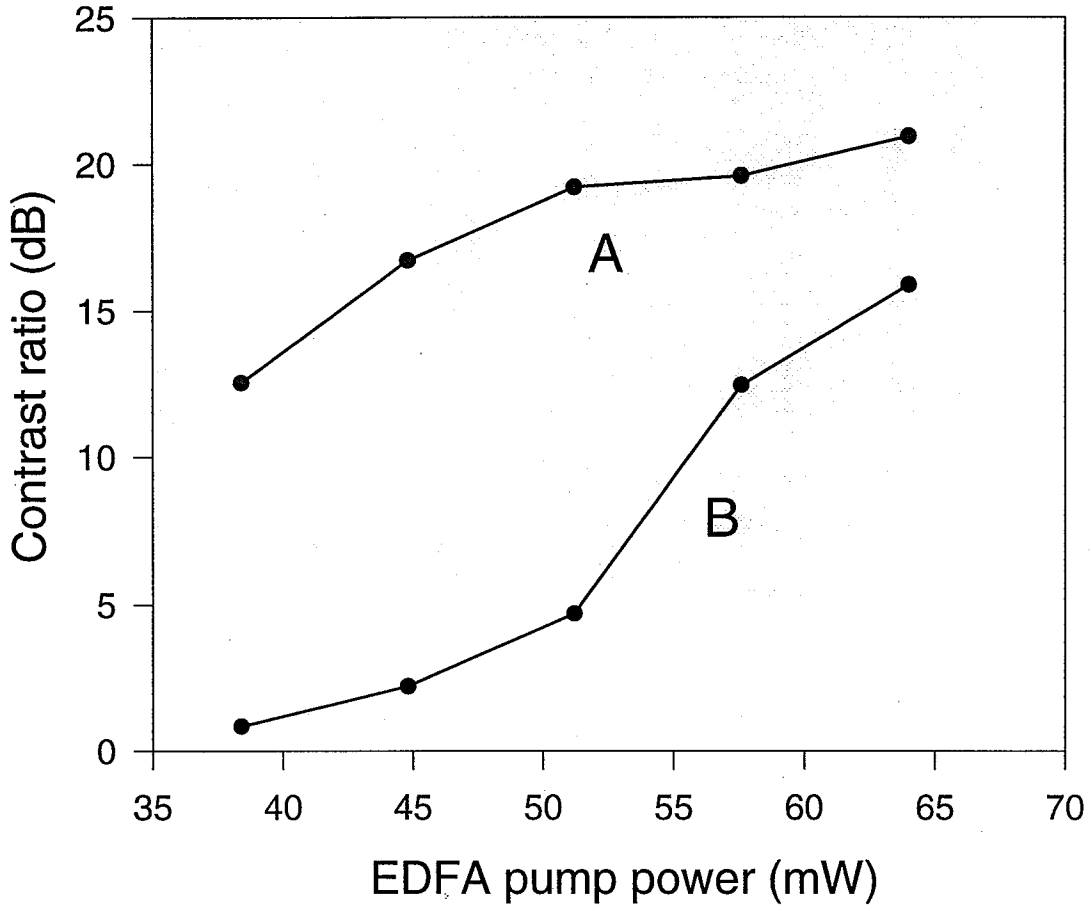

Fig. 5.6. Contrast ratios as function of EDFA pump power at the output of the nonlinear thresholder for length 31 (line A) and length 63 (line B) M-sequence phase codes. The filter cut-off wavelength is 1573 nm.

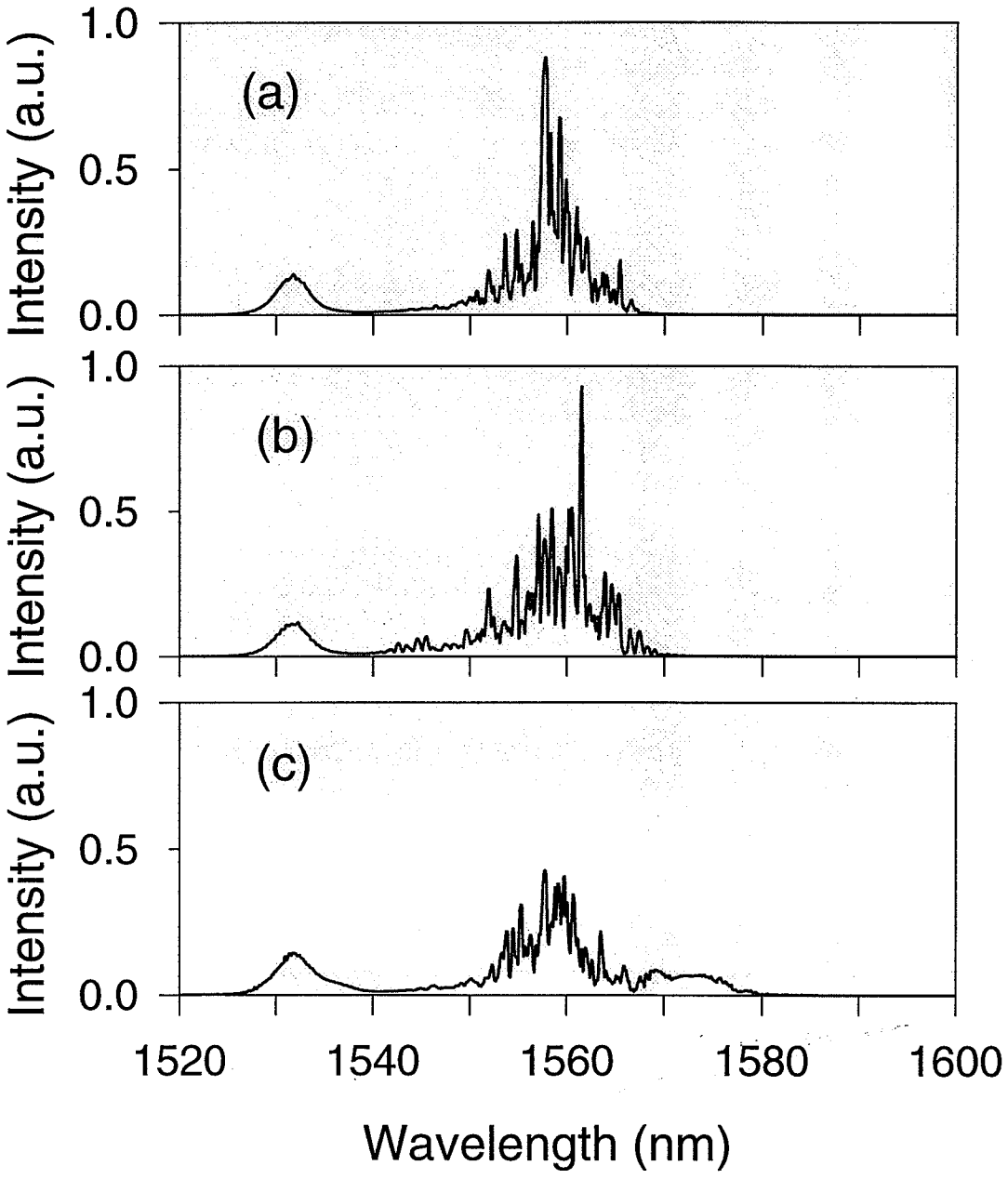

Fig. 5.7. Output spectra after thresholder fiber for (a): 31-31 non-conjugate (or orthogonal); (b): 63-31 non-conjugate; (c): 31-31 conjugate M-sequence codes

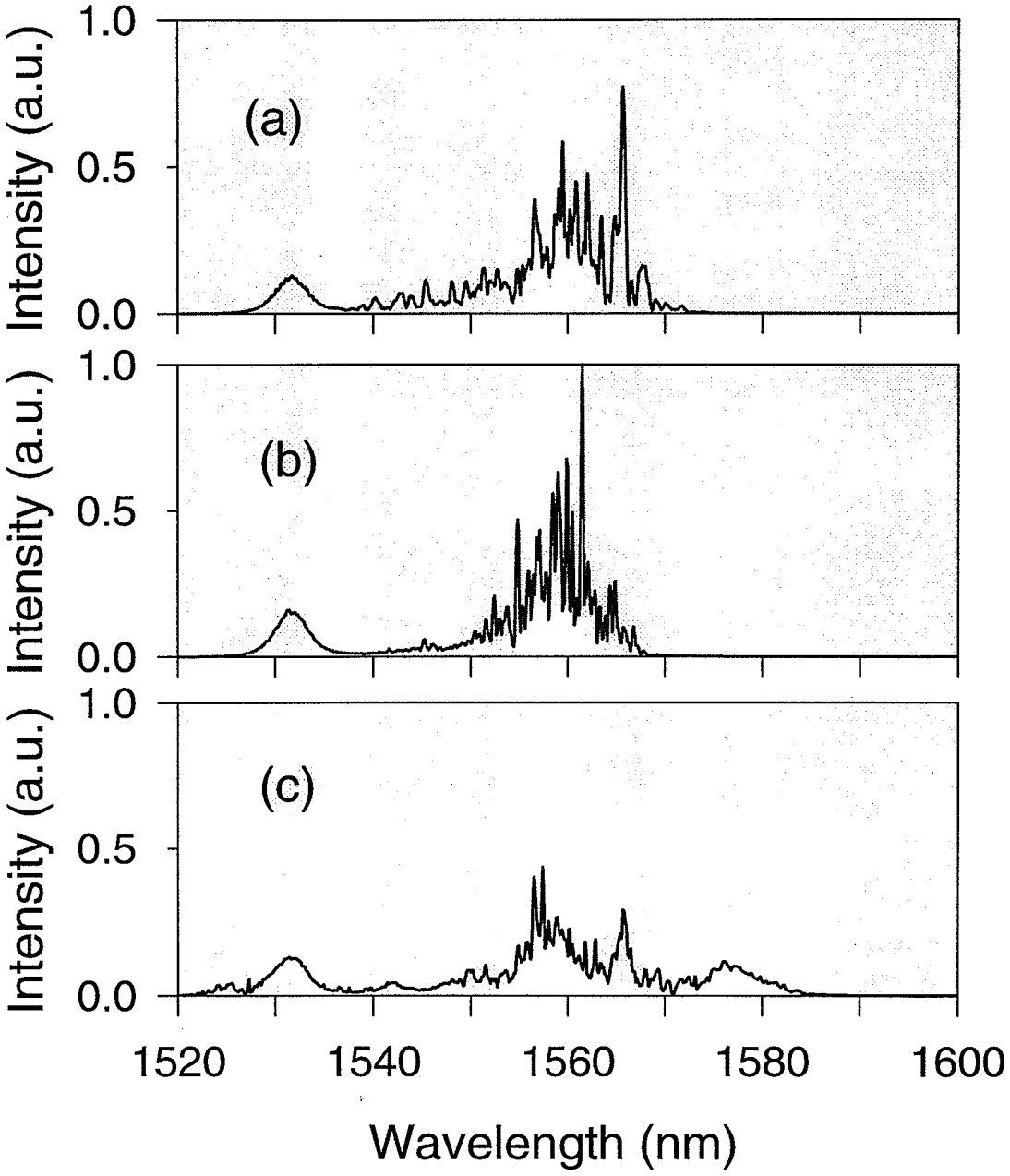

Fig. 5.8. Output spectra after thresholder fiber for (a): 63-63 non-conjugate (or orthogonal); (b): 31-63 non-conjugate; (c): 63-63 conjugate M-sequence codes

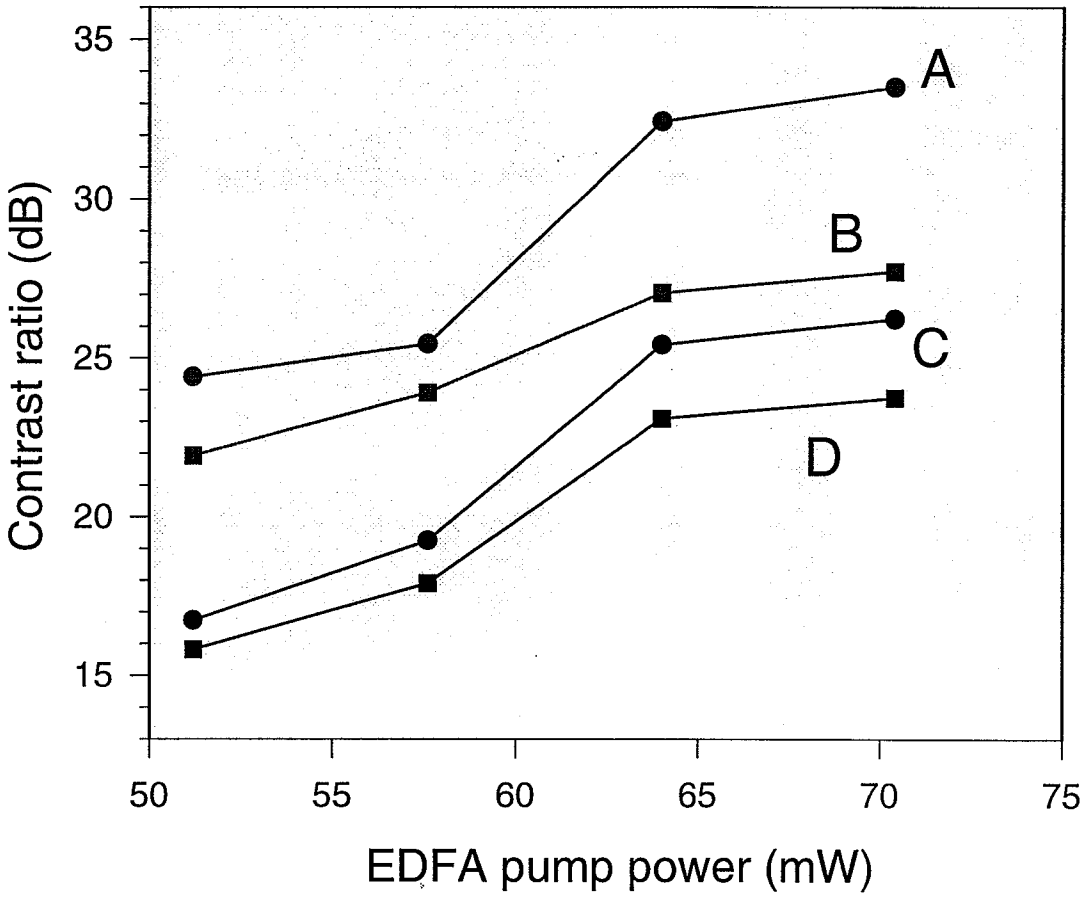

Fig. 5.9. Contrast ratios as function of EDFA pump power at the output of the photodetector for a decoder with length-31 codes when interference signals are encoded with length-63 (line A) or length-31 (line B) codes and for a decoder with length-63 codes when interference signals are encoded with length-63 (line C) or length-31 (line D). The filter cut-off wavelength is >1573 nm.

6. CONCLUSIONS

6.1 Summary

In this thesis I have presented the first experimental demonstrations of the femtosecond pulse CDMA scheme over a single-user CDMA testbed consisting of a single CDMA transmitter/receiver pair linked with a 2.5-km transmission fiber. In the process of assembling such single-user CDMA system, a few key CDMA sub-system component technologies, namely femtosecond pulse fiber laser, dispersion compensation, and femtosecond encoding/decoding, were developed and successfully tested. For the femtosecond pulse source, a stretched-pulse mode-locked Er-fiber ring laser was built which produces a reasonable stable ~65-fsec pulse strain at 33 MHz. The mode-locking is easy to initiate and can stay for a very long period of time provided the pump 980-nm source is stable. Furthermore, the mode-locked pulse characteristics (such as power spectrum and pulse width) are fairly repeatable in terms of daily operation. This is important because the fiber link is dispersion optimized for a certain wavelength and any deviation from the designed spectrum may experience more dispersion which eventually leads to reduction in contrast ratio (although this can be fixed by applying correcting phase to LCM). For the dispersion compensation, we have demonstrated the first use of a suitable DCF to compensate the dispersion of SMF for femtosecond pulse transmission. Pulse stretch/recompression ratio as high as 800 is demonstrated in a 2.5-km all-fiber dispersion-compensated link. This 2.5-km SMF-DCF link has a small residual third-order dispersion which is 3 to 5 times lower than that of dispersion-shifted fibers. As a result, output pulses from this fiber link experience very less pulse broadening (within a factor of 2) for input pulses of 250 to 500 fsec in duration. The residual dispersion is almost completely removed

by the programmable pulse shapers which also serve as the CDMA phase coding devices. Consequently, distortionless transmission for sub-500-fsec pulses over 2.5 km of fibers is demonstrated. The CDMA encoder and decoder we built are a pair of identical fiber-pigtailed pulse shapers with a 128-element liquid crystal phase modulator LCM as a spectral filter. A very low insertion loss (fiber to fiber) of 5.3 dB and small pulse distortion are achieved with proper choices of physical components and careful alignments. High-fidelity encoding and subsequent decoding of femtosecond pulses for various code lengths were successfully demonstrated by virtue of almost exactly the same spectrum-to-space correspondence in the LCM plane for both pulse shapers. Furthermore, the phases applied to the LCM can be programmed to provide not only CDMA phase encoding/decoding but also simultaneously phase correction to compensate any residual dispersion in the system. This capability of the LCM is of great importance to real multiple-user CDMA systems where signals from different other users have different residual dispersion due to the differences in the mode-locked spectra and/or transmission distances.

On the system level, we have demonstrated high-fidelity 2.5-km fiber transmission of spectrally encoded femtosecond pulses which results in high contrast ratio (30 dB) between properly and improperly decoded pulses after the nonlinear thresholder. The physical parameters, such as pulsewidth, average power, pump power level, and residual dispersion of the fiber link, employd in this single-user system can be used as a guidance in designing mutiple-user CDMA systems and the experimental results such , as energy contrast ratios, obtained here can also serve as a baseline estimate for multiple-user systems.

6.2 Concluding Remarks and Future Works

The purpose of this thesis research (along with one other collegue's) is to explore the physical feasibility the femtosecond pulse CDMA. Although the single-user CDMA system we have demonstrated is somewhat rudimentary, it does show potential for mutiple-access operation from the high contrast ratio demonstrated. The

system performances such as energy contrast ratio and transmission fiber length can be enhanced by the improvements of the various component technologies. For the fiber laser source, the use of more efficient Er-fiber and better laser cavity design can produce femtosecond pulses with average power as high as several tens of mW [65]. With such high laser power, the need for pre-EDFA in the transmitter can be lifted. This not only reduces the complexity and thus cost of the system but also eliminates any problem associated with a CPA-EDFA, such as polarization mode dispersion [66]. Replacing with bulk 980-nm Ti-saphire pump lasers with compact laser diodes will make the system more portable and one step closer to practical use. As for the dispersion compensation, with the combination of a DCF (for coarse dispersion compensation) and pulse shapers (for fine tuning residual dispersion) a much longer dispersion-free fiber transmission distance can be achieved if both encoder and decoder LCMs are used to their full capacity. With current setup, this distance can exceed 30 km. For the coding devices, current spectral resoluation of the pulse shapers is larger than the pixel width of the LCMs. If the spectral resolution is improved (e.g. by using larger input beam sizes), not only the transmission length can be extended but also the fidelity of encoding/decoding can be enhanced and thus the contrast ratio. The energy contrast ratio can also be enhanced by an enhanced post-EDFA and a better design in the long-pass spectral filter. The current contrast ratio is basically limited by the amount of nonlinear spectral phase shift and the long-wavelength components of ASE. The use of an EDFA of higher amplification can increase the spectral shift to longer wavelength and moving the cutoff of the spectral filter to a longer wavelength can get around the ASE. If both parameters (pump power and cutoff) are optimally chosen, very much higher contrast ratios should be obtainable.

Finally, there are two major problems to be solved for the CDMA to have a chance for practical use. The first is the polarization effect. Since optical fiber is slightly birefringent the polarization of light is evolving along the fiber transmission. Because the pulse shapers contain polarization-sensitive elements such as gratings and LCM, polarization controllers have to be used in a few locations (e.g. the input end of

the encoder and both ends of the decoder) to optimize the throughput of the system. The difference in the energy contrast between the two conditions with the polarization optimized and not optimized can be as high as 20 dB. Furthermore, the optimized polarization condition can quickly drift away and constant adjustment of all polarization controllers is necessary. In a real system, this is very impractical and remedies such as the use of polarization-maintaining fibers or some kind of automatic polarization control has to be applied. The second probem in realization of true CDMA systems is the alignment of all encoder and decoder. The most time-consuming part of our CDMA project was building the two identical pulse shapers. Tremendous efforts and time have been spent to iteratively adjust various components in both pulse shapers. In reality, it is highly impossible to align all the bulk-optic encoder and decoder pulse shapers. To solve this problem, an integrated-optic version of the pulse shaper which can be mass-produced has to be developed.

LIST OF REFERENCES

[1] S. Kawanishi, H. Takara, T. Morioka, O. Kamatani, K. Kikoh, and M. Saruwatari, "Single channel 400 Gbit/s time-division-multiplexed transmission of 0.98 ps pulses over 40 km employing dispersion slope compensation," Electr. Lett. vol. 9, pp. 457-459, 1996.

[2] H. Onaka et al., "1.1 Tb/s WDM transmission over 150 km 1.3 μm zero-dispersion single-mode fiber," in Conference of Optical Fiber Communication (OFC'96), postdealine paper, PD-19, San Jose, CA, 1996.

[3] G. E. Keiser, *Local Area Networks*, McGraw-Hill, New York, 1989.

[4] J. Y. Hui, "Pattern Code Modulation and Optical Decoding - A Novel Code Division Multiplexing Technique for Multifiber Network," IEEE Journal Select. Areas Commun. SAC-3, 916-927 (1985).

[5] P. R. Prucnal, M. A. Santoro, and T. R. Fan, "Spread Spectrum Fiber-Optic Local Area Network Using Optical Processing," IEEE J. Lightwave Technol. LT-4, PP. 547, 1986.

[6] J. A. Salehi, "Code-Division Multiple-Access Techniques in Optical Fiber Networks - Part I: Fundamental Principles," IEEE Trans. Comm. vol. 37, PP. 824-833, 1989.

[7] A. M. Weiner, J. P. Heritage, and J. A. Salehi, "Encoding and decoding of femtosecond pulses," Opt. Lett. vol. 13, PP. 300-302, 1988.

[8] A. M. Weiner, J. A. Salehi, J. P. Heritage, and M. Stern, "Encoding and Decoding of Femtosecond Pulses for Code-Division Multiple-Access", J. E. Midwinter and H. S. Hintons, Eds., OSA Proceedings on Photonic Switching (Optical Society of America, Washington, DC, 1989) ,vol. 3, pp. 263-269 .

[9] J. A. Salehi, A. M. Weiner, and J. P. Heritage, "Coherent ultrashort light pulse code-division multiple access communication systems," J. Lightwave Tech. vol. 8, pp. 478-491, 1990.

[10] A. M. Weiner and J. A. Salehi, "Optical Code-Division Multiple-Access," in Photonics in Switching, J. Midwinter, ed. (Academic Press, San Diego, 1993), vol. II, pp. 73-118.

[11] D. Zaccarin and M. Kavehrad, "An Optical CDMA System Based on Spectral Encoding of LED," IEEE Phot. Tech. Lett. vol. 5, pp. 479-482, 1993.

[12] R. A. Griffin, D. D. Sampson, and D. A. Jackson, "Coherence Coding for Code-Division Multiple-Access Networks," IEEE J. Lightwave Technol. vol. 13, pp. 1826-1837, 1995.

[13] L. Nguyen, B. Aazhang, and J. F. Young, "All-Optical CDMA with Bipolar Codes," Electronics letters 31, (1995).

[14] L. Boivin, M. C. Nuss, W. H. Knox, and J. B. Stark, "206-channel chirped-pulse wavelength-division multiplexed transmitter," Elect. Lett. vol. 33, pp. 827-828, 1997.

[15] A. E. Siegman, *Lasers*, University Science Books, California, 1986.

[16] U. Keller, and T. S. Chiu, "Resonant Passive Mode-Locked Nd:YLF laser", IEEE J. Quantum Electron. vol 28, pp. 1710-1721, 1992.

[17] B. C. Barnett, L. Rahman, M. N. Islam, Y. C. Chen, P. Bhattacharya, W. Riha, K. V. Reddy, A. T. Howe, K. A. Stair, H. Iwamura, S. R. Friberg, and T. Mukai, "High power erbium-doped fiber laser mode locked by a semiconductor saturable absorber," Opt. Lett, vol. 20, 471-473, 1995.

[18] H. A. Haus, E. P. Ippen, and K. Tamura, "Additive-pulse modelocking in fiber laser", IEEE J. Quantum Electron. vol 30, pp. 200-207, 1994.

[19] D. J. Richardson, R. I. Laming, D. N. Payne, V. Matsas, and M. W. Phillips, "Selfstarting, passively modeloched erbium fiber ring laser based on the amplifying sagnac switch", Electon. Lett., vol 27, pp. 542-544, 1991.

[20] I. N. Duling III, "Subpicosecond all-fiber erbium laser", Electon. Lett., vol 27, pp. 544-545, 1991.

[21] V. J. Matsas, T. P. Newson, D. J. Richardson, and D. N. Payne, "Selfstarting passively modelocked fiber ring laser exploiting nonlinear polarization rotation", Electon. Lett., vol 28, pp. 1391-1393, 1992.

[22] K. Tamura, H. A. Haus, and E. P. Ippen, "Self-starting additive pulse mode-locking erbium fibre ring laser", Electon. Lett., vol 28, pp. 2226-2228, 1992.

[23] H. A. Haus, K. Tamura, L. E. Nelson, and E. P. Ippen, "Stretched-pulse Additive pulse mode-locking in fiber ring laser: theory and experiment", IEEE J. Quantum Electron. vol 31, pp. 591-598, 1995.

[24] K. Tamura, E. P. Ippen, H. A. Haus, and L. E. Nelson, "77-fs pulse generation from a stretched-pulse mode-locked all-fiber ring laser", Opt. Lett. vol 18, pp. 1080-1082, 1993.

[25] K. Tamura, L. E. Nelson, H. A. Haus, and E. P. Ippen, "Soliton versus nonsoliton operation of fiber ring lasers", Appl. Phys. Lett., vol. 64, pp. 149-151, 1994.

[26] W. J. Tomlinson, R. H. Stolen, and A. M. Johnson, "Optical wave breaking of pulses in nonlinear optical fibers," Opt. Lett., vol. 10, pp. 457-459, 1985.

[27] E. P. Ippen, and C. V. Shank, "Techniques for measurement" in *Ultrashort Light Pulses*, S. L. Shapito ed., Springer-Verlag, New York, 1984, ch. 3.

[28] D. Le Guen, F. Favre, M. L. Moulinard, M. Henry, G. Michaud, L. Mace, F. Devaux, B. Charbonnier, T. Georges, Technical Digest, OFC'97, PD-17, pp.436-438, 1997.

[29] G. P. Agrawal, *Fiber-Optic Communication Systems*, Chap. 2, Wiley, New York, 1992.

[30] R. Kashyap, S. V. Chernikov, P. F. McKee, and J. R. Taylor, "30 ps chromatic dispersion compensation of 400 fs pulses at 100 Gbits/s in optical fibers using an all fiber photoinduced chirped reflection grating," Elect. Lett. vol. 30, pp. 1078-1080, 1994.

[31] S. V. Chernikov, J. R. Taylor, and R. Kashyap, "Optical fiber dispersion compensation at 100 Gbits/s by using a novel transmission fiber based on chirped fiber Brágg gratings," Conference on Laser and Electo-optics, Baltimore, MD, May, 1995.

[32] B. J. Eggleton, F. Ouellette, K. A. Ahmed, P. A. Krug, and H.-F. Liu, "Recompression of pulses broadened by transmission through 10 km of non-dispersion-shifted fiber at 1.55 μm using 40-mm-long optical fiber Bragg gratings with tunable chirp and central wavelength," Photon Tech. Lett., vol. 7, pp. 494-496, 1995.

[33] L. Dong, M. J. Cole, A. D. Ellis, M. Durkin, M. Ibsen, V. Gusmeroli, and R. I. Laming, "40 Gbit/s 1.55 μm transmission over 109 km of non-dispersion shifted fibre with long continously chirped fibre gratings," Technical Digest, Optical Fiber Communication Conference, OFC 97, paper PD-6, pp. 391-394, 1997.

[34] M. Stern, J. P. Heritage, and E. W. Chase, "Grating compensation of third-order fiber dispersion," IEEE J. Quantum Electron., vol. 28, pp. 2742-2748, 1992.

[35] S. Watanabe, T. Naito, and T. Chikama, "Compensation of chromatic dispersion in a single-mode fiber by optical phase conjugation," IEEE Photonics Technol. Lett., vol. 5, pp. 92-95, 1993.

[36] R. M. Jopson, A. H. Gnauck, and R. M. Derosier, "10-Gb/s 360-km transmission over normal-dispersion fiber using mid-system spectral inversion," OFC 93, San Jose, pp. 17-20, 1993.

[37] A. D. Ellis,M. C. Tatham, D.A.O. Davies, D. Nessett, D. G. Moodie, and G. Sherlock, "40 Gbit/s transmission over 202 km of standard fibre using midspan spectral inversion," Elect. Lett. vol. 31, pp. 299-301.

[38] A. H. Gnauck, R. M. Jopson, P. P. Iannone, and R. M. Derosier, "Transmission of two wavelength-multiplexed 10 Gbit/s channels over 560 km of dispersive fibre," Elect. Lett. vol. 30, pp. 727-728.

[39] J. M. Dugan, A. J. Price, M. Ramadan, D. L. Wolf, E. F. Murphy, A. J. Antos, D. K. Smith, and D. W. Hall, "All-optical, fiber-based 1550 nm dispersion compensation in a 10 Gbit/s, 150 km transmission experiment over 1310 nm optimized fiber," in *Optical Fiber Communication*, vol. 5 of 1992 OSA Technical Digest Series (Optical Society of America, Washington, D.C., 1992), paper PD-14.

[40] H. Izadpanah, C. Lin, J. Gimlett, D. W. Hall, and D. K. Smith, "Dispersion compensation in 1310 nm-optimized SMFs using an equalizer fiber, EDFAs and 1310/1550 nm WDM," Electron. Lett., vol. 28, pp. 1469-1471, 1992.

[41] A. J. Antos, D. W. Hall, and D. K. Smith, "Dispersion-compensating fiber for upgrading existing 1310-nm-optimized systems to 1550-nm operation," Technical Digest, Optical Fiber Communication Conference, OFC 93, paper THJ3, pp. 204-205, 1993.

[42] C. D. Poole, J. M. Wiesenfeld, D. J. DiGiovanni, and A. M. Vengsarkar, "Optical fiber-based dispersion compensation using high-order modes near cut-off," J. Lightwave Technol. vol. 12, pp. 1746-1758, 1994.

[43] C.-C. Chang, and A. M. Weiner, "Dispersion compensation for ultrashort pulse transmission using two-mode equalizer fibers," Photon. Technol. Lett. vol. 6, pp. 1392-1394, 1994.

[44] C. Lin, H. Kogelnik, and L. G. Cohen, "Optical-pulse equalization of low-dispersion transmission in single-mode fibers in the 1.3-1.7 μm spectral region," Opt. Lett. vol. 5, pp. 476-478, 1980.

[45] A. M. Vengsarkar, A. E. Miller, M. Haner, A. H.Gnauck, W. A. Reed, K. L. Walker, 'Fundamental-mode dispersion-compensating fibers: design consideration and experiments,' OFC Technical Digest, paper Thk2, p. 225-227 (1994).

[46] L.G. Cohen, 'Comparison of single-mode fiber dispersion measurement techniques,' J. Lightwave Technol., vol. 3, pp. 958-966, 1985.

[47] W. H. Knox, 'Dispersion measurements for femtosecond-pulse generation and applications,' Appl. Phys. B, vol. 58, pp. 225-235, 1994.

[48] H.-T. Shang, 'Chromatic dispersion measurement by white-light interferometry on meter-length single-mode optical fibers,' Elect. Lett. vol. 17, pp. 603-605, 1981.

[49] J. Stone, and D. Marcuse, 'Direct measurement of second-order dispersion in short optical fibers using white-light interferometry,' Elect. Lett., vol. 20, pp. 751-752, 1984.

[50] F. Reynaud, F. Salin, and A. Barthelemy, 'Measurement of phase shifts introduced by nonlinear optical phenomena on subpicosecond pulses,' Opt. Lett., vol. 14, pp. 275-277, 1989.

[51] X. D. Cao, and D. D. Meyerhofer, 'Frequency-domain interferometer for measurement of the polarization mode dispersion in single-mode optical fiber,' Opt. Lett., vol. 19, pp. 1837-1839, 1994.

[52] L. Lepetit, G. Cheriaux, and M. Joffre, 'Linear techniques of phase measurement by femtosecond spectral interferometry for application in spectroscopy,' J. Opt. Soc. Am. B, vol. 12, pp. 2467-2474, 1995.

[53] G. P. Agrawal, *Nonlinear Fiber Optics*, 2nd ed. (Academic Press, San Diego, 1995), Chap. 2.

[54] H. P. Sardesai, Ph. D. Thesis, School of Electrical and Computer Engineering, Purdue University, Dec. 1997.

[55] M. L. Stock, A. Galvanauskas, M. E. Fermann, G. Mourou, and D. J. Harter, "Generation of high-power femtosecond optical pulses by chirped pulse amplification in erbium doped fibers," Technical Digest of the Nonlinear and Guided-Wave Phenomena Topical Meeting, paper PD5-1, pp. 412-414, 1993.

[56] A. M. Weiner, J. P. Heritage, and E. M. Kirschner, "High-resolution femtosecond pulse shaping," J. Opt. Soc. Am. B, vol. 5, pp. 1563-1572, 1988.

[57] A. M. Weiner, D. E. Leaird, J. S. Patel, and J. R. Wullert, II, "Programmable shaping of femtosecond optical pulses by use of 128-element liquid crystal phase modulator," IEEE J. Quantum Electron., vol. 28, pp. 908-920, 1992.

[58] c. Froehly, B. Colombeau, and M. Vampouille, in *Progress in Optics*, vol. 20, pp. 65, E. Wolf ed., Amsterdam, North-Holland, 1983.

[59] R. N. Thurston, J. P. Heritage, A. M. Weiner, and W. J. Tomlinson, "Analysis of picosecond pulse shape synthesis by spectral masking in the grating pulse compressor," IEEE J. Quantum Electron., vol. 22, pp. 682-696, 1986.

[60] A. M. Weiner, "Femtosecond optical pulse shaping and processing," Progress in Quantum Electron. vol. 19, pp. 161-237, 1995.

[61] J. P. Heritage, E. W. Chase, R. N. Thurston, and M. Stern, "A simple femtosecond optical third-order disperser", Conference on Lasers and Electro-optics (Optical Society of America, Baltimore, MD, 1991) pp. 74-75.

[62] R. L. Peterson, R. E. Ziemer, and D. E. Borth, *Introduction to Spread Spectrum Communications,"* Prentice-Hall, New Jersey, 1995.

[63] H. P. Sardesai, and A. M. Weiner, " A nonlinear fiber-optic receiver for ultrashort pulse code division multiple access communications," Elect. Lett., vol. 7, pp. 610-611, (1997).

[64] G. P. Agrawal and M. J. Potasek, "Nonlinear pulse distortion in single-mode optical fibers at zero-dispersion wavelength," Phys. Rev. A. 33, pp. vol. pp. 1765-1766, 1986.

[65] K. Tamura and M. Nakazawa, "Optimizing power extraction in stretched-pulse fiber ring lasers," Appl. Phys. Lett., vol. 67, pp. 3691-3693, 1995.

[66] C. D. Poole and J. Nagel, "Polarization effects in lightwave systems," in *Optical Fiber Telecommunications*, ed. I. P. Kaminow and T. L. Koch, Academic Press, 1997.

VITA

Cheng-Chun was born in Taipei, Taiwan in 1963. He received the B.S. degree in Civil Engineering from National Taiwan University in 1985. He then served the army of Republic of China from 1985 to 1987. He received the M.S. degrees in Engineering Mechanics and Electrical Engineeing from Virginia Polytechnic Institute and State University in 1990 and 1992, respectively, and the Ph. D. degree in Electrical Engineering from Purdue University in 1997. His research interests are ultrashort pulse fiber lasers, fiber dispersion compensation, femtosecond pulse shaping, and fiber-optic communications. He has published over 25 articles in conferences and journals and is a member of Eta Kappa Nu and Optical Society of America.